Novel nanoscopic FeF_3–based materials: synthesis, characterisation, and catalytic applications

Dissertation

zur Erlangung des akademischen Grades
doctor rerum naturalium
(Dr. rer. nat.)
im Fach Chemie
eingereicht an der

Mathematisch-Naturwissenschaftlichen Fakultät I
der Humboldt-Universität zu Berlin
von

Ying Guo

Präsident der Humboldt-Universität zu Berlin
Prof. Dr. Jan-Hendrik Olbertz

Dekan der Mathematisch-Naturwissenschaftlichen Fakultät I
Prof. Stefan Hecht, PhD

Gutachter: 1. Prof. Dr. Erhard Kemnitz

2. Prof. Dr. Nicola Pinna

Tag der mündlichen Prüfung: 19-06-2013

Ars longa, vita brevis.

Kurzfassung

Nanoskopische Metallfluoride mit auf der Oberfläche gebundenen Hydroxygruppen sind für die heterogene Katalyse von großer Bedeutung. Mit Katalysatoren die an der Oberfläche Lewis- und Brønsted-saure Zentren besitzen, lassen sich zahlreiche Reaktionen katalysieren. Frühere Studien berichteten bereits über bi-acide Materialien basierend auf Aluminium- oder Magnesiumfluorid die mittels Sol-Gel-Synthese dargestellt wurden. Diese Materialien zeigten exzellente Leistungen in verschiedenen Reaktionen. Übergangsmetallfluoride könnten ebenfalls die erwünschten Eigenschaften aufweisen, allerdings hat sich deren Synthese und Charakterisierung hinsichtlich nano-kristalliner Materialien noch nicht etabliert. Das Hauptaugenmerk dieser Arbeit liegt auf einer Pilotstudie zur Darstellung von Eisen(III)fluorid (FeF_3) unter Verwendung von Sol-Gel-Syntheserouten. Eine modifizierte fluorolytische Sol-Gel-Synthese wurde entwickelt um bi-acide auf FeF_3 basierende Materialien zu erhalten. Die Synthese beginnt mit der Predehydratisierung des Eisenpräkursors, einem Nitratsalz. Diese Prozedur erzeugt Hydroxygruppen, die potentiellen Brønsted-sauren Zentren, auf der Oberfläche der klassischen Lewissäure FeF_3. Im Anschluss wurde Magnesiumfluorid (MgF_2) als Matrix eingesetzt um die porösen Eigenschaften des FeF_3 einzustellen. Die Ein-Schritt-Fluorierung der vermischten Präkursoren führt zu ternären FeF_3-MgF_2 Materialien. Deren Bulk-Eigenschaften wurden mit verschiedenen analytischen Methoden untersucht, u.a. Elementar- und Thermoanalyse, Röntgenpulverdiffraktometrie (XRD) und Transmissionselektronenmikroskopie (TEM). Die Wechselwirkung zwischen MgF_2 und FeF_3 wurde mittels Mössbauer-Spektroskopie und Röntgenphotoelektronenspektroskopie (XPS) aufgeklärt. Verglichen mit FeF_3 zeigen ternäre FeF_3-MgF_2 bemerkenswert hohe Oberflächen und verbesserte Porosität, wie mittels N_2-Adsorptions-Desorptions-Messungen gezeigt werden konnte. Das Wichtigste jedoch ist, das hauptsächlich starke Lewis- und mittelstarke Brønsted-saure Zentren auf der FeF_3-MgF_2 vorhanden sind, wie mittels temperaturprogrammierter Desorption von Ammoniak (NH_3-TPD) und Infrarotspektroskopie gekoppelt mit Chemisorption verschiedener Sondenmoleküle (Chemisortption-IR) gezeigt werden konnte. Des Weiteren wurden, unter Verwendung anderer Erdalkalimetallfluoride (CaF_2 oder SrF_2) und Zinkfluorid (ZnF_2) als Matrix, Serien ternärer Fluoridmaterialien synthetisiert und systematisch untersucht. TEM-Aufnahmen und die energiedispersive Röntgenspektroskopie (EDX) zeigen dass FeF_3 homogen in der MF_2-Matrix (M = Ca oder Sr) verteilt ist. Durch Charakterisierung der FeF_3-MF_2-Oberflächen konnten systematische Veränderungen hinsichtlich Größe der Oberfläche, Porosität und Azidität festgestellt werden. Mit abnehmender Atomnummer (von Sr zu Mg) erhöht sich die Stärke der sauren Zentren, während die mittlere Porengröße dramatisch abnimmt. Darüber hinaus führt ein größeres M-zu-Fe-Verhältnis generell zu kleineren Porengrößen und höheren Oberflächen. Diese Ergebnisse implizieren, dass die Eigenschaften ternärer FeF_3-MF_2 durch Veränderung der MF_2-Matrix oder des M-zu-Fe-Verhältnisses einstellbar sind. Diese Arbeit beweist damit die Realisierbarkeit der Synthese neuer nanoskopischer Metallfluoride mit gewünschten Oberflächeneigenschaften.

Schlussendlich konnte anhand einer Modellreaktion, der Isomerisierung von Citronellal zu Isopulegolen, die katalytische Aktivität der bi-aziden Zentren der auf FeF_3 basierenden Materialien, insbesondere FeF_3-MgF_2, nachgewiesen werden. Leaching- und Recycling-Tests zeigten, dass die Materialien in einem realen heterogen katalysierten Prozess robust arbeiten und wiederverwendbar sind. Zusätzlich wurde in dieser Arbeit diskutiert wie Oberfläche, Porosität und Azidität gemeinsam die katalytische Aktivität von FeF_3-MgF_2 bestimmen.

Letztendlich wurden in dieser Arbeit neue auf FeF_3 basierende Nanomaterialien entwickelt und ausführlich charakterisiert. Die modifizierte Sol-Gel-Route erzeugt nanoskopische Metallfluoride die sich durch Bi-Azidität und andere einstellbare Oberflächeneigenschaften auszeichnen, wodurch die Herstellung von Katalysatoren der nächsten Generation mit vorgegebener Porosität und Azidität befördert wird.

Schlagwörte: Bi-Azidität; heterogene Katalyse; Eisenfluorid; Nanomaterial; Sol-Gel-Synthese

Abstract

Nanoscopic metal fluorides with surface hydroxyl groups are of broad interest in heterogeneous catalysis. With both Lewis and Brønsted acid sites on the surface, they can catalyse a wide range of reactions. Previous studies have reported bi-acidic materials based on aluminium or magnesium fluoride prepared by a sol-gel route. These materials showed excellent performance in different reactions. Transition metal fluorides may also have desirable properties, but their syntheses and characterisation have not been established. This work addresses the issue with a pilot study on using sol-gel methods to develop iron(III) fluoride (FeF_3) based materials with surface bi-acidity.

A modified fluorolytic sol-gel route was established to prepare the bi-acidic FeF_3-based materials. The synthesis started with pre-dehydration of the iron precursor, a nitrate salt. This procedure introduced hydroxyl groups, the potential Brønsted acid sites, on the surface of a classic Lewis acid, FeF_3. Subsequently, magnesium fluoride (MgF_2) was used as matrix to tune the porosity of FeF_3. One-step fluorination of mixed precursors produced ternary FeF_3-MgF_2 materials. Their bulk properties were studied by a panel of analytical methods including elemental and thermal analysis, powder X-ray diffraction (XRD), and transmittance electron microscopy (TEM). Interaction between MgF_2 and FeF_3 was elucidated by using Mössbauer spectroscopy and X-ray photoelectron spectroscopy (XPS). Comparing with FeF_3, the ternary FeF_3-MgF_2 showed remarkable high surface area and enhanced porosity as revealed by N_2 adsorption-desorption measurements. Most importantly, strong Lewis and medium strong Brønsted acid sites were found predominant on the FeF_3-MgF_2 surface by temperature programmed desorption of ammonia (NH_3-TPD) and infrared spectroscopy coupled with chemisorption of different probe molecules (chemisorption-IR).

Next a series of ternary fluoride materials were synthesised and studied systematically, using other alkaline earth metal fluorides (CaF_2 or SrF_2) as well as zinc fluoride (ZnF_2) as matrix. TEM images together with energy-dispersive X-ray spectroscopy (EDX) suggested that FeF_3 is distributed homogeneously in the MF_2 matrix (M = Ca or Sr). Surface characterisation of FeF_3-MF_2 revealed systematic changes in their surface area, porosity, and surface acidity. With decreasing atom numbers (from Sr to Mg), strengths of surface acidic sites and surface area increased, while the average pore size decreased drastically. Moreover, higher M-to-Fe ratio generally resulted in smaller pore size and larger surface area. These findings imply that the properties of ternary FeF_3-MF_2 are tunable by changing the MF_2 matrix or the M-to-Fe ratio or both. Thus this work demonstrates the feasibility to synthesise novel nanoscopic metal fluorides with desirable surface properties.

Last but not least, in the model reaction of citronellal's isomerisation to isopulegols, FeF_3-based materials, particularly FeF_3-MgF_2, were highly active due to their bi-acidity. Results of leaching and recycling tests indicated that they work robustly in a real heterogeneous process and are reusable. Finally, this work discussed how surface area, porosity, and surface acidity jointly determined the catalytic activity of FeF_3-MF_2.

In conclusion, this work developed and extensively characterised novel FeF_3-based nanomaterials. The modified sol-gel route produces nanoscopic metal fluorides marked by bi-acidity and other tunable surface properties, thereby empowering the manufacture of next-generation catalysts with targeted porosity and acidity.

Keywords: bi-acidity; heterogeneous catalysis; iron fluoride; nanomaterial; sol-gel process

Table of contents

Table of figures and tables

Abbreviations

acac	acetylacetonate
BE	binding energy
B.E.T.	the method used by Brunauer, Emmet, and Teller to determine specific surface area
DLS	dynamic light scattering
EDX	energy dispersive X-ray spectroscopy
Eq.	equation
Fig.	figure
FWHM	full width at half maximum
Hal	halogen
HRTEM	high resolution transmission electron microscopy
HS	high-surface
I	intensity
IR	infrared
IS	isomer shift
MS	mass spectrometry
OAc	acetate group
PDF	powder diffraction file
QS	quadrupole splitting
STEM	scanning transmission electron microscopy
TEM	transmission electron microscopy
TG	thermogravimetry
THF	tetrahydrofuran
TPD	temperature programmed desorption
XPS	X-ray photoelectron spectroscopy
XRD	X-ray diffraction

1 Introduction

The human history is driven by the phylogeny of materials. But what is a material? The Oxford Dictionary gives its definition: a "material" is a substance that things can be made from.[1] This brief definition highlights the most prominent feature of a material: it is the fundamental of all other artificial creations. From bronze to nanomaterials, innovations of new materials and following applications have coined the contemporary life. With time, the initial instinct of collecting and modifying natural substances became the desire to invent new materials with superior properties that meet the requirements of a growing society. As these requirements become more and more specialised, the materials also become increasingly sophisticated. *High-performance*, *multifunctional*, and *sustainable* belong to the frequently used adjectives to describe today's new materials.

Some materials display extraordinary properties when downscaled to the nanometer range (approximately 1-100 nm). Their physicochemical properties are distinct from those of bulk materials. Thus the term "nanomaterial" comes into vocabulary of the public. Nanomaterial is defined by the International Organisation for Standardisation (ISO) and the European Standardisation Committee (CEN) as "material with any external dimension in the nanoscale or having internal structure or surface structure in the nanoscale."[2] According to this definition, the only common feature of all nanomaterials is the nanoscopic size. Nanomaterials can be of different chemical compositions including (but not restricted to) carbon materials (*e.g.* fullerene, carbon nanotubes, and graphene), inorganic nanoparticles and structures, and organic supramolecules. From the carbon nanotube/organic polymer composites in aerospace application[3] to the liposome and nanoparticles in drug delivery[4], nanomaterials are playing an active role in research laboratories of diverse disciplines. Especially, nanomaterial-based catalysts are frequently used in energy and environment related areas such as petroleum refinery, clean energy provision, pollutant degradation, and fine chemical production.

Various techniques have been developed to produce nanomaterial-based catalysts: gas-phase processes such as flame hydrolysis and chemical vapor deposition (CVD); wet-chemical techniques such as hydrothermal-solvothermal synthesis, precipitation and coprecipitation, and the sol-gel method; and solid-state reactions such as mechano-milling.[5] Among them, the sol-gel method attracts great attention because it is simple and mild. It has been widely used to synthesise a large variety of nanoscopic metal oxides. Some of these sol-gel prepared oxides, like alumina (Al_2O_3), silica (SiO_2), and zirconia (ZrO_2), are excellent heterogeneous catalysts (or catalyst supporters) thanks to their surface acidity and high surface area. Since fluorine (F) is the most electronegative element, metal fluorides are distinguished by their pronounced acidity compared with metal oxides. Conventional synthesis methods of metal fluorides, however, usually result in crystalline phases with low surface area; and thus applications of metal fluorides in catalysis are largely restricted.

To address this issue, a "fluorolytic" sol-gel method was proposed. Developed by E. Kemnitz *et al.*[6] in 2003, this synthesis route has become one of the most useful methods to synthesise nanoscopic metal fluorides. It is designed as an analogue to the classic hydrolytic sol-gel method. The major difference is that in the fluorolytic sol-gel route, hydrogen fluoride (HF) is used instead of water. The key step is a fluorolysis reaction that usually takes place at room temperature. Crystallisation of metal fluorides is therefore avoided and their nanoscopic features are preserved.

A large variety of nanoscopic metal fluorides have been prepared since the birth of this method. Benefiting from the electronegativity of fluorine, these nanoscopic metal fluorides generally exhibit pronounced surface Lewis acidity. Other common features include low long-range order, high surface area, and well developed porous system.[6, 7] These features make nanoscopic metal fluorides promising in heterogeneous catalysis. Indeed, some examples have revealed high activity in various reactions: AlF_3 as an extremely strong Lewis acid can catalyse the CCl_2F_2 dismutation and $C_3Br_2F_6$ isomerisation;[6] alkaline earth metal fluorides (MgF_2, CaF_2, SrF_2, and BaF_2) are highly active catalysts with different chemo-selectivity in the dehydrohalogenation of chlorofluorobutanes.[8] Within one decade, the sol-gel prepared nanoscopic metal fluorides have become an important class of heterogeneous catalysts.[7, 8]

Moreover, the fluorolytic sol-gel route is a very flexible method with tunable synthesis parameters.[9, 10] Screenings in precursors and solvents have been proved practical; fluorination reagents and reaction temperature can be adjusted, too. This flexibility allows the design and synthesis of different fluoride derivatives, for example: magnesium oxofluorides have been prepared by a two-step process, in which fluorolysis and hydrolysis are introduced separately;[11] in contrast, aluminium hydroxy fluorides or magnesium hydroxy fluorides with active surface hydroxyls have been produced by a one-step fluorination with aqueous HF solutions;[10, 12] and recently, noble metal nanoparticles have been successfully loaded on the surface of aluminium hydroxy fluorides via *in situ* reduction of the noble metal precursors in fluoride sol.[13, 14] Therefore various nanoscopic metal fluorides based catalysts can be prepared through modified sol-gel methods, and their prospects in heterogeneous catalysis are nearly unlimited because of the combination of many synthesis parameters.

Among all types of fluoride derivatives, partially hydroxylated metal fluorides (hydroxy fluorides) play an active role in heterogeneous catalysis in recent years. Partially hydroxylated magnesium fluorides and aluminium fluorides are highly active in acid-catalysed reactions such as the Friedel-Crafts alkylation (*e.g.* synthesis of vitamin E and vitamin K1)[15] and the carbonyl-ene reaction (isomerisation of citronellal to isopulegols).[16] Doping the hydroxylated fluorides further with noble metals (*e.g.* Pd, Pt, Ag, and Au) leads to multi-functional fluoride catalysts that provide both surface acidity and hydrogenation ability;[13, 14, 17] this type of catalysts are able to catalyse the one-pot synthesis from citronellal or citral to menthol. In 2012, a Sn-doped hydroxylated magnesium fluoride was reported as an efficient catalyst in the degradation of cellulose, offering a feedstock in bio-ethanol production.[18]

Despite much progress, present hydroxylated fluorides catalysts are mostly based on a narrow range of main group metal fluorides, *i.e.* aluminium fluoride and magnesium fluoride. Naturally the questions arose whether it is possible to develop partially hydroxylated transition metal fluorides, and whether they can provide comparable or even better catalytic performances than main group metal fluorides. This work therefore aimed at providing a pilot study to tentatively answer the questions.

The primary task was to select a proper transition metal as the research object. Three principles were proposed for the screening:

- the corresponding fluoride must be a Lewis acid;
- hydroxyl groups must be introduced without changing the stability of the fluorides;

- economy cost should be considered, and thus low-cost precursors were preferred.

Following these principles, a preliminary screening in the transition metals was performed. Chapter 3 summarises the screening results. Iron (Fe) was chosen as a favourable candidate and the research would focus on iron(III) fluoride (FeF_3).

Pure FeF_3 shows a pale green colour and possesses a VF_3 structure, in which each Fe atom is six-fold coordinated.[19] Conventionally, it can be prepared by heating Fe or Fe_2O_3 in F_2 gas flow,[19] or by the reaction between $FeCl_3$ and HF.[20] Since another iron(III) halide, $FeCl_3$, is frequently used as a typical Lewis acid catalyst in the Friedel-Crafts reaction and the Diels-Alder reaction,[21] FeF_3 may be effective as well. Previously reported studies include examples of using FeF_3 catalysts in the selective addition of cyanotrimethylsilane to aldehydes,[22] and in the aryl-aryl cross coupling (together with Grignard reagents).[23] Using FeF_3 as heterogeneous catalyst is less often, probably because the conventionally prepared FeF_3 is in crystalline phase, and hence it exhibits low surface area and few surface active sites, which are disadvantages in heterogeneous processes. K. Murthy[24] and I. Murwani[25] have separately reported mixed fluorides catalysts using FeF_3 as a dopant. This type of catalysts have been tested in gas-phase reactions like dismutation of CCl_2F_2 and hydrofluorination of C_2Cl_4,[24] and in liquid-phase reactions like benzoylation of anisole[24] and oxidation of ethylbenzene to acetophenone.[25] These studies, however, have only addressed the Lewis acidity of FeF_3. The prospect of FeF_3 coupled with Brønsted acid sites has not yet been tested. Thus synthesis of a partially hydroxylated nanoscopic FeF_3 is a key step to thoroughly investigate its potential as a heterogeneous catalyst. Especially, although the hydroxyl groups in iron hydroxide ($Fe(OH)_3$) and iron oxohydroxide (FeO(OH)) are basic,[19] the hydroxyl groups in FeF_3 may become acidic because of the electronegativity of F. Similar conversion of acidity-basicity has been observed by comparing surface hydroxyl groups in magnesium oxide and in partially hydroxylated magnesium fluoride.[10] Thus if both Lewis and Brønsted acid sites are on the surface, this partially hydroxylated FeF_3 can act as bi-acidic catalyst. Moreover, since the partially hydroxylated FeF_3 will be tested as heterogeneous catalysts, high surface is preferred because heterogeneous catalysis is a surface phenomenon.

In light of this background, this work was designed to achieve the following targets:

- establishment of a sol-gel synthesis route of partially hydroxylated FeF_3:
  - optimisation of synthesis parameters (precursor, solvent, and fluorination reagent) of the sol-gel route of nanoscopic FeF_3;
  - substantial modification of the sol-gel route in order to introduce the hydroxyl groups on the surface of FeF_3;
  - preparation of high-surface FeF_3-based materials;
- characterisation of obtained FeF_3-based materials with emphasis on their surface properties:
  - using elemental analysis, thermal analysis, powder X-ray diffraction (XRD), Mössbauer spectroscopy, and transmittance electron microscopy (TEM) to study the composition and structure of FeF_3-based materials;
  - using N_2 adsorption-desorption measurements to determine surface area and porosity;

- using ammonia temperature programmed desorption (NH_3-TPD) and infrared spectroscopy coupled with chemisorption of probe molecules (chemisorption-IR) to study surface acidity;

- evaluation of the potential of FeF_3-based materials as heterogeneous catalysts with the model reaction, the isomerisation of citronellal to isopulegols. Despite its importance in the fine chemical industry,[26, 27] this intramolecular carbonyl-ene reaction has the advantage that both Lewis and Brønsted acid sites are involved in the heterogeneous process.[28] Thus it can provide strong evidence for the bi-acidity of partially hydroxylated FeF_3-based materials.

In short, this work aimed at developing novel FeF_3-based materials with high surface area and bi-acidity. The most important breakthrough was introducing hydroxyl groups (potential Brønsted acid sites) on to the surface of FeF_3. Chapter 4 describes how the synthesis route was developed and gives detailed characterisation of the partially hydroxylated FeF_3. The endeavour in preparing a high-surface material is addressed in Chapter 5. The problem was solved by using magnesium fluoride (MgF_2) as matrix. Other important results and discussion in this chapter include the characterisation of obtained ternary FeF_3-MgF_2 materials and the investigation into interactions between the two components. Chapter 6 summarises the follow-up work using other alkaline earth metal fluorides (CaF_2 and SrF_2) as well as zinc fluoride (ZnF_2) as matrix. The discussion of characterisation results focuses on the systematic changes in properties with respect to different metal fluoride matrices. Last but not least, partially hydroxylated FeF_3 materials with and without matrix were tested in the model reaction of citronellal's isomerisation. Chapter 7 gives a brief introduction of this reaction and summarises the catalytic results of these FeF_3-based materials. The correlation between their catalytic activity and surface properties (*i.e.* surface area, porosity, and surface acidity) are also discussed in Chapter 7.

2 Research background

2.1 Sol-gel chemistry

Syntheses of nanoscopic FeF_3-based materials are based on the sol-gel method. Fig. 2.1 summarises the fundamental steps in a sol-gel process. This method is extremely useful in manufacturing inorganic porous materials, inorganic-organic hybrid materials, and polymers. As indicated by its name, the sol-gel process involves a "sol" or a "gel". Definitions of these two terms, however, may vary according to different synthesis purposes. Because this work deals with inorganic materials, here a sol refers to a colloid suspension of solid particles in size between approximately 1-1000 nm in a liquid phase, while a gel is a solid network that is expanded in a liquid phase; the solid network can be covalently linked (polymeric gel) or formed from particulate sols by van der Waals forces (particulate gel).[29, 30] Drying a sol or gel by evaporation leads to the formation of a xerogel, in which the porous structure completely or partly collapses. If a gel is dried under supercritical conditions, it gives rise to an aerogel that preserves the porous structure of the wet gel with none or little shrinkage. Both xerogels and aerogels are high-surface and porous materials; especially, they may exhibit a large number of surface labile sites.[29] These features are essential in heterogeneous catalyses. Thus the sol-gel method is frequently used to produce heterogeneous catalysts or catalysts supports.

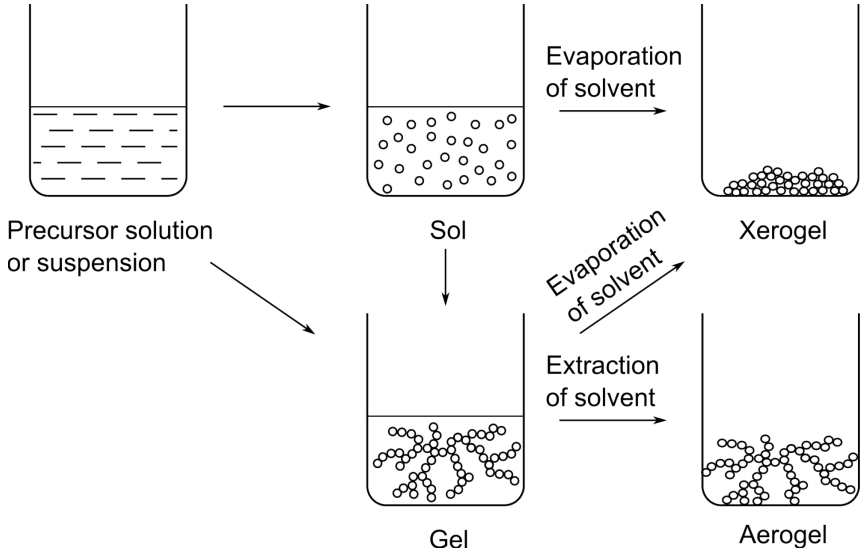

Fig. 2.1 Schematic illustration of the sol-gel process.

Conventionally, the sol-gel process was applied in the syntheses of metal oxides like SiO_2, TiO_2, ZrO_2, and Al_2O_3. The essential step in this process is a hydrolysis reaction of the precursor. Thus this process is also named as the hydrolytic sol-gel route. In 2003, E. Kemnitz *et al.*[6] reported a novel sol-gel synthesis route for nanoscopic metal fluorides. In this route, hydrogen fluoride (HF) solution was used instead of water, and the precursor un-

derwent a fluorination reaction ("fluorolysis"). This route was recognised as an analogue to the hydrolytic sol-gel route. Hence it was given the name "fluorolytic sol-gel route", indicating its connection to the hydrolytic route. Reaction pathways of both routes are described in 2.1.1 and 2.1.2.

2.1.1 Hydrolytic sol-gel route

The hydrolysis process was defined by J. Livage[31] as the establishment of M-OH or M=O bonds via coordination of a metal cation, M^{n+}, and water molecule (Fig. 2.2). Different compounds can be used as precursors: alkoxides, acetates, and inorganic salts like nitrates, chlorides, and sulfates.[29] Among them, metal alkoxides are probably the most frequently used precursors in the sol-gel route, because the hydrolysis of alkoxides can be simply performed by adding water to precursors.

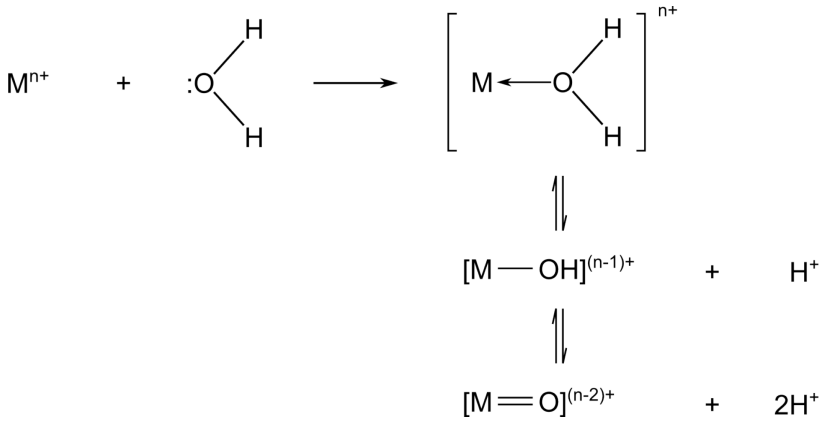

Fig. 2.2 Schematic illustration of the hydrolysis process.

Following the hydrolysis step, a condensation process happens and gives rise to the cross-linked gel-network. Releasing of water or alcohol molecules (if alkoxides are used as precursors) is typical in this process (Fig. 2.3).[32]

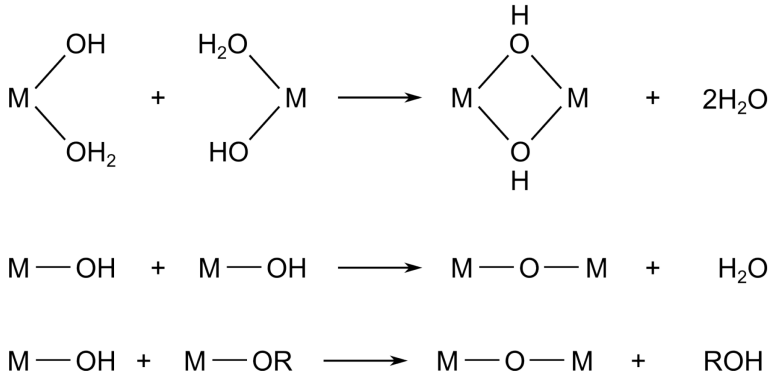

Fig. 2.3 Schematic illustration of the condensation process.

2.1.2 Fluorolytic sol-gel route

The fluorolysis process was named after the hydrolysis process.[6] It involves the formation of M-F bonds via the reaction between M^{n+} cation and HF. A typical fluorolysis process is as follows:

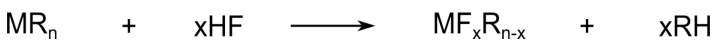

Fig. 2.4 General reaction pathway of the fluorolysis process.

The reaction may not proceed completely, leaving residual R groups; under such circumstances, a post-fluorination in the gas phase is necessary to obtain highly fluorinated products.[6]

In the fluorolytic sol-gel route, formation of M-F-M network is achieved via the direct attack of fluorine at the undercoordinated M centre (Fig. 2.5), rather than through the condensation process as in the hydrolytic sol-gel route. This is one major difference between the fluorolytic and the hydrolytic sol-gel route.

Fig. 2.5 Schematic illustration of the formation of M-F-M bonds (M-□: undercoordinated metal atom).

2.2 Fundamentals of analytical methods

2.2.1 Infrared spectroscopy (IR spectroscopy)

Infrared absorption spectra originate in photons in the infrared region that are absorbed by transitions between two vibrational levels of a molecule in the electronic ground state.[33] The total energy of the molecule can be separated into three additive components:

Eq. 2.1 $$E_{\text{total}} = E_{\text{el}} + E_{\text{vib}} + E_{\text{rot}},$$

where E_{el} associates with the motion of the electrons in the molecule, E_{vib} associates with the vibrations of the constituent atoms, and E_{rot} associates with the rotation of the molecule as a whole. If a molecule is placed in an electromagnetic field (*e.g.* light), a transfer of energy from the field to the molecule will occur when the Bohr's frequency condition is satisfied:

Eq. 2.2 $$\Delta E = h\nu,$$

where ΔE is the difference in energy between two quantised states, h is Planck's constant, and ν is the frequency of the light. Since the wavenumber ($\tilde{\nu}$) can be converted into frequency via:

Eq. 2.3 $$\tilde{\nu} = \frac{\nu}{c_n},$$

where c_n is the speed of light in the corresponding medium, the Bohr's condition is also written as:

Eq. 2.4 $$\Delta E = hc_n\tilde{\nu}.$$

Supposing that:

Eq. 2.5 $$\Delta E = E_2 - E_1,$$

thus the molecule "absorbs" ΔE when it is excited from E_1 to E_2 and "emits" ΔE when it reverts from E_2 to E_1. The vibration transitions that are observed in infrared spectra appear in the 10^2-10^4 cm^{-1} region, and originate from vibrations of nuclei constituting the molecule. It should be emphasised that not all transitions between these levels are possible. The relevant selection rule allows any transition corresponding to $\Delta v = \pm 1$ if the molecule is assumed to be a harmonic oscillator. Under ordinary conditions, however, only the fundamentals that originate in the transition from $v = 0$ to $v = 1$ in the electronic ground state can be observed. In addition to the harmonic oscillator selection rule, another restriction results from the symmetry of the molecule. Thus, the number of allowed transitions in polyatomic molecules is greatly reduced.

2.2.2 X-ray photoelectron spectroscopy (XPS)

The X-ray photoelectron spectroscopy technique is based on the photoelectron effect. Discovered by H. Hertz[34] and theoretically explained by A. Einstein,[35] this effect describes the emission of electrons (so-called photoelectrons) from sample surface after the absorption of energy from light. K. Siegbahn and his group used this effect as an analytical tool to study valence band structure and surface composition, and to identify elements and their chemical state.[36] The basic theoretical equation of this method is:

Eq. 2.6 $$h\nu = E_K + E_B + \Phi,$$

where $h\nu$ is the energy of the X-ray photons being used, E_K is the kinetic energy of the photoelectrons, E_B is the binding energy (BE) of the electron, and Φ is the work function of the spectrometer. Given $h\nu$ and Φ, E_B can be determined by measuring the E_K. Thus in an XP spectrum, intensities of photoelectrons are usually plotted versus E_B or E_K.

The XPS is usually considered as a surface-sensitive technique. The information depth of XPS for solid sample can be defined as the depth from which 95% of all the photoelectrons are scattered by the time they reach the surface. For photoelectrons of intensity I_0 emitted at a depth of d below the surface, the intensity is attenuated according to the Beer-Lambert law. Thus the intensity I_s of these photoelectrons as they reach the surface is:

Eq. 2.7 $$I_s = I_0 e^{-d/\lambda},$$

where λ is the inelastic mean free path of an electron in a solid. The information depth d_S is therefore 3λ. As λ is usually in the range of 1-3.5 nm for AlKα radiation (a commonly used X-ray source), the information depth of XPS under these conditions is 3-10 nm.

2.2.3 Mössbauer spectroscopy

The Mössbauer spectroscopy is based on the Mössbauer effect, named after its discoverer, R. Mössbauer. This effect describes the recoilless nuclear absorption of gamma radiation.[37] That is, a gamma ray emitted by one nucleus can be resonantly absorbed by nuclei of the same isotope, and this absorption is measurable. For example, a ^{57}Co source is used to generate gamma ray in studying ^{57}Fe with Mössbauer spectroscopy.

The Mössbauer spectroscopy has been established as a powerful tool for studying solid-state nuclei by providing information on electron structure, symmetry, magnetism, phase transition, and lattice dynamics. Especially, it can offer fingerprint analysis of iron-containing materials, and is therefore extremely beneficial for this work. Three types of hyperfine parameters can be interpreted from a Mössbauer spectrum. The isomer shift gives information on oxidation state, spin state, and bonding properties; the quadrupole splitting refers to oxidation state, spin state, and site symmetry; and the magnetic splitting gives information on the magnetic properties of the material under study.

2.2.4 N_2 adsorption-desorption isotherms at 77 K

Physisorption measurements are widely used for the determination of the surface area and porosity of catalysts. Physisorption (or physical adsorption) occurs whenever a gas (adsorbate) is brought into contact with a degassed solid (adsorbent). The phenomenon is brought about by the same balance of intermolecular attractive and repulsive forces that are responsible for the condensation of vapours and the deviations of real gases from ideality. Dispersion forces always provide the non-specific source of attraction between the adsorbate and the adsorbent, but there are various types of specific adsorbent-adsorbate interactions which may contribute to the interaction energies for the adsorption of polar molecules.[38]

Volumetric methods are generally used for the determination of nitrogen adsorption-desorption isotherms at 77 K. A known quantity of gas is admitted to a confined volume containing the adsorbent and the volume of gas adsorbed at the equilibrium pressure is the difference between the volume of gas admitted and that required to fill the dead space at the equilibrium pressure. The adsorption isotherm is constructed point-by-point by the admission of successive charges of gas, allowing sufficient time for equilibration at each point.

Surface area determination is achieved by the Brunauer-Emmett-Teller (B.E.T.) method.[39] A number of simplifying assumptions are introduced in the B.E.T. theory. As such, adsorption of gas molecules in the first layer is assumed to take place on an array of surface sites of uniform energy. Adsorbed molecules in the first layer act as sites for multilayer adsorption, which in the simplest case approaches infinite thickness as p approaches p_0. It is further assumed that the evaporation-condensation characteristics are identical for all the layers except the first, and that the heats of adsorption for the second and higher layers are equal to the heat of condensation of the adsorbate. Summation of the amount adsorbed in all layers then gives the isotherm equation:

Eq. 2.8
$$\frac{V}{V_{\mathrm{m}}} = \frac{cp/p_0}{(1-p/p_0)[1+(c-1)p/p_0]},$$

where V is the amount of adsorbate at the equilibrium relative pressure p/p_0, V_{m} is the monolayer capacity, and c is a constant which is correlated exponentially to the first layer heat of adsorption.

For convenience the B.E.T. equation is usually expressed in the form:

Eq. 2.9
$$\frac{p}{V(p_0-p)} = \frac{1}{V_{\mathrm{m}}c} + \frac{(c-1)}{V_{\mathrm{m}}c}\cdot\frac{p}{p_0},$$

which shows a linear relation between $p/V(p_0\text{-}p)$ and p/p_0 (*i.e.* the B.E.T. plot).

The second stage in the application of the B.E.T. method is the calculation of the surface area, S_{BET}, from the value of V_{m}. This step requires the knowledge of the average area, a_{m}, occupied by the adsorbate molecule in the complete monolayer since:

Eq. 2.10
$$S_{\mathrm{BET}} = V_{\mathrm{m}} N_{\mathrm{A}} a_{\mathrm{m}}$$

where N_{A} is the Avogadro's constant. Such a procedure is based on the assumption that, for a given adsorbate under the given temperature, the value of a_{m} remains constant and independent of the nature of the adsorbent.

3 Synthesis of transition metal fluorides

This chapter summarises the preliminary screening work of synthesising transition metal fluorides. It addresses the question why this work focused on FeF_3. At the same time, these results will provide references for further study on transition metal fluorides.

The sol-gel synthesis route of various transition metal fluorides was explored. Different combinations of precursor, solvent, and fluorination reagent were tested. The products were characterised with elemental analysis and powder XRD to determine their chemical compositions (Table 3.1).

Table 3.1 Screening results of transition metal fluorides.

Precursor	Fluorination reagent	Solvent	Dominant products
$Cr(NO_3)_3 \cdot 9H_2O$	71% HF [a]	Ethanol or methanol	Fluoride and nitrate
$Cr_3(OAc)_7(OH)_2$	71% HF	Methanol	Basic acetate
$Cr(OH)_3$	71% HF	Methanol	Fluoride
$Mn(NO_3)_2 \cdot 6H_2O$	71% HF	Methanol	Fluoride and nitrate
$MnCO_3$	71% HF	Methanol	Fluoride
$Ni(NO_3)_2 \cdot 6H_2O$	71% HF	Methanol	Nitrate
$Ni(OAc)_2 \cdot H_2O$	40% HF [b]	Methanol	Fluoride
$Ni(OAc)_2 \cdot H_2O$	71% HF	Methanol	Fluoride
$Ni(OAc)_2 \cdot H_2O$	Anhydrous HF	Methanol	Fluoride
$Zn(NO_3)_2 \cdot 6H_2O$	71% HF	Methanol	– [c]
$Zn(OAc)_2$	40% HF	Methanol	Fluoride
$Zn(OAc)_2$	71% HF	Methanol	Fluoride
$Zn(OAc)_2$	Anhydrous HF	Ethanol, methanol, or THF	Fluoride
$AgNO_3$	Anhydrous HF	Methanol	Nitrate
Ag_2CO_3	Anhydrous HF	Methanol	Fluoride
Ag(OAc)	Anhydrous HF	Methanol	Fluoride and acetate
$La(NO_3)_3 \cdot 6H_2O$	71% HF	Methanol	Fluoride and nitrate

a and b: Aqueous HF solution; c: no product available.

Not all the syntheses led to fluorides. When $Zn(NO_3)_2 \cdot 6H_2O$ was used as precursor, no powder product was formed. The obtained product was a paste-like substance that stuck to the reactor wall. It is probable that the fluorination of $Zn(NO_3)_2 \cdot 6H_2O$ proceeded only sparingly, leaving large amounts of unreacted nitrate; since the melting point of $Zn(NO_3)_2 \cdot 6H_2O$ (about 36°C) is just slightly above room temperature, the product melted and adhered to the glass reactor after calcination at 100°C, which is a regular step of the synthesis process. The fluorination of $Ni(NO_3)_2 \cdot 6H_2O$ and $AgNO_3$ were also unsuccessful, whereas $Cr(NO_3)_3 \cdot 9H_2O$, $Mn(NO_3)_2 \cdot 6H_2O$ and $La(NO_3)_3 \cdot 6H_2O$ could be partly fluorinated. In comparison, an iron nitrate precursor, $Fe(NO_3)_3 \cdot 9H_2O$, can be almost completely fluorinated as discussed in Chapter 4.

Apart from nitrate, acetate is another widely used precursor for sol-gel synthesis.[32] Indeed, $Zn(OAc)_2$ or $Ni(OAc)_2 \cdot H_2O$ are both proper precursors for the synthesis of fluorides. $Cr_3(OAc)_7(OH)_2$, however, could not be fluorinated through the sol-gel route.

Moreover, although $MnCO_3$ and Ag_2CO_3 can be fluorinated, the two synthesis processes are not sol-gel process since neither sol nor gel was formed. Adding acids or injecting CO_2 into the precursor suspension may help dissolving the carbonate, and thus may turn the synthesis to a real sol-gel process.

4 Synthesis and characterisation of partially hydroxylated FeF_3

4.1 Synthesis

4.1.1 Sol-gel synthesis route

The fluorolytic sol-gel synthesis follows a general reaction path as shown in Fig. 2.4. The precursor is first dissolved or suspended in a solvent, then fluorinated by HF solution to form a sol or a gel. Drying the sol or gel leads to the formation of a xerogel that can be applied in catalyses. Choosing a proper precursor is vitally important in order to obtain a xerogel with desirable properties. Other parameters like solvent and fluorination reagent may also affect the properties of the xerogel. Accordingly, screenings in the precursor, solvent, and fluorination reagent were performed to optimise the sol-gel synthesis route. Table 4.1 summarises the screening results with evaluations of the obtained sols and xerogels.

Table 4.1 Screening results of the synthesis of iron(III) fluoride (FeF_3).

Precursor	Fluorination reagent	Solvent	Remarks	
			Sol	Xerogel
$Fe(acac)_3$	71% HF [a]	THF	Red-brown; turbid	Low fluorination degree; leaching in catalytic tests [c]
$FeCl_3$	71% HF	Methanol	Yellow-brown; turbid	Low fluorination degree; leaching in catalytic tests
$Fe(NO_3)_3 \cdot 9H_2O$	40% HF [b]	Methanol	Colourless; clear	Highly fluorinated; active in catalytic tests
$Fe(NO_3)_3 \cdot 9H_2O$	71% HF	Methanol	Colourless; clear	Highly fluorinated; active in catalytic tests
$Fe(NO_3)_3 \cdot 9H_2O$	Anhydrous HF	Methanol	Colourless; clear	Highly fluorinated; active in catalytic tests
$Fe(NO_3)_3 \cdot 9H_2O$	Anhydrous HF	Ethanol	Colourless; turbid	Highly fluorinated; inactive in catalytic tests
$Fe(NO_3)_3 \cdot 9H_2O$	Anhydrous HF	THF	Yellow; clear	Highly fluorinated; non-selective in catalytic tests

a and b: Aqueous HF solution; c: the isomerisation reaction of citronellal to isopulegols was taken as the model reaction in catalytic test, and detailed descriptions of the catalytic test are given in Chapter 7.

The screening results suggest that both solvent and iron precursor play a vital role in preparing highly fluorinated xerogels. Especially, changing the anions of iron precursors can lead to totally different results. J. Livage *et al.*[32] discussed the role of anions during the sol-gel synthesis. Their work pointed out that in a hydrolytic sol-gel process, when inorganic salts were used as precursors, the electronegativity of the anions should not be too high; it should be only slightly higher than the solvent in order to form a solvated complex that can further react to give rise to colloidal sol particle or gel network. Similarly, in the fluorolytic sol-gel process, one needs to compare the electronegativity of anions and the solvent. The comparison between iron chloride and iron nitrate in methanolic solution offers an example: the electronegativity of methanol (χ_{met}) is 2.40,[40] while the χ_{Cl} of Cl^- is 3.16 and the χ_N of NO_3^- is 2.76;[32] thus when iron nitrate was used as precursor, it may form the solvated complex that can be further fluorinated. With the help of elemental analysis and catalytic tests, the following combination was therefore selected as an optimal choice: iron nitrate nonahydrate ($Fe(NO_3)_3 \cdot 9H_2O$) as the precursor, methanol as the solvent, and anhydrous HF solution as the fluorination reagent. Through this route, a colourless and transparent FeF_3 sol was successfully prepared (Fig. 4.1 (A)). Drying the sol led to the formation of FeF_3 xerogel. The powder XRD pattern shows the obtained FeF_3 contains one equivalent water (Fig. 4.1 (B)). The broad reflexes indicate its low crystallisation degree, which is one common feature shared by many nanoscopic metal fluorides.[8]

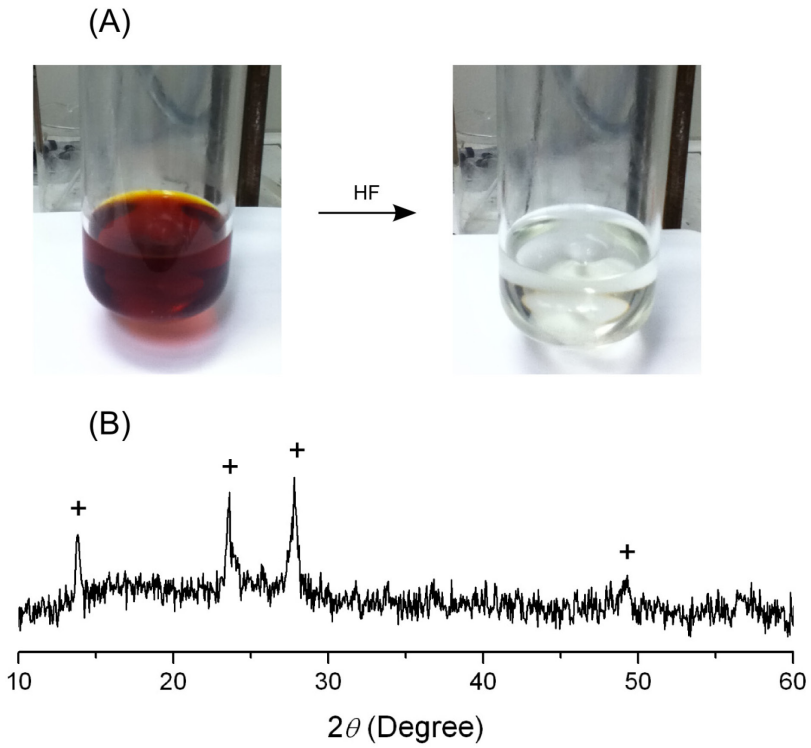

Fig. 4.1 (A) Images of $Fe(NO_3)_3 \cdot 9H_2O$ solution (left) and FeF_3 sol (right); (B) the powder XRD pattern of FeF_3 xerogel (+ refers to an $FeF_3 \cdot H_2O$ phase in PDF 26-783).

4.1.2 Pre-dehydration treatment

Since this work aims at developing a catalyst with both Lewis and Brønsted acidity, hydroxyl groups acting as the potential Brønsted acid sites have to be introduced onto FeF_3. Depending on precursors, distinct methods are available to this purpose. Metal alkoxides have been used in the synthesis of partially hydroxylated AlF_3 or

MgF_2.[12, 15] In this route, an aqueous HF solution was sufficient to initiate fluorolysis and hydrolysis in a single step, resulting in $M(OH)_xF_{n-x}$ xerogels. In contrast, with the iron nitrate precursor, $Fe(NO_3)_3 \cdot 9H_2O$, this route would have only led to the formation of iron fluoride monohydrate and hence was not an option. On the other hand, thermal dehydration treatment of iron nitrate precursor gives rise to iron hydroxy nitrate; through this way, hydroxyl groups can be introduced before the fluorination step. Fig. 4.2 (A) shows the dehydration pathway of $Fe(NO_3)_3 \cdot 9H_2O$ according to K. Wieczorek-Ciurowa and A. J. Kozak.[41] It suggests that the suitable temperature range of the dehydration process is 50-150°C. An optimal pre-dehydration temperature of 65°C was found with the help of catalytic tests (see 7.2.1). The weight loss during the pre-dehydration process was determined, suggesting the chemical composition of the partially dehydrated iron nitrate (Fig. 4.2 (B)). It was then used as the precursor in the sol-gel synthesis to prepare the partially hydroxylated FeF_3. For brevity, the term "FeF_3" refers to partially hydroxylated species in the following text unless otherwise stated.

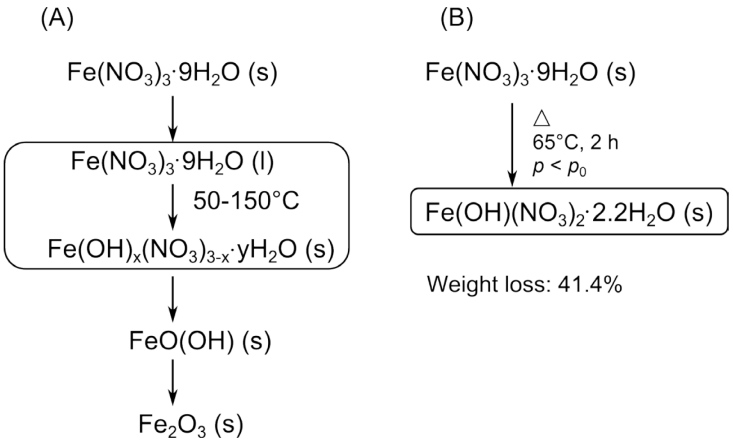

Fig. 4.2 (A) Schematic diagram of thermal treatment of $Fe(NO_3)_3 \cdot 9H_2O$; (B) chemical composition of partially dehydrated iron nitrate precursor; s refers to solid state and l refers to liquid state. Fig. (A) is adapted from K. Wieczorek-Ciurowa *et al.*[41]

4.2 Bulk characterisation of partially hydroxylated FeF_3

4.2.1 Chemical composition

The dried xerogel of the partially hydroxylated FeF_3 appeared pale green (Fig. 4.3 (A)), the characteristic colour for iron(III) fluoride. To prove the existence of hydroxyl groups in FeF_3, it was first investigated by IR spectroscopy. The IR spectrum was recorded after removing the surface impurities and weakly bonded water species by heating the sample at 200°C under high vacuum (Fig. 4.3 (B)). The weak vibration band at 1640 cm^{-1} probably results from strongly bonded water species in small quantity. However, its low intensity cannot explain the strong vibration bands of –OH at 3597, 3333, and 3167 cm^{-1}. Similar results have been found in the IR spectrum of ZnF_2 and these –OH vibration bands have been taken as evidences for the formation of Zn–OH bonds.[42] Similarly, the IR spectrum of FeF_3 confirms the existence of Fe–OH bonds. However, since the ordinary IR spectroscopy is not a surface-sensitive technique, it cannot discriminate surface hydroxyl groups from those in the

bulk. Therefore IR spectroscopy coupled with chemisorption of probe molecules is needed to solve this problem. The relevant results are discussed in 4.3.2.

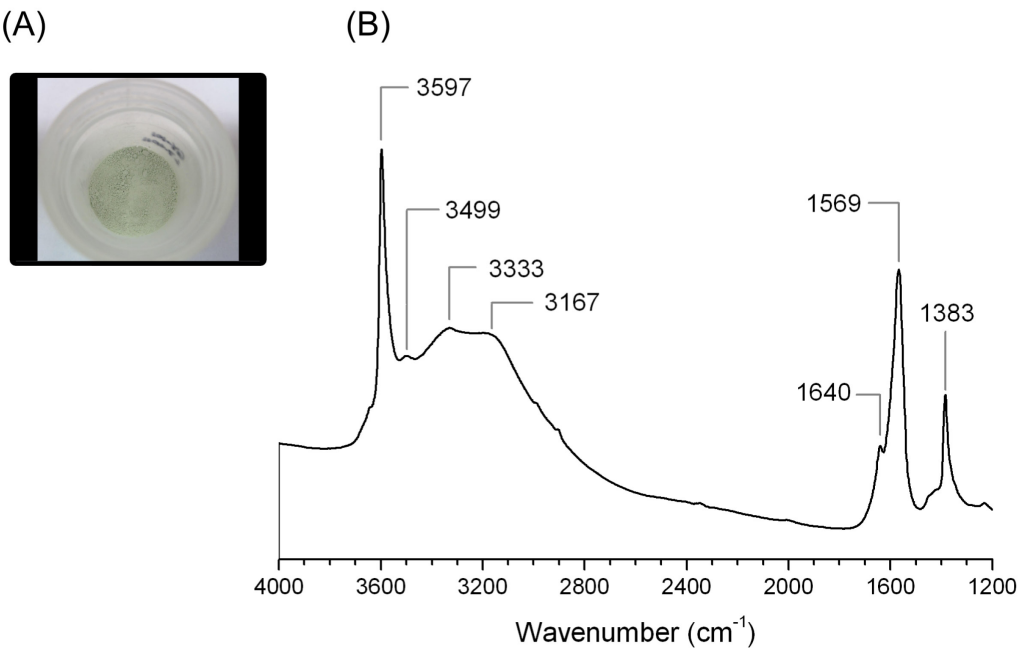

Fig. 4.3 (A) Image of partially hydroxylated FeF_3 xerogel; (B) IR spectrum of partially hydroxylated FeF_3 after activation at 200°C under vacuum.

The chemical composition of the partially hydroxylated FeF_3 was determined jointly by elemental and thermal analyses. Elemental analysis provided the content of single elements (C, H, N, and F), while thermal analysis coupled with mass spectrometry (MS) recorded the weight loss and ionic fragments released during heating (Fig. 4.4).

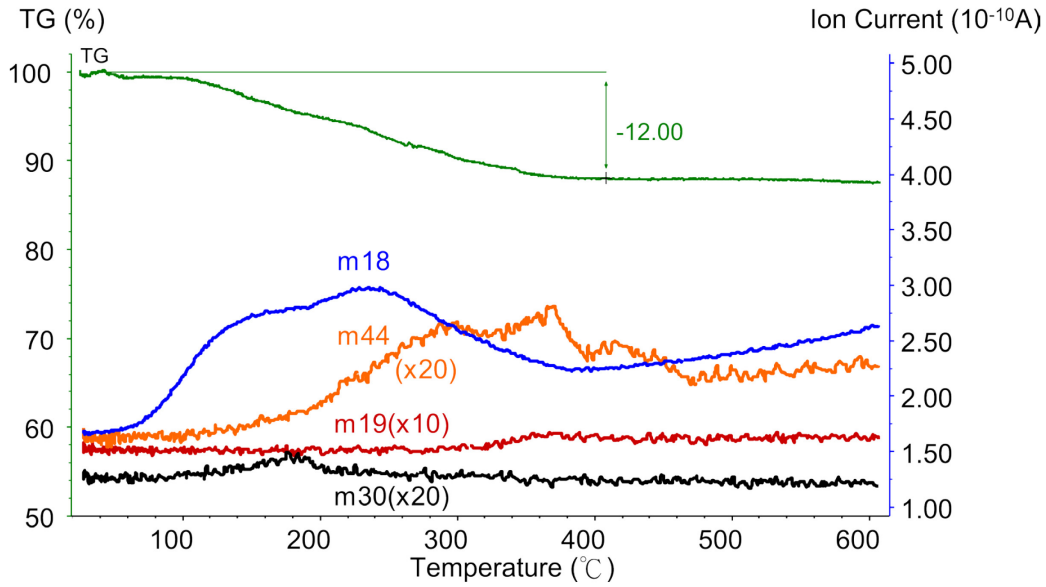

Fig. 4.4 TG curve and MS profiles of partially hydroxylated FeF_3; assignments of the ionic fragments: m18 (H_2O^+), m19 (F^+), m30 (NO^+), and m44 (CO_2^+).

In the MS profiles of FeF_3, the m/z = 18 species may result from released water or hydroxyls. The amount of released F^+ (m/z = 19) is insignificant, suggesting that FeF_3 is thermally stable. NO^+ (m/z = 30) can be traced back to the residual nitrate. At the same time, the carbon source is probably some solvent molecules adsorbed or coordinated to FeF_3. These organic species were probably oxidised to CO_2^+ (m/z = 44) by the released NO_x (NO or NO_2). The chemical composition of FeF_3 was calculated by using the results of elemental analysis. The few coordinated solvent molecules are omitted to simplify the formula. Though NO_x species have been detected by thermal analysis, the N content is below the detection limit of elemental analysis, probably because of its low concentration. Thus no NO_3^- appears in the chemical formula of FeF_3 (Table 4.2). The weight loss determined by the thermogravimetry (TG) curve was used to verify the calculated result.

Table 4.2 Results of elemental analysis of partially hydroxylated FeF_3.

Sample	Element (wt%)				Calculated composition
	C [a]	H [a]	N [a]	F [b]	
FeF_3	0.5	1.3	– [c]	40.6	$FeF_{2.7}(OH)_{0.3}\cdot 0.6H_2O$

a: Error range (confidence interval): ± 0.3%; b: error range: ± 2.0%; c: below the detection limit.

4.2.2 Structure and morphology

The partially hydroxylated FeF_3 xerogel was further investigated by electron microscopy. High-resolution transmission electron microscopy (HRTEM) image shows FeF_3 crystallites with clear lattice planes (Fig. 4.5 (A)). The diameter of the spotted crystallites is about 10 nm, confirming the nanoscopic nature of FeF_3. The scanning transmission electron microscopy (STEM) image is also provided (Fig. 4.5 (B)) as a direct proof of the porous features.

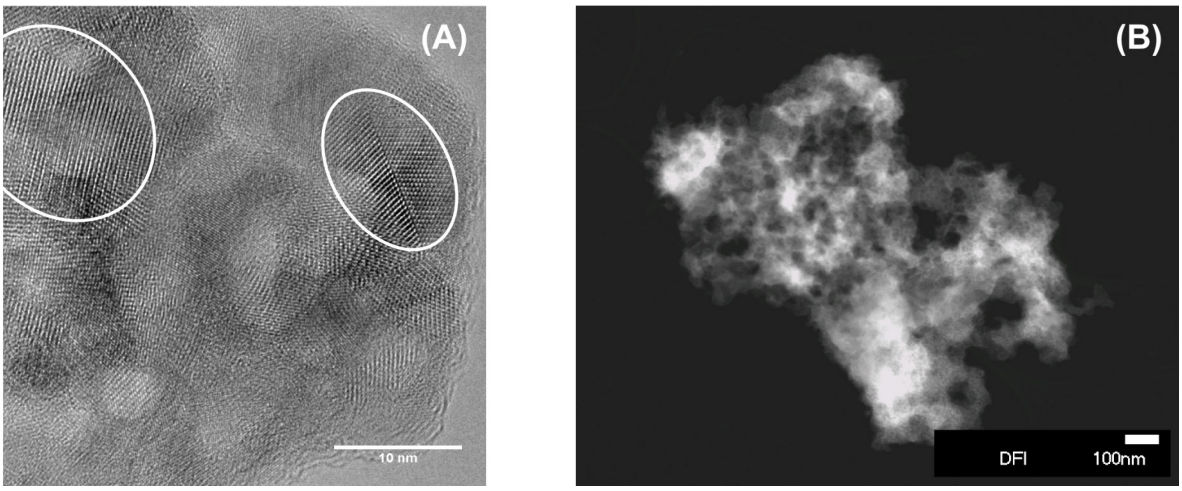

Fig. 4.5 (A) HRTEM image (scale: 10 nm); (B) STEM image (scale: 100 nm) of FeF_3.

STEM differs from conventional TEM by focusing the electron beam into a narrow spot which is scanned over the sample in a raster. Equipped with a high-angle annular dark-field (HAADF) detector, STEM is possible to provide images with atomic resolution. The signal intensity is related to the atomic number and thickness of the sample.[43] Since iron is a relatively heavy element, it is possible to obtain high-quality STEM images. Indeed, the STEM image confirms that FeF_3 contains mainly meso-/macropores (pore diameter of 50-100 nm) that are composed of the voids between aggregates or agglomerates. A thorough study of porosity can be found in 4.3.1 by N_2 adsorption-desorption measurements.

4.3 Surface characterisation of partially hydroxylated FeF_3

Because heterogeneous catalysis is a surface phenomenon, surface characteristics of the partially hydroxylated FeF_3 is the focus of this chapter. The porous features as well as the surface acidity jointly decide the potential of FeF_3 in heterogeneous catalysis. To determine them, N_2 physisorption and IR spectroscopy hyphenated with chemisorption of selected probe molecules were applied.

4.3.1 Surface area and porosity

The N_2 adsorption-desorption isotherms of FeF_3 at 77 K are given in Fig. 4.6. It shows the main features of type II isotherms that refers to macroporosity, with a type H3 hysteresis loop[39] that corresponds to pores of nonuniform size. Indeed, the STEM image (Fig. 4.5 (B)) shows clearly the existence of macropores with pore diameter of about 100 nm; and since the average pore diameter of FeF_3 is 33 nm, which lies in the mesopores range, there should be some smaller pores in this sample. Not only the pore size but also the surface area can be calculated from the isotherms. FeF_3 exhibits relatively small surface area of 40 $m^2 \cdot g^{-1}$. However, high-surface material is expected to have advantages in heterogeneous catalysis. The target of preparing high-surface catalysts was achieved by synthesising ternary fluorides as described in Chapter 5 and 6.

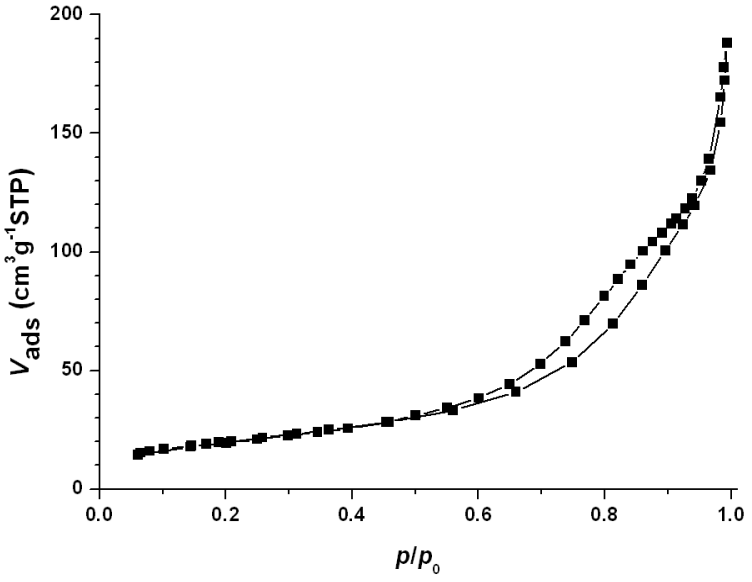

Fig. 4.6 N_2 adsorption-desorption isotherm of FeF_3; p/p_0: relative pressure, V_{ads}: quantity of adsorbed N_2.

4.3.2 Surface acidity

The chemisorption-IR with probe molecules is a very powerful technique in studying surface acidity. Two different kinds of probe molecules (NH_3 and CD_3CN) were used to determine the types and strengths of surface acid sites. NH_3 can interact with acid sites of a solid surface in different ways.[44] This work focused on three of them:

(1) protonation with surface hydroxyl groups (strong or medium strong Brønsted acid sites);

(2) coordination to electron-deficient metal atoms (Lewis acid sites);

(3) hydrogen-bonding via the nitrogen atom of the ammonia (weak Brønsted acid sites).

The differential spectra of FeF_3 after NH_3 adsorption are given in Fig. 4.7. The intensive band at 1430 cm^{-1} band can be assigned to protonated NH_4^+ species, indicating the existence of Brønsted sites. Additionally, this band shifts slightly towards lower wavenumbers ($\Delta\delta$ = 20 cm^{-1}) compared with the vibration frequency of protonated NH_4^+ on alumina surface (δ = 1450 cm^{-1}).[45] It suggests that the Brønsted acidity of FeF_3 is probably weaker than that of alumina, which is commonly recognised as a strong acid. The vibration band at 1251 cm^{-1} and the broad shoulder at 1194 cm^{-1} can be assigned to the coordinated NH_3 species that indicate for surface Lewis sites. The peak at a lower wavenumber (1143 cm^{-1}) corresponds to the H-bonding species that is typical for weak Brønsted sites.

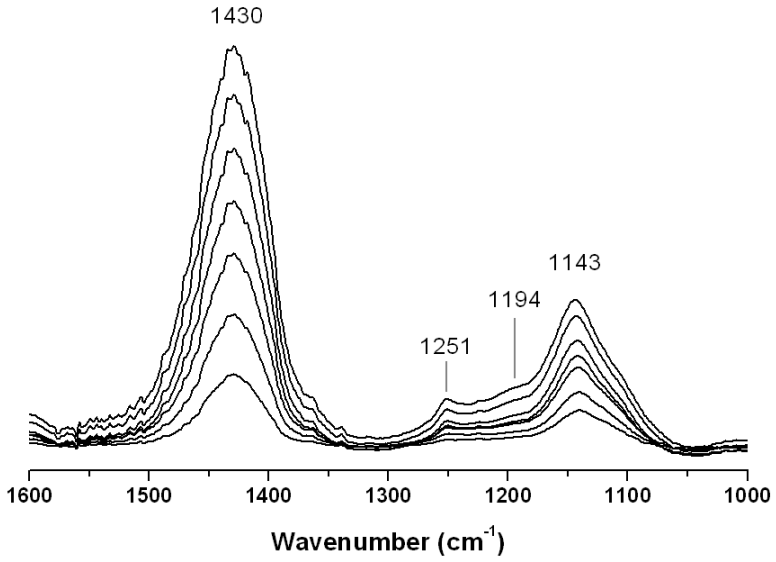

Fig. 4.7 Differential IR spectra of FeF_3 saturated stepwise with NH_3.

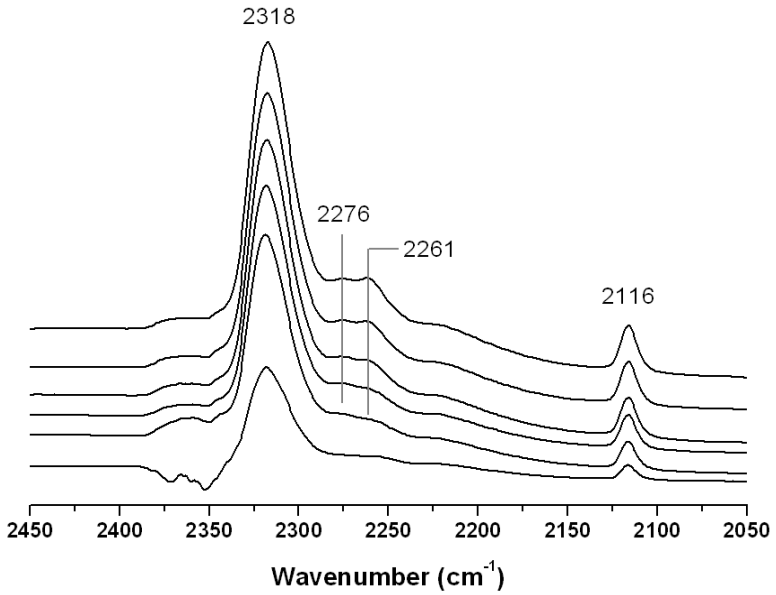

Fig. 4.8 Differential IR spectra of FeF_3 saturated stepwise with CD_3CN.

CD_3CN is another widely used probe molecule because it can interact with both Lewis and Brønsted acid sites.[5, 46] Especially, the well-known *trio* bands are characteristic for strong Brønsted acid sites. It refers to the simultaneous occurrence of three bands at about 2890, 2400, and 1700 cm^{-1}.[5] In the differential spectra of FeF_3 (Fig. 4.8), the trio bands are missing, indicating that the Brønsted acid sites on the FeF_3 surface are not strong enough to form an H-complex with CD_3CN. This result is in agreement with the red-shift of the 1430 cm^{-1} band in the NH_3-chemisorption IR spectra (Fig. 4.7). The band at 2116 cm^{-1} corresponds to the symmetric CD stretching; the asymmetric CD stretching is too weak to be detected.[46] The bands at 2261 and 2276 cm^{-1} are largely reduced after evacuation, suggesting that they are probably caused by physisorbed species. The intensive band at 2318 cm^{-1} is characteristic for coordinated CD_3CN species on medium strong or strong Lewis acid sites. Its frequency shifts by about 13 cm^{-1} to lower wavenumbers as compared with aluminium hydroxy fluoride.[13] This implies that the Lewis acidity of partially fluorinated FeF_3 is weaker than that of aluminium hydroxy fluoride, which is in line with the electronegativity order of Fe (χ_{Fe} = 1.83) and Al (χ_{Al} = 1.61).[47]

4.4 Summary

This chapter discussed the synthesis strategy and characterisation results of nanoscopic FeF_3, a potential heterogeneous catalyst. A modified sol-gel route was established for the preparation of this nanomaterial. Thanks to a pre-dehydration treatment of the iron nitrate precursor, hydroxyl groups were successfully introduced on the surface of FeF_3. Bulk and surface properties of this partially hydroxylated FeF_3 were characterised by different analytical methods. It was proved to be a nanocrystalline material with macroporosity. More importantly, using chemisorption-IR, both Lewis and Brønsted acid sites were determined on the surface. Complementary probe

molecules were employed for the IR investigation; and the results suggested that strong Lewis sites and medium strong Brønsted sites are predominant on the surface.

In short, surface hydroxyl groups were generated by the pre-dehydration of iron nitrate, and more important, were preserved after the fluorolysis process. This chapter provided a synthesis route that is simple to perform for partially hydroxylated FeF_3 materials with surface bi-acidity. This type of materials can be useful in various acid-catalysed reactions. However, the relatively small surface area may limit its potential as a heterogeneous catalyst. Thus the follow-up work should concentrate on synthesising FeF_3-based high-surface materials. To this end, Chapter 5 offers a solution.

5 Synthesis and characterisation of ternary FeF_3-MgF_2

5.1 Synthesis

Chapter 4 describes the development of partially hydroxylated FeF_3. So far, hydroxyl groups have been successfully introduced on the surface of FeF_3 via the pre-dehydration treatment of iron precursor. However, the obtained FeF_3 showed relatively low surface area of about 40 $m^2 \cdot g^{-1}$. Since FeF_3 was to be used as a heterogeneous catalyst, high surface area is preferred because all the active sites are on the surface. In order to prepare a high-surface material, FeF_3 was dispersed in a nanoscopic MgF_2 matrix; thus a new class of materials was obtained. A one-step fluorination of the mixed Fe and Mg precursors led to the formation of ternary FeF_3-MgF_2 (denoted as fm-*n*, *n* refers to the molar Mg-to-Fe ratio). The synthesis route is shown in Fig. 5.1 (A). Pure nanoscopic MgF_2 was also prepared as a reference.

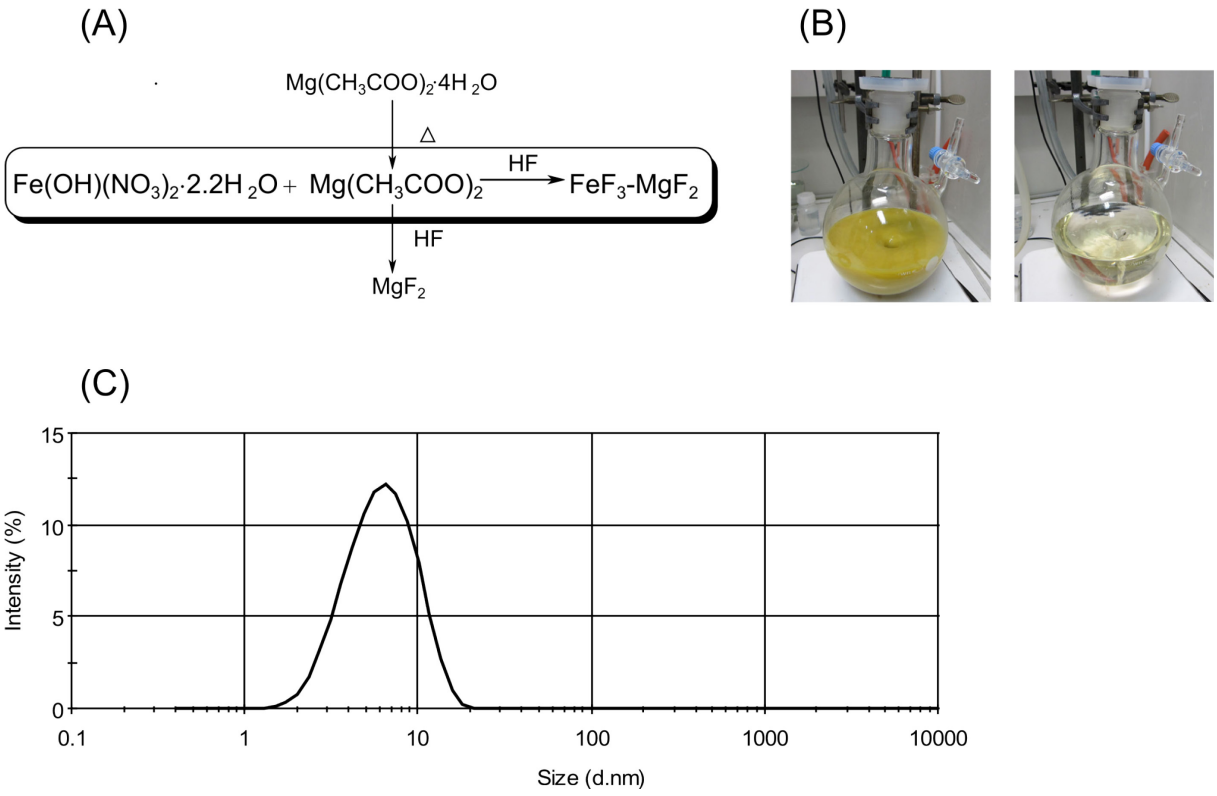

Fig. 5.1 (A) Schematic illustration of the one-step synthesis of ternary FeF_3-MgF_2; (B) images of mixed Fe-Mg precursors suspension (left, the molar Mg-to-Fe ratio = 2:1) and the corresponding fm-2 sol (right); (C) fm-2 sol particle size distribution by intensity from DLS measurement (d.: diameter).

Fig. 5.1 (B) shows the images of one representative sample, fm-2, before and after fluorination. Similar to the synthesis of FeF_3, a clear FeF_3-MgF_2 sol was obtained. In order to determine the particle size distribution in the

sol, the fm-2 sol was studied by dynamic light scattering (DLS). As shown in Fig. 5.1 (C), the hydrodynamic diameter of fm-2 sol particles follows an approximate log-normal mono-distribution with the mean at about 6 nm. The result reveals the nanoscopic nature of the ternary FeF_3-MgF_2.

5.2 Bulk characterisation

5.2.1 Chemical composition

Chemical composition of FeF_3-MgF_2 was determined by elemental and thermal analyses. Fig. 5.2 shows the TG curve and MS profiles of one representative FeF_3-MgF_2 sample, fm-2. Similar to FeF_3 (see Fig. 4.4), FeF_3-MgF_2 undergoes a single-step decomposition during the heating run. The weight loss was mainly caused by the release of water and hydroxyls (m/z = 18). The release of NO^+ (m/z = 30) was also recorded, indicating the existence of residual nitrate. The assignment of the m/z = 44 species was not straightforward. Its ion current curve shows three different peaks. The one between 100 and 150°C is accompanied by the release of NO^+ and thus can be assigned to CO_2^+ from organic rests (acetate or solvent) that oxidised by NO_x; similar results have been discussed in 4.2.1. The other two peaks in higher temperature range may result from the direct decomposition of acetate. The F^+ ion current curve (m/z = 19) shows a broad peak at higher than 250°C, suggesting that FeF_3-MgF_2 is thermally less stable at higher temperature. This is probably caused by the interference of Mg into Fe, as discussed in the structural characterisation part (5.2.2).

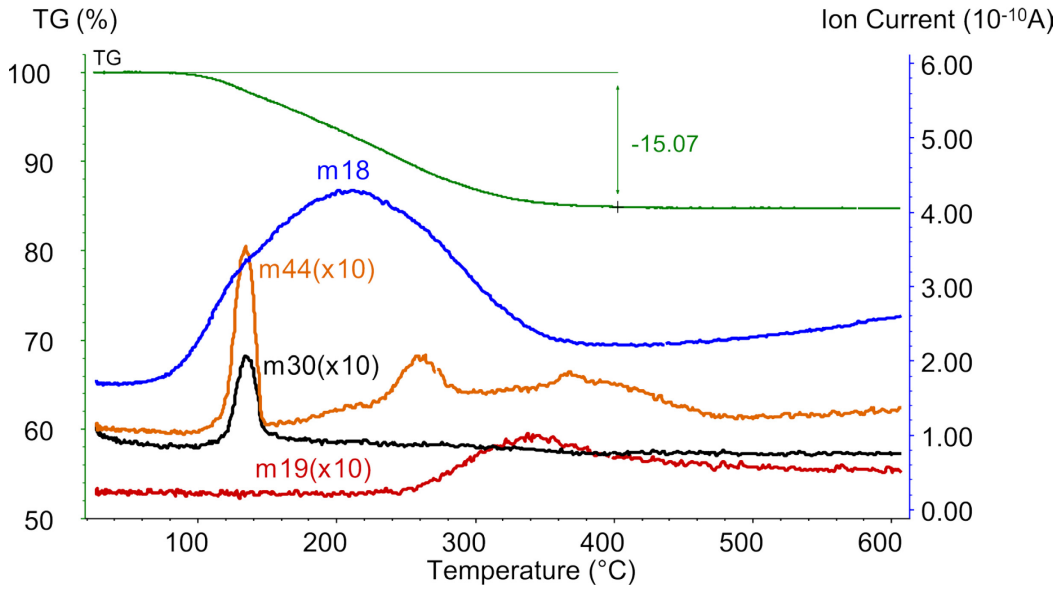

Fig. 5.2 TG curve and MS profiles of fm-2; assignments of the ionic fragments: m18 (H_2O^+), m19 (F^+), m30 (NO^+), and m44 (CO_2^+).

Moreover, it is noticeable that most organic residuals and water (or hydroxyls) were removed before 200°C, a relatively low temperature compared with that of other acetate containing fluoride, *e.g.* ZnF_2.[42] One possible explanation is that the released NO_x species act as oxidant and their presence may decrease the decomposition temperature of organic rests. Similar effect of nitrate salt has been reported by X.H. Liu *et al.*,[48] who found the organic template was removed at lower temperature when nitrate participated. Thus it is possible to obtain an organic-free FeF_3-MgF_2 sample by isothermal heating at low temperature. Fig. 5.3 shows the TG curve and corresponding MS profiles of fm-2 under isothermal treatment at 200°C. As expected, the total weight loss is in line with that from the first measurement (Fig. 5.2). The CH_3^+ species (m/z = 15) that originates from solvent and residual acetates shows a broad peak and a spike. As the spike in the curve of CH_3^+ species appears at exactly the same position of the CO_2^+ and NO^+ peaks, the result confirms that NO_x species can catalyse the oxidation and decomposition of organic residuals.

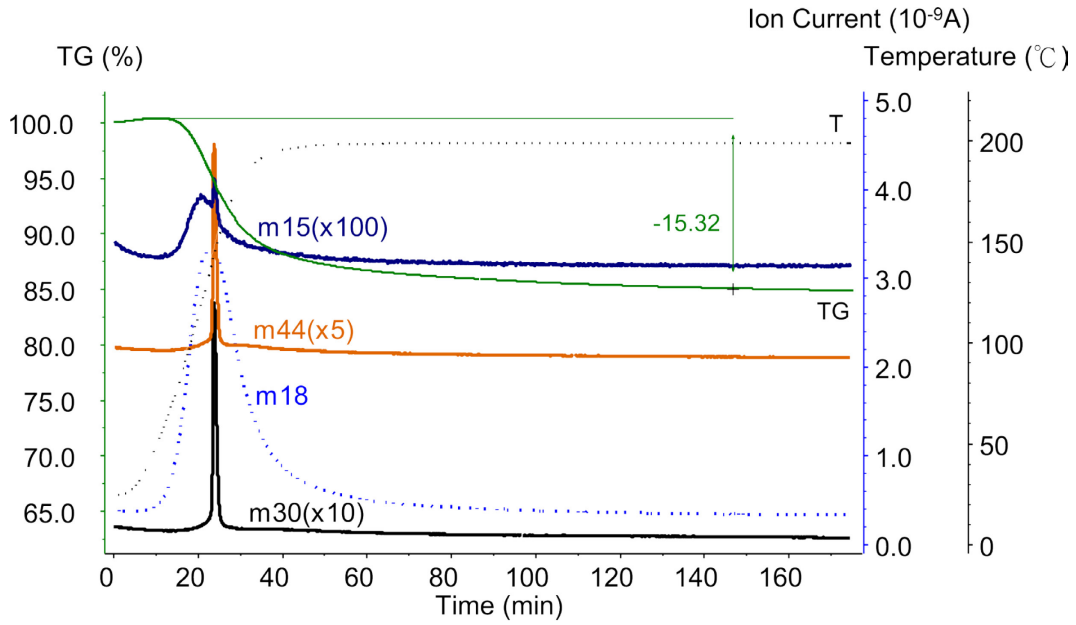

Fig. 5.3 TG curve and MS profile of fm-2 under heating with isotherm-plateau at 200°C; assignments of the ionic fragments: m15 (CH_3^+), m18 (H_2O^+), m30 (NO^+), and m44 (CO_2^+).

Table 5.1 Results of elemental analysis of fm-*n* samples and MgF_2.

Sample	Element (wt%)				Calculated composition	Fluorination degree [d]
	C [a]	H [a]	N [a]	F [b]		
fm-1	0.5	1.4	0.4	36.9	$FeMgF_{3.6}(OH)_{1.3}(NO_3)_{0.06}(OAc)_{0.04}\cdot 0.6H_2O$	0.72
fm-2	0.6	1.5	– [c]	42.8	$FeMg_2F_{5.9}(OH)_{1.0}(OAc)_{0.1}\cdot 1.4H_2O$	0.84
fm-3	0.3	1.3	0.5	40.7	$FeMg_3F_{7.7}(OH)_{1.1}(NO_3)_{0.1}(OAc)_{0.1}\cdot 2.1H_2O$	0.85
MgF_2	7.8	1.8		37.2	$MgF_{1.7}(OAc)_{0.3}\cdot 0.8H_2O$	0.85

a: Error range: ± 0.3%; b: error range: ± 2.0%; c: below detection limit; d: fluorination degree: [F]/(3[Fe]+2[Mg]).

Table 5.1 summarises the elemental analysis results of FeF_3-MgF_2 and MgF_2. Based on experimental results, the fluorination degree of FeF_3-MgF_2 was calculated and listed in the table as well. The fluorination degree is defined as the ratio of experimental and theoretical values of F content, and hence its upper limit is 1. Generally, FeF_3-MgF_2 samples are highly fluorinated. With increasing amount of MgF_2, the fluorination degree of FeF_3-MgF_2 grows slightly and approaches the limit of 0.85. Compared with FeF_3, the FeF_3-MgF_2 samples contain more hydroxyl groups: the OH-to-Fe ratio of FeF_3-MgF_2 is about 1.0, which is two times higher than that of FeF_3 (Table 4.2). Since these hydroxyls are potential Brønsted acid sites, the ternary FeF_3-MgF_2 samples probably have an advantage over FeF_3.

5.2.2 Structural characterisation

Structural characteristics of FeF_3-MgF_2 were acquired by powder XRD and Mössbauer spectroscopy. XRD patterns of a series of FeF_3-MgF_2 samples were recorded. The fm-1 sample (Fig. 5.4 (A): (a)) is amorphous, without reflexes of any phases; with increasing MgF_2 content, the FeF_3-MgF_2 samples (Fig. 5.4 (A): (b) and (c)) begin to show features of a MgF_2 phase. The XRD patterns of fm-2 and its residual after thermal analysis are shown in Fig. 5.4 (B). After heated up to 600°C, the fm-2 residual shows separated FeF_3 and MgF_2 phases in XRD patterns. No evidence of a mixed Fe-Mg-fluoride phase was observed.

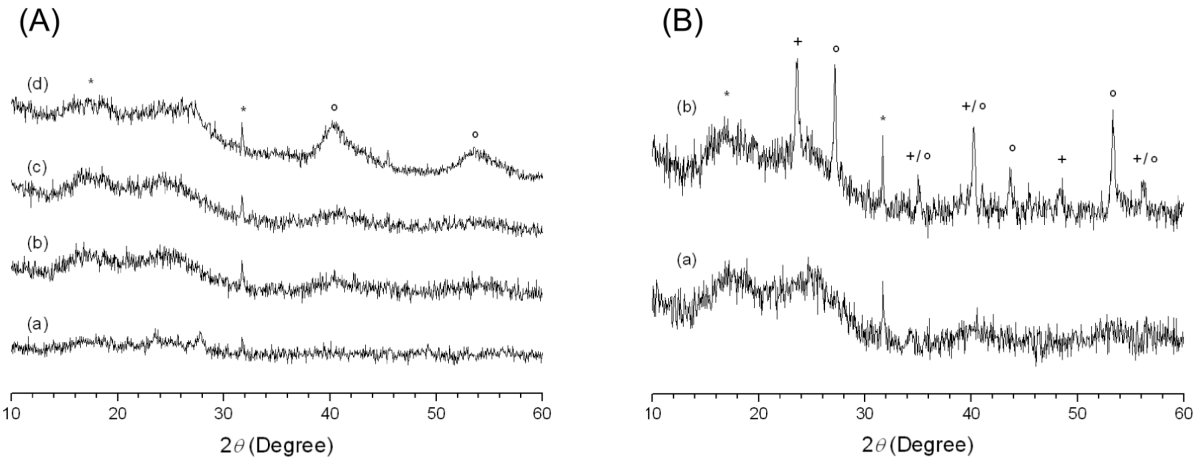

Fig. 5.4 (A) Powder XRD patterns of (a) fm-1 (b) fm-3 (c) fm-6 and (d) MgF_2; (B) powder XRD patterns of fm-2 (a) original and (b) after thermal analysis; * refers to reflexes from the sample holder, + refers to an FeF_3 phase in PDF 33-647, and ° indicates for MgF_2 in PDF 1-1196.

Mössbauer spectroscopy is a very powerful method for the study of local structure and magnetic properties of iron containing materials. Two FeF_3-MgF_2 samples, fm-2 and fm-9, were studied by this technique. The results of FeF_3 are provided as references. First of all, an investigation in literature shows that FeF_3 of rhombohedral structure (r-FeF_3) possesses a long-range magnetic order at room temperature and thereby exhibits a Zeeman-split six-line spectrum. In its paramagnetic state, T > 363 K, r-FeF_3 exhibits a single line spectrum indicating zero or negligibly small quadrupole splitting (see Table 5.2).[49] In contrast, nanoscopic FeF_3, which has been

termed amorphous FeF_3 (a-FeF_3) at room temperature, exhibits a quadrupole doublet with broad lines,[50] indicating a lack of magnetic interactions and a lower than cubic symmetry at the Fe site.

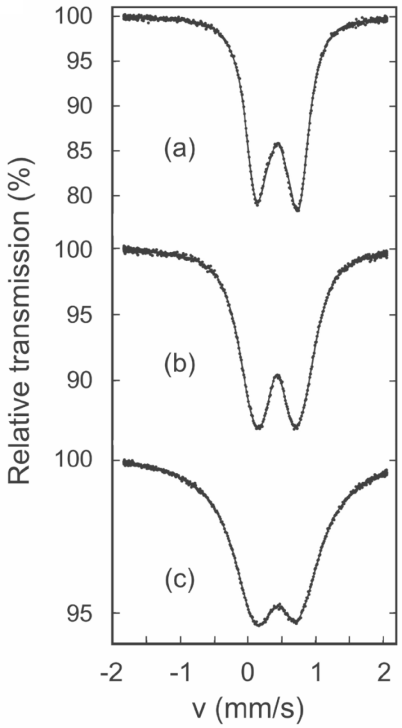

Fig. 5.5 ^{57}Fe Mössbauer spectra of (a) FeF_3, (b) fm-2, and (c) fm-9.

Table 5.2 Parameters from ^{57}Fe Mössbauer spectra of FeF_3, fm-2, fm-9 and literature values for amorphous FeF_3 (a-FeF_3) and crystalline FeF_3 (r-FeF_3).

Sample	IS[a] (mm/s)	<QS[b]> (mm/s)	$<QS^2>^{1/2}$	Standard deviation σ (mm/s)	T_t[c] (K)	B[d] (T)
FeF_3	0.45	0.58	0.50	0.30		
fm-2	0.43	0.73	0.56	0.47		
fm-9	0.43	0.96	0.60	0.75		
a-FeF_3[e]	0.45−0.46	0.55−0.58			30−40	53−56
r-FeF_3[e]	0.49	0	0	0	363	61.8

a: Isomer shift; b: quadrupole splitting; c: magnetic transition temperature; d: local magnetic field at 4.2 K; e: see references[49, 50].

The room temperature spectra of the sol-gel prepared FeF_3 as well as fm-2 and fm-9 samples also exhibit a broad doublet (Fig. 5.5) with the parameters for FeF_3 being in excellent agreement with the literature values for a-FeF_3 (Table 5.2). This agreement and the lack of magnetic hyperfine lines confirm the nanoscopic nature of the sol-gel prepared FeF_3. The broadening of the doublet indicates the existence of a large number of slightly different Fe

surroundings. The slight asymmetry of the spectrum of FeF_3 may be due to weak correlation between isomer shift (IS) and quadrupole splitting (QS). The latter can be induced by the local variation of chemical bonding due to the introduced OH groups which coordinate to the Fe atoms and result in different partially fluorinated $FeF_{6-x}O_x$ units. Similar structural units have been confirmed by ^{19}F MAS NMR in partially hydroxylated MgF_2.[51] In addition, residual nitrate and coordinative H_2O may also contribute to these oxygen-containing units.

The fitted parameters of the ^{57}Fe Mössbauer spectra of the FeF_3-MgF_2 samples are summarised in Table 5.2. The magnitude of the isomer shift indicates that Fe atoms in all the samples are in the +3 formal oxidation state in an octahedral coordination by fluorine.[52] The non-zero quadrupole splitting and the broadened line shape reflect the random distortion of the octahedral coordination and structural disorder. The increasing magnitude of the mean value of quadrupole splitting (<QS>) with increasing MgF_2 indicates the increase in the asymmetry around Fe atoms whereas the increase in the root mean square ($<QS^2>^{1/2}$) and standard deviation (σ) reflects the increase between minimal and maximal asymmetry around Fe atoms. In conclusion, the increasing MgF_2 content leads to increasing disturbances of the Fe coordination polyhedra. Apparently, this indicates an at least partial mixing of iron and magnesium ions at the atomic level.

5.2.2.1 Discussion: interaction between FeF_3 and MgF_2 in ternary fluorides

The Mössbauer spectra of FeF_3-MgF_2 samples reflect the structural interference between MgF_2 and FeF_3. However, the origin of this interaction remains unclear. Two supplementary experiments were therefore designed for further investigation. Another two FeF_3-MgF_2 samples were prepared with the Mg-to-Fe ratio of 2 to 1. One sample was synthesised via the mechano-milling of FeF_3 and MgF_2 xerogels (Mech-fm-2). The other was prepared by drying the mixed FeF_3 and MgF_2 sols which were fluorinated separately (Mix-fm-2).

Table 5.3 Comparison of fm-2, Mech-fm-2, Mix-fm-2, and FeF_3 in surface area, pore size, and catalytic activity.

Sample	Preparation method	Surface area ($m^2 \cdot g^{-1}$)	Average pore diameter (nm)	Conversion of (±)-citronellal [a] (%)	Selectivity to (±)-isopulegols [a] (%)
fm-2 [b]	One-step fluorination	440	2.4	94 [c]	82 [c]
Mech-fm-2	Mechano-milling	80	4.7	26 [d]	46 [d]
Mix-fm-2	Mixed-sols of FeF_3 and MgF_2	460	2.6	90 [c]	79 [c]
FeF_3		70	13.4	33 [d]	52 [d]

a: Chapter 7 gives details of the model reaction: citronellal→isopulegols;

b: synthesis of fm-2 was repeated to test the reproducibility, and results of other fm-2 samples can be seen in 5.3.1 and 7.2.2;

c: with 5 mg FeF_3; d: with 10 mg FeF_3.

Subsequently, these two samples were characterised by N_2 adsorption-desorption measurement and their catalytic activity was tested with the model reaction (see Chapter 7). The sample from mixed sols was almost identical to the fm-2 sample in surface area and catalysis tests, whereas the mechano-milled sample showed properties similar to FeF_3 (Table 5.3).

Moreover, X-ray photoelectron spectroscopy (XPS) was used to investigate these FeF_3-MgF_2 samples prepared through different routes. XPS is a very useful technique in studying the electronic structure of solids. Especially, the core-level XPS shows the chemical shift, in which the binding energies (BE) of elements shift because of different chemical environments. This phenomenon is widely used to investigate the chemical bondings of various materials. Therefore it is also named as ESCA (electron spectroscopy for chemical analysis).[36]

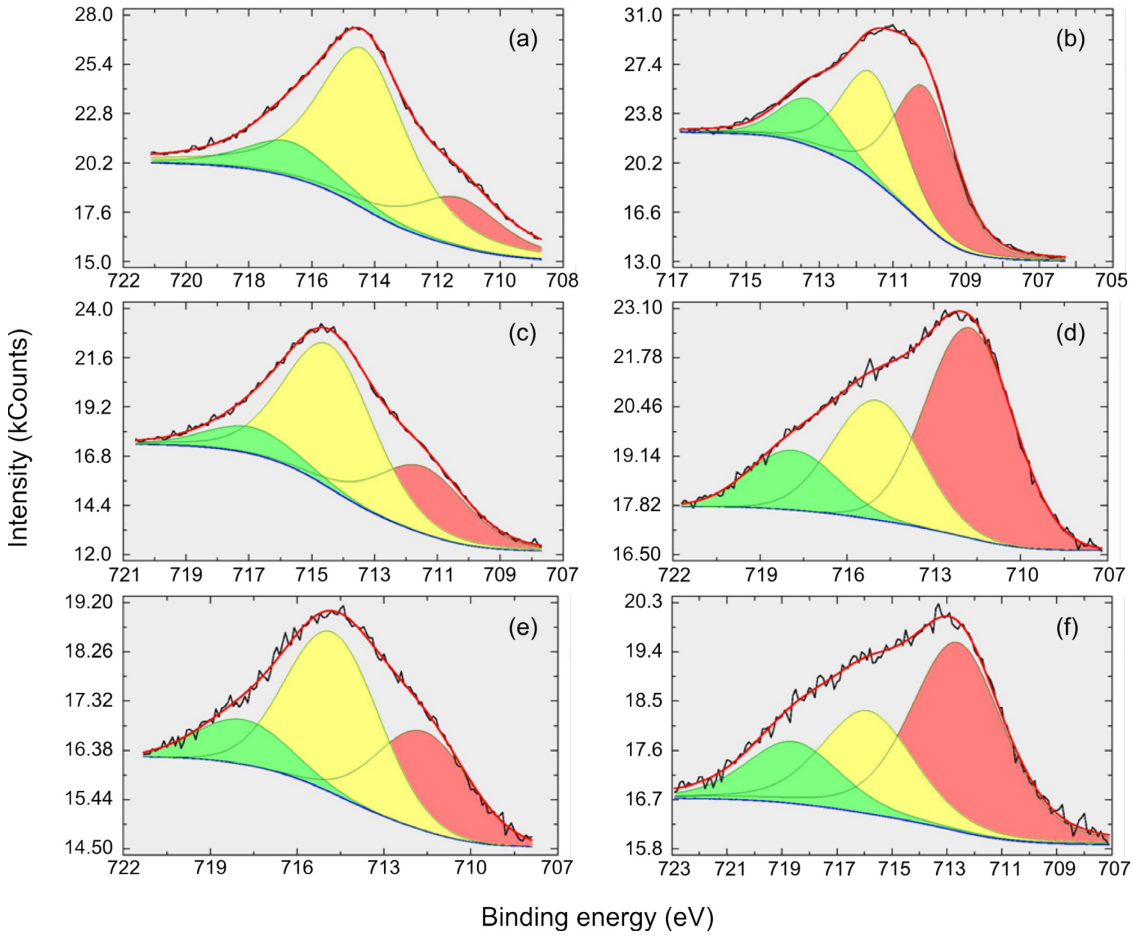

Fig. 5.6 Fe 2p emission of (a) crystalline FeF_3, (b) crystalline Fe_2O_3, (c) partially hydroxylated FeF_3, (d) one-step sol-gel prepared FeF_3-MgF_2 (fm-2), (e) mechano-milled FeF_3-MgF_2 (Mech-fm-2), and (f) xerogel of mixed FeF_3 and MgF_2 sols (Mix-fm-2); each colour represents a resolved BE value.

In this work, XPS was applied to clarify the following issues:

(1) the chemical state of Fe;

(2) the effect of dispersing FeF_3 into MgF_2 matrix on the BEs of Fe and Mg;

(3) the chemical composition of ternary FeF_3-MgF_2.

Here the discussion focuses on the results of four relevant elements, Fe, Mg, F, and O. The assignments of the fitted BEs are listed in Table 5.4. Three sets of BE values of Fe $2p_{3/2}$ photoelectrons are distinguished from the spectra. The BE at about 717-718 eV is assigned to the satellite peak; the BE of about 715 eV corresponds to Fe(III)-F; the BE of about 712 eV, however, may refer to either Fe(III)-O or Fe(II)-F species. As indicated by Mössbauer spectra, all the Fe atoms are in their +3 oxidation state; therefore the peak at the BE of 712 eV should be assigned to Fe(III)-O. For brevity, the oxidation state of Fe was omitted since it is always +3. The detailed Fe ($2p_{3/2}$) spectra of partially hydroxylated FeF_3 and Mech-fm-2 assemble the features of crystalline FeF_3 (Fig. 5.6 (a), (c), and (e)). The proportion of Fe-O is lower in the crystalline FeF_3 than that in the other two samples, as indicated by the peak between 710-713 eV. It is probably a consequence of the pre-dehydration of iron nitrate precursor, because the Fe-O bindings have been introduced into the samples through this process. In comparison, the fitted BE curves fm-2 and Mix-fm-2 samples show a different form. The dominant species is Fe-O instead of Fe-F in these samples. Since the Fe-O bindings indicate for Fe-OH species that are potential Brønsted acid sites, this result may explain the much higher activity of fm-2 and Mix-fm-2 comparing with Mech-fm-2 (see Table 5.3).

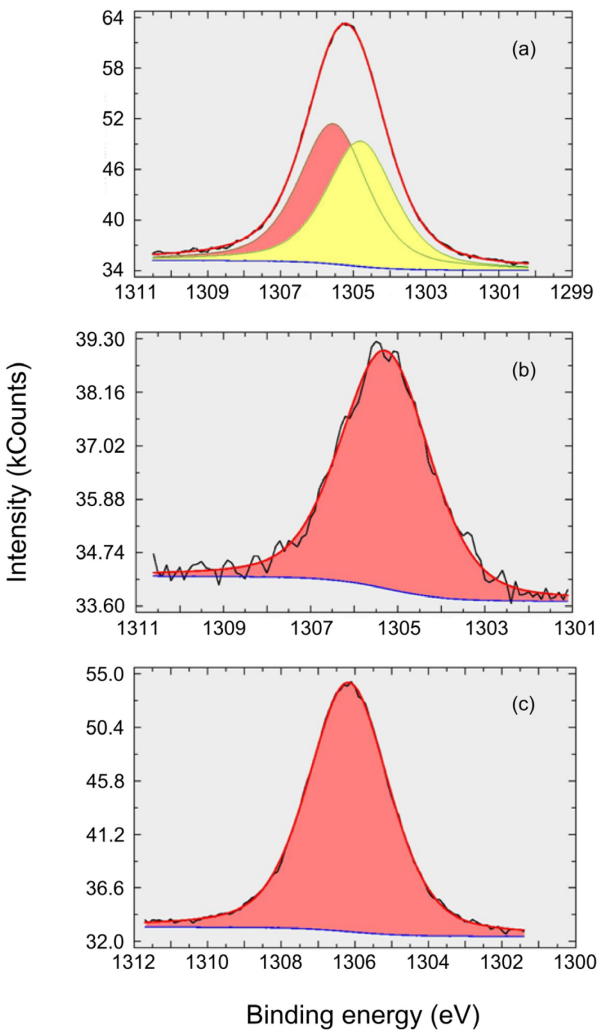

Fig. 5.7 Mg 1s emission of (a) fm-2, (b) mechano-milled FeF_3-MgF_2 (Mech-fm-2), and (c) xerogel of mixed FeF_3 and MgF_2 sols (Mix-fm-2); each colour represents a resolved BE value.

The BEs of Mg were examined by referring to the fitted Mg (1s) spectra (Fig. 5.7). In spite of their different synthesis routes, all the three studied FeF_3-MgF_2 samples show similar BEs of Mg 1s electrons that lie between 1305-1306 eV. Two peaks with different central BEs were resolved in the fm-2 spectrum (Fig. 5.7 (a)), both indicating Mg-F bonds in MgF_2. The increase of electron shielding in a Fe-F-Mg bonding probably contributes to the shift of one peak to lower BE (1304.8 eV). It confirms the interaction between Fe and Mg ions at the atomic level, as suggested by Mössbauer spectra (Fig. 5.5).

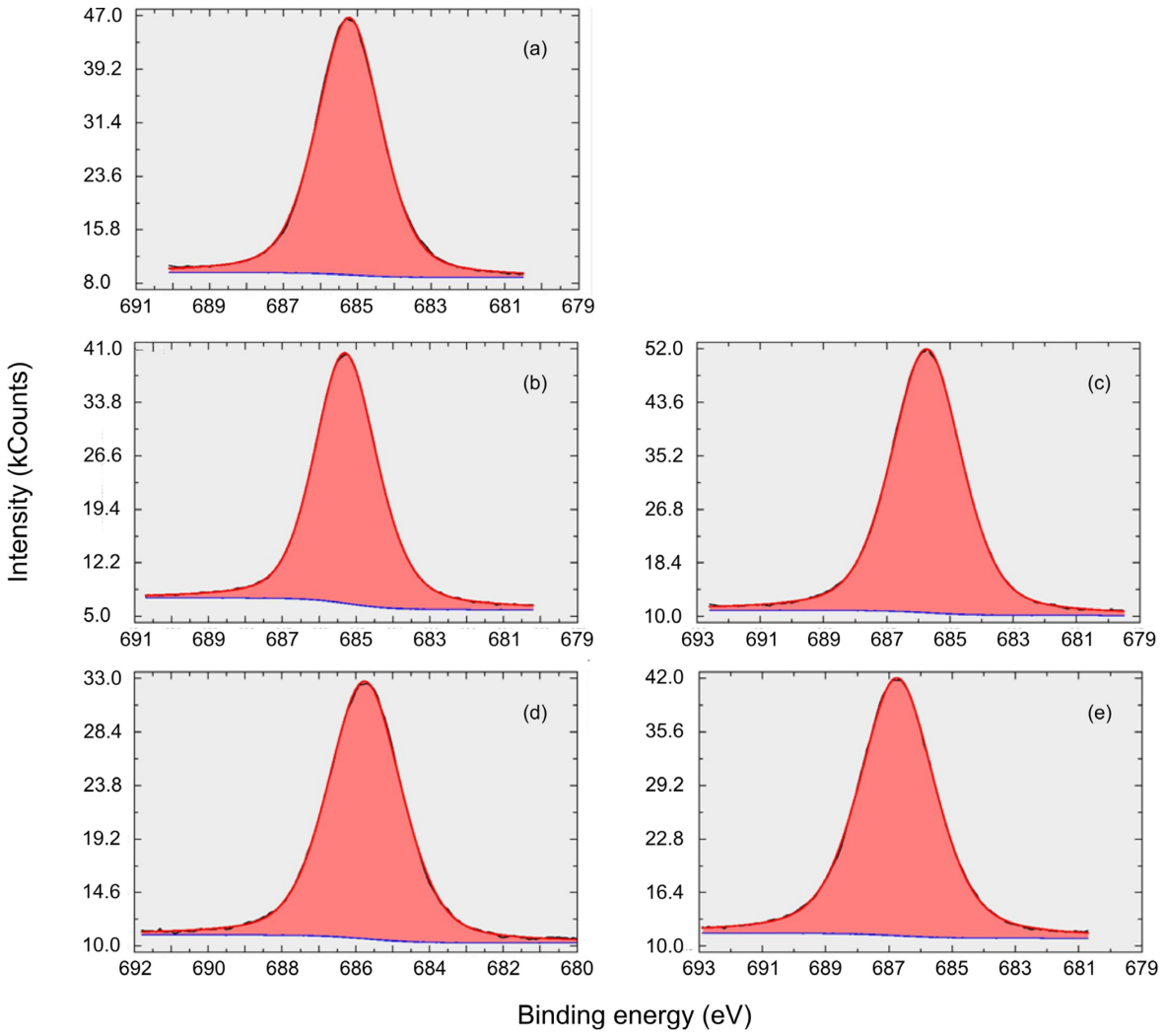

Fig. 5.8 F 1s emission of (a) crystalline FeF_3, (b) partially hydroxylated FeF_3, (c) fm-2, (d) mechano-milled FeF_3-MgF_2 (Mech-fm-2), and (e) xerogel of mixed FeF_3 and MgF_2 sols (Mix-fm-2).

Fig. 5.8 shows the detailed F (1s) spectra of FeF_3 and FeF_3-MgF_2 samples. Only one F-bonding species was observed in the XP spectra of all the samples. The BEs of F 1s photoelectrons of three FeF_3-MgF_2 samples (fm-2, Mech-fm-2, and Mix-fm-2) all shift slightly to higher region compared with that of crystalline FeF_3 or partially

hydroxylated FeF_3. It is probably due to the more electronegative Mg core, as the shielding effect of valence electrons on the F core is less effective.

Fig. 5.9 shows the fitted O (1s) spectra. Generally, three O-binding species can be interpreted from the BEs of O 1s electrons: the Fe-O bondings, organic species (probably residual acetate), and H_2O. Comparing the spectra of ternary FeF_3-MgF_2 and FeF_3, no significant differences can be observed. Thus using MgF_2 as matrix results in little disturbance in the coordination environment of O atoms.

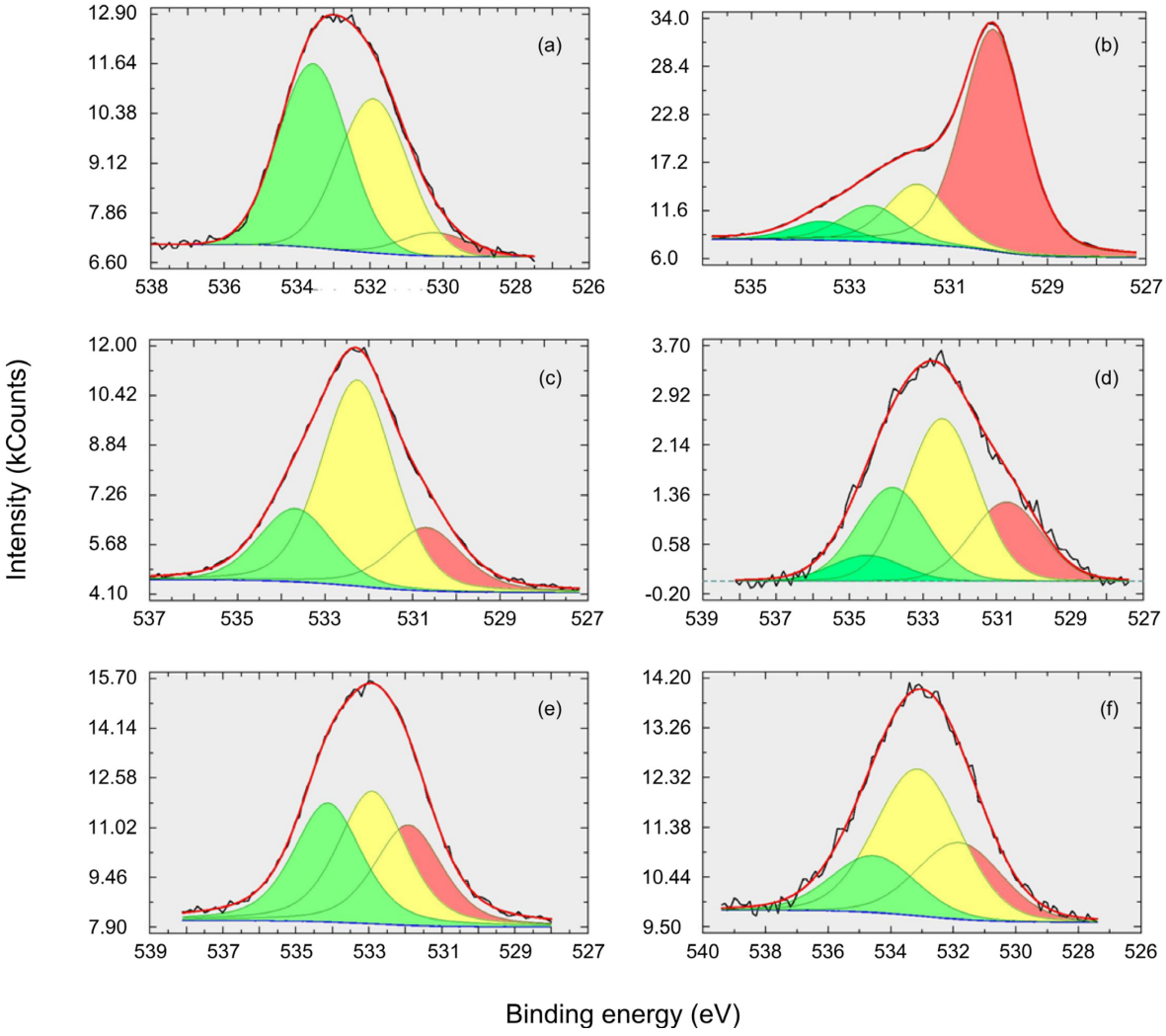

Fig. 5.9 O 1s emission of (a) crystalline FeF_3, (b) crystalline Fe_2O_3, (c) partially dehydrated FeF_3, (d) fm-2, (e) mechano-milled FeF_3-MgF_2 (Mech-fm-2), and (f) xerogel of mixed FeF_3 and MgF_2 sols (Mix-fm-2); each colour represents a resolved BE value.

Not only the BEs of different atoms but also the elemental composition can be determined by XPS. Especially, this technique can offer valuable information about the surface composition of the samples. The information

depth ($3\lambda_i$) for XPS can be calculated from the inelastic mean free path (IMFP), λ_i, of an electron in a solid. The IMFP for Fe 2p, Mg 1s, and F 1s emissions were 1.8, 2.9, and 1.8 nm, respectively;[53] for Al Kα excitation thus the corresponding information depths were 5.4, 8.7, and 5.4 nm each. The particle size of partially hydroxylated FeF_3 can be estimated from its TEM images (Fig. 4.5). Accepting the assumption that the sample consists of spherical particles, the particle radius is therefore about 5 nm. The estimated particle radius of the ternary FeF_3-MgF_2 sample, fm-2, is even smaller, of about 2 nm (Fig. 5.13). Thus XPS cannot differentiate between electron emissions of the surface atoms and of the bulk – it becomes a bulk method. Indeed, the F-to-Fe ratio of the partially hydroxylated FeF_3 obtained by XPS (2.8, Table 5.4) is comparable to that calculated from elemental analysis (2.7, Table 4.2). The Mg-to-Fe ratio of fm-2 is slightly higher than that of the precursors, probably because of the contribution of Mg atoms from the bulk.

In short, the different synthesis routes of FeF_3-MgF_2 samples and the XPS investigations confirm the disturbance of MgF_2 on FeF_3, and suggest that this interaction must be introduced via the interaction between sol particles *in situ* during the one-step sol-gel synthesis. This conclusion is in line with the deduction from Mössbauer spectra.

Table 5.4 Core-level binding energies (BEs) and calculated elemental compositions obtained from the fitted XPS data.

Sample	Fe 2p		Mg 1s		F 1s		O 1s		Elemental composition (atomic ratios)
	BE (eV)	Species	BE (eV)	Species	BE (eV)	Species	BE (eV)	Species	
Fm-2	711.8	Fe-O	1304.8	MgF_2	685.7	FeF_3 and	530.7	Fe-O	Fe/Mg/F/O =
	715.0	FeF_3	1305.6	MgF_2		MgF_2	532.5	Org.[b]	1/3.3/8.9/2.3
	717.9	Sat. FeF_3[a]					533.8	H_2O/org.	
							534.5	H_2O	
Mech-fm-2	711.6	Fe-O	1305.3	MgF_2	685.8	FeF_3 and	531.9	Fe-O	Fe/Mg/F/O =
	714.8	FeF_3				MgF_2	532.9	Org.	1/0.9/5.1/4.5
	717.9	Sat. FeF_3					534.1	H_2O	
Mix-fm-2	712.6	Fe-O	1306.2	MgF_2	686.7	FeF_3 and	531.8	Fe-O	Fe/Mg/F/O =
	715.9	FeF_3				MgF_2	533.1	Org.	1/2.8/6.8/2.4
	718.6	Sat. FeF_3					534.5	H_2O	
FeF_3	711.5	Fe-O			685.3	FeF_3	530.7	Fe-O	Fe/F/O =
	714.4	FeF_3					532.3	Org.	1/2.8/1.4
	716.9	Sat. FeF_3					533.7	H_2O/org.	

a: Satellite peak; b: organic species.

5.2.2.2 *Discussion: formation of ternary FeF_3-MgF_2*

The discussion in 5.2.2.1 describes the interaction between FeF_3 and MgF_2 in the ternary fluorides materials. The interaction between sol particles seems to have a great influence on the final xerogel products. Naturally, the question of how the ternary fluorides sol is formed needs to be discussed. It is therefore essential to examine the reaction pathway in the synthesis of ternary FeF_3-MgF_2. To this end, a two-step fluorination process was designed by using iron and magnesium precursors in revised orders: that is, an FeF_3 (or MgF_2) sol was first prepared following the usual procedure, then the magnesium acetate (or iron nitrate) precursor was added, and finally the mixture was fluorinated stoichiometrically in the second step. When MgF_2 sol was first prepared, no unusual phenomenon was observed during the synthesis; and the final xerogel product was almost identical to the one-step fluorinated fm-*n* samples in both porous structure and catalytic activity. When FeF_3 sol was first prepared, however, an unexpected colour change was observed: the turbid $Mg(OAc)_2$ suspension was added to the colourless and transparent FeF_3 sol, and then these two obviously reacted and formed a red-brown solution (or sol), which became transparent as the stir bar was visible (Fig. 5.10 (h)).

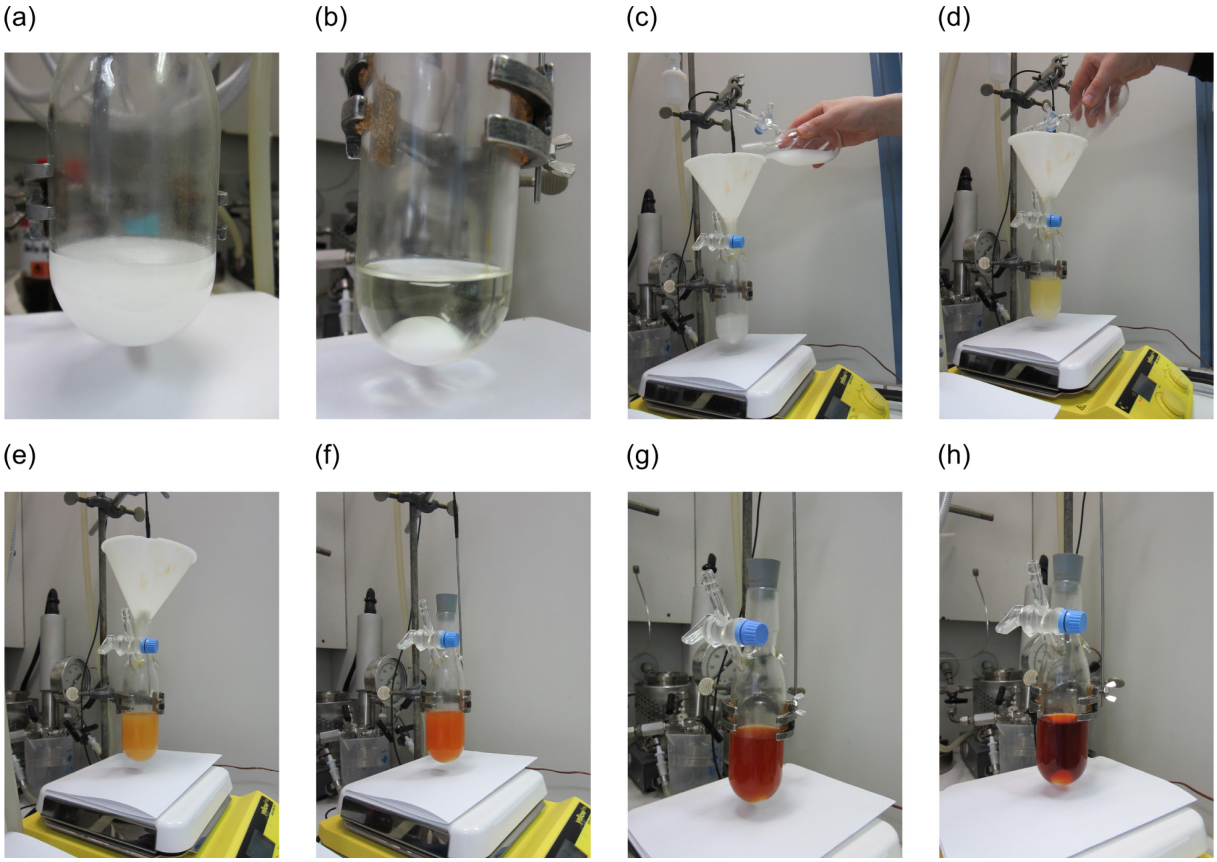

Fig. 5.10 Images of (a) $Mg(OAc)_2$ suspension, (b) FeF_3 sol, (c) adding $Mg(OAc)_2$ suspension to FeF_3 sol; and image records of $Mg(OAc)_2$-FeF_3 (Mg-to-Fe ratio 1.5) mixture at (d) t = 0 min, (e) t = 1 min, (f) t = 2 min, (g) t = 5 min, and (h) t = 14 min.

Since iron nitrate and magnesium acetate were used as precursors, the partly fluorinated mixture in Fig. 5.10 (h) should contain compounds or complexes formed by five ionic species, Fe^{3+}, Mg^{2+}, F^-, NO_3^-, and OAc^-, in methanolic solution. It is known that MgF_2, $Mg(NO_3)_2$, and $Mg(OAc)_2$ are all white in colour, while iron nitrate and iron acetate can form complexes showing a typical red-brown colour.[19] Moreover, it is also known that Fe^{3+} shows great affinity towards oxygen-containing ligands like acetate.[19, 54] Thus it is possible that a metathesis reaction happens between FeF_3 and $Mg(OAc)_2$ in the sol and gives rise to an intermediate iron acetate complex. This deduction implies that magnesium is the first to be fluorinated in the competition with iron during fluorination. A possible two-step reaction pathway is therefore proposed in Fig. 5.11.

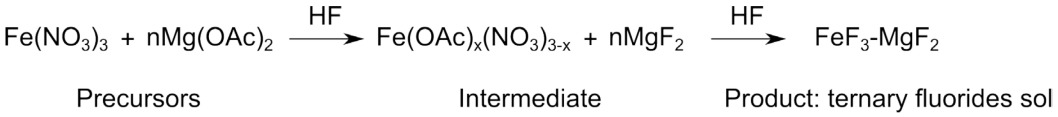

Fig. 5.11 Possible reaction pathway of ternary FeF_3-MgF_2.

To analyse the composition of the intermediate mixture, the solution (or sol) shown in Fig. 5.10 (h) was carefully dried at 30°C to avoid decomposition of iron complexes. The obtained brick-red powder was studied by elemental analysis. The calculated composition is presented in Table 5.5. Not only acetate but also nitrate was found in the iron complex.

Table 5.5 Elemental analysis of the intermediate.

Mg-to-Fe ratio	Element (wt%)				Calculated composition
	C [a]	H [a]	N [a]	F [b]	
1.5	7.4	2.4	6.2	16.1	$Fe(OAc)_{1.3}(NO_3)_{1.7}\cdot 1.5MgF_2\cdot 2H_2O$

a: Error range: ± 0.3%; b: error range: ± 2.0%.

Finally, another synthesis was designed to examine the hypothesis about the formation pathway of FeF_3-MgF_2 sol. In this synthesis, mixed iron and magnesium precursors were fluorinated with understoichiometric amounts of HF; the amount of HF was controlled as in two equivalents to Mg. The obtained powder product was calcined, and studied by XRD (Fig. 5.12). The reflexes are assigned to two phases, Fe_2O_3 and MgF_2. The Fe_2O_3 phase is probably the calcination product of the intermediate $Fe(OAc)_x(NO_3)_x$. No evidences of FeF_3 or MgO can be observed. In short, only one fluoride phase, MgF_2, is identified in this sample. This suggests that the proposed reaction pathway in Fig. 5.11 is likely to be the case.

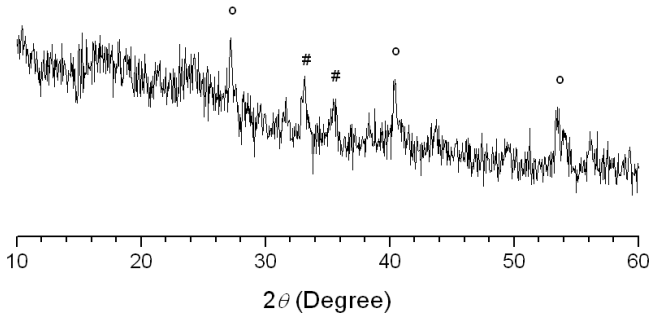

Fig. 5.12 Powder XRD pattern of an understoichiometrically fluorinated Fe-Mg sample after calcined at 600°C (# refers to an Fe_2O_3 phase in PDF 33-664 and ° indicates a MgF_2 phase in PDF 1-1196).

5.2.3 Morphology

The ternary FeF_3-MgF_2 was further investigated by electron microscopy. Nanocrystallites with clear crystalline planes can be distinguished in the HRTEM image of fm-2 (Fig. 5.13 (A)). Assuming FeF_3-MgF_2 consists of spherical crystallites, the radii of these particles are mostly below 2 nm, which is significantly smaller than that of FeF_3 (Fig. 4.5 (A)).

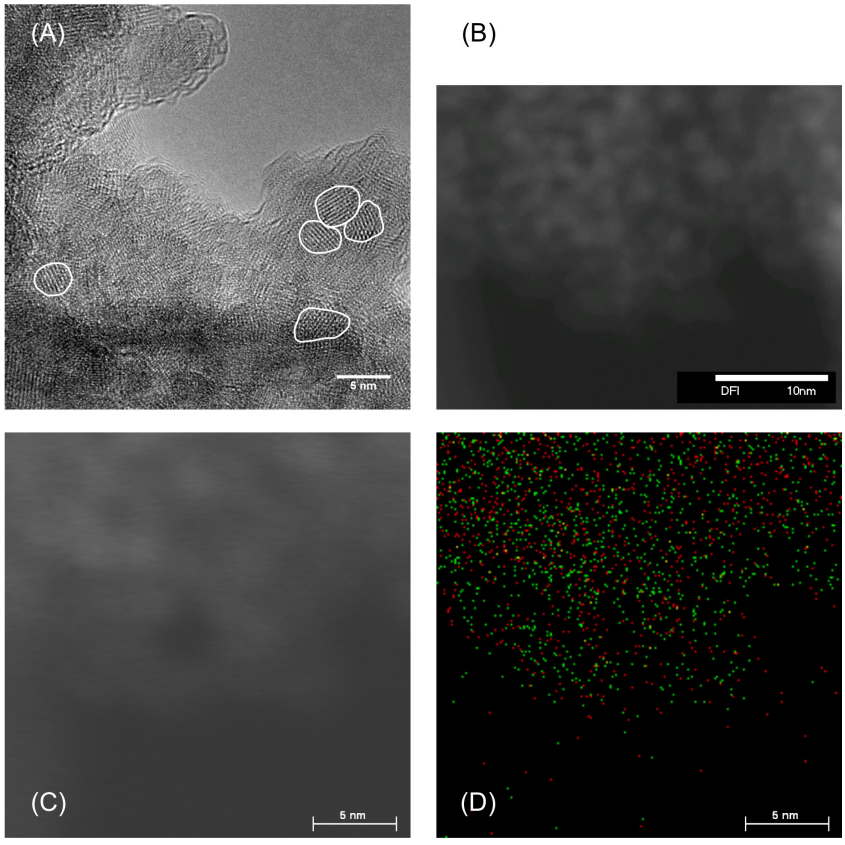

Fig. 5.13 (A) HRTEM image (scale: 5 nm) of fm-2; (B) STEM image (scale: 10 nm) of fm-2; (C) STEM image (scale: 5 nm) of fm-2; (D) the hypermap of Fe and Mg elements (red: Fe; green: Mg) corresponding to (C).

The STEM image suggests that the voids between aggregates or agglomerates form the porous system of fm-2 (the dark regions in Fig. 5.13 (B)). Different to FeF_3, FeF_3-MgF_2 exhibits distinctly smaller pores: only micropores or small mesopores that are smaller than 5 nm are observed (Fig. 5.13 (B)). The N_2 adsorption-desorption measurements in 5.3.1 offer further investigations on this issue.

Moreover, with STEM, it is possible to perform mapping by energy dispersive X-ray spectroscopy (EDX); thus the elemental distribution in FeF_3-MgF_2 particles can be determined. This technique may offer valuable information in clarifying the material's structure. Distribution of Fe and Mg elements in the selected area (corresponding to STEM image in Fig. 5.13 (C)) were calculated from the hypermap (Fig. 5.13 (D)) generated by EDX. Interestingly, Fe and Mg show a homogeneous distribution; this result gives rise to two possible interpretations: Fe and Mg distribute homogeneously in two dimensions, corresponding to a layer structure, or they disperse uniformly in three dimensions, referring to a granular structure. Since no evidences show that FeF_3-MgF_2 samples consists of layered structure, it can be deduced that the two elements distribute homogeneously in 3-dimensional space and therefore there are no isolated FeF_3-domains embedded in MgF_2 matrix.

5.3 Surface characterisation

5.3.1 Surface area and porosity

In the ternary FeF_3-MgF_2 system, a nanoscopic MgF_2 (surface area: 240-260 $m^2 \cdot g^{-1}$) was used as matrix to tune the surface area of the material. To determine the surface area and porosity of the FeF_3-MgF_2 samples, N_2 adsorption-desorption measurements were performed. The summarised isotherms in Fig. 5.14 (A) provide an overview of the porous features of the fm-*n* samples. With increasing content of MgF_2, the isotherm changes gradually from an "FeF_3-type" (Fig. 5.14 (A): (a)) to a "MgF_2-type" (Fig. 5.14 (A): (d)). As described in Chapter 4, the "FeF_3-type" isotherm corresponds to meso-/microporous materials exhibiting nonuniform pores. Showing a type H2 hysteresis loop, the "MgF_2-type" isotherm is indicative for micro-/mesoporous materials with nearly cylindrical pores of nonuniform size.[39]

In the next step the B.E.T. surface area and average pore diameter, both calculated from the isotherms, were plotted versus the molar Mg-to-Fe ratio, respectively. (Fig. 5.14 (B)) The surface area increases drastically with Mg content until it approaches the maximum at the Mg-to-Fe ratio of 2 to 1. Afterwards higher Mg contents do not result in further increases: the fm-2 sample exhibits the highest surface area of 380-500 $m^2 \cdot g^{-1}$. Unexpectedly, the surface areas of most fm-*n* samples are even higher than that of the pure MgF_2. As discussed in 5.2.2, this is probably caused by structural distortions of FeF_3 in presence of MgF_2. Additionally, the use of iron nitrate precursor leads to some residual $-NO_3$ groups. These residual nitrates may catalyse the decomposition of other organic residuals and thus give rise to gas species that contribute to higher surface.

Moreover, not only the surface area but also the pore size was tuned in the ternary FeF_3-MgF_2. The average pore diameters of fm-*n* samples show a logarithmic relationship to the Mg-to-Fe ratio (Fig. 5.14 (C)). The pore diameter of the fm-*n* ($n \geq 2$) samples lies in the range of 2-3 nm, which is at the borderline between micro- and mesoporosity. The result is also in line with the STEM image of fm-2 in Fig. 5.13.

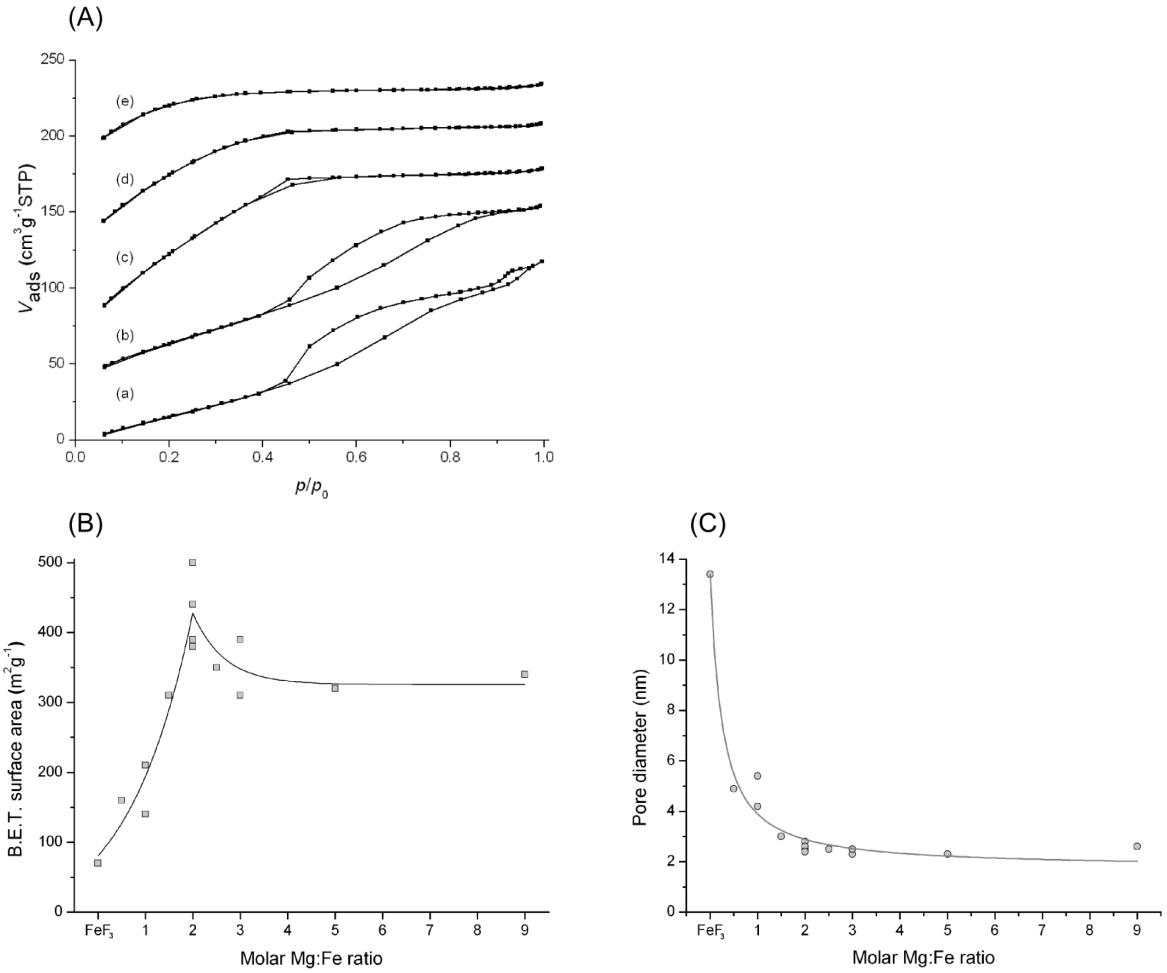

Fig. 5.14 (A) N_2 adsorption-desorption isotherms of (a) fm-0.5, (b) fm-1, (c) fm-2, (d) fm-3, and (e) MgF_2; (B) surface area of fm-*n* samples versus the molar Mg-to-Fe ratio; (C) pore diameter of fm-*n* samples versus the molar Mg-to-Fe ratio. Results of FeF_3 and MgF_2 are provided as references. Some fm-*n* samples were synthesised repeatedly to examine the reproducibility.

5.3.2 Surface acidity

A study on the surface acidity of FeF_3-MgF_2 is crucial because it suggests their potentials as solid acid catalysts. Therefore, ammonia (NH_3) and deuterated acetonitrile (CD_3CN) were employed as probe molecules. Temperature programmed desorption (TPD) and chemisorption-IR were used as complementary methods to investigate the interaction between the probe molecules and the sample surface.

To determine the strengths of the surface acid sites, TPD measurements were performed using NH_3 as probe molecule. The NH_3-TPD profile of the fm-2 sample is shown in Fig. 5.15. The records of FeF_3 and MgF_2 are also presented as references. The profile of FeF_3 has one maximum at 300°C, referring to medium strong acid sites.[8] In the profile of MgF_2, however, the maximum at 160°C is characteristic for weak acid sites. More interestingly,

with two maxima at 160 and 280°C evidencing the presence of both weak and medium strong acid sites, the fm-2 sample shows hybridised features of the desorption profiles of FeF_3 and MgF_2.

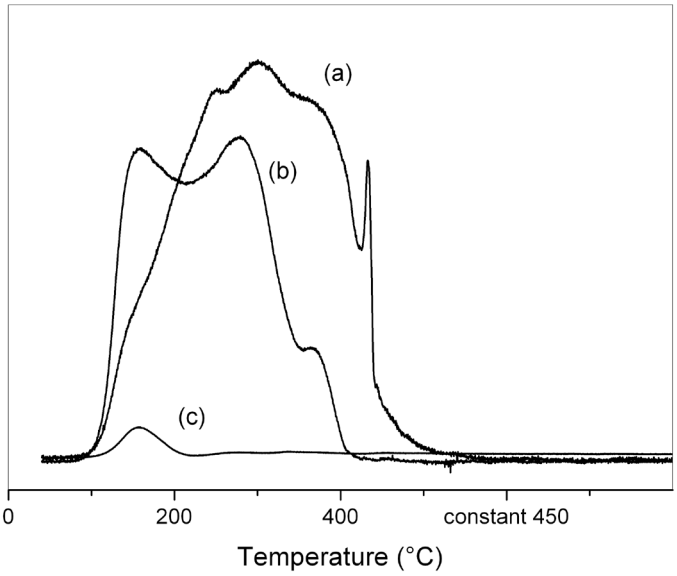

Fig. 5.15 NH_3-TPD profiles of (a) FeF_3, (b) fm-2, and (c) MgF_2.

The TPD method is very useful in investigating the strength of acid sites. However it is not specific for Lewis or Brønsted acid sites. Therefore, chemisorption-IR spectra with NH_3 as probe molecule were recorded. The differential spectra of one FeF_3-MgF_2 sample, fm-2, are given in Fig. 5.16 (A). Other samples exhibit similar behaviour; thus although the following discussion relates to one representative sample, fm-2, it holds for other fm-*n* samples as well. The chemisorption models of NH_3 on solid surface have been discussed in 4.3.2. Accordingly, the intense band at 1436 cm^{-1} is assigned to protonated ammonium (NH_4^+) species stabilised by adjacent –OH groups,[55] confirming the existence of Brønsted acid sites on the fm-2 surface. This band lies at almost the same position as that in the spectra of FeF_3 (Fig. 4.7), suggesting the strength of the strong Brønsted sites is similar in two samples.

The assignments of the other three vibration bands are not straightforward. The 1191 and 1243 cm^{-1} bands lie in the wavenumber range (1280-1150 cm^{-1})[44] of the vibration bands of coordinated NH_3 species at Lewis acid sites. The band at 1303 cm^{-1}, however, can be only assigned to coordinated NH_3 species with strong hydrogen bonding (Fig. 5.16 (B)).[33, 44] Yet it is noticeable that the reference is based on the study of $[M(NH_3)_m]\cdot Hal_n$ coordination compounds while the results here are based on solid surfaces. The H-bonding species referring to weak Brønsted acidity were not detected on the surface of fm-2.

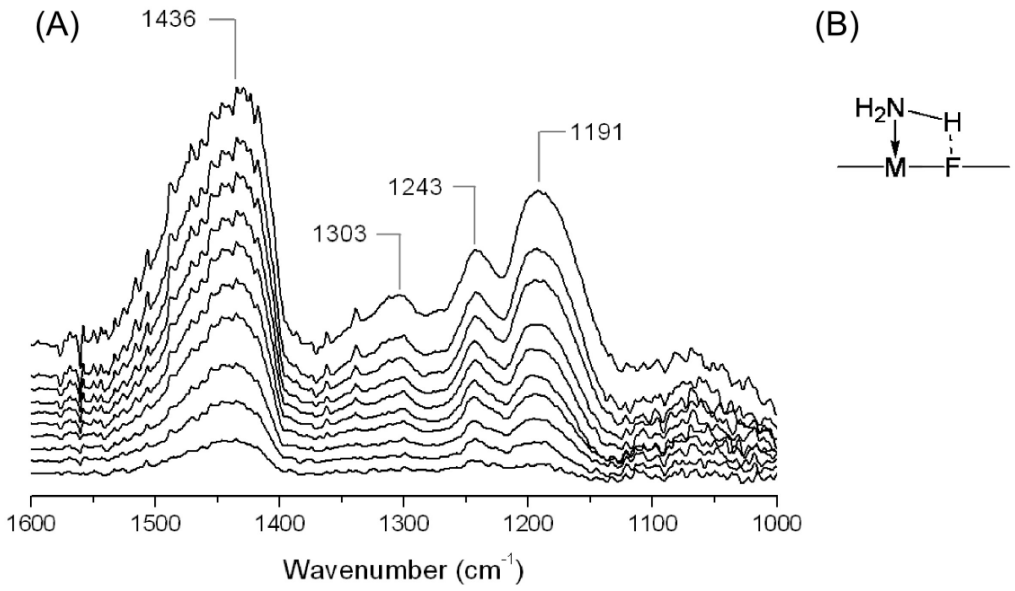

Fig. 5.16 (A) Differential IR spectra of fm-2 saturated stepwise with NH_3; (B) schematic diagram of NH_3 co-ordinated to a Lewis acid site with H-bonding to fluorine.

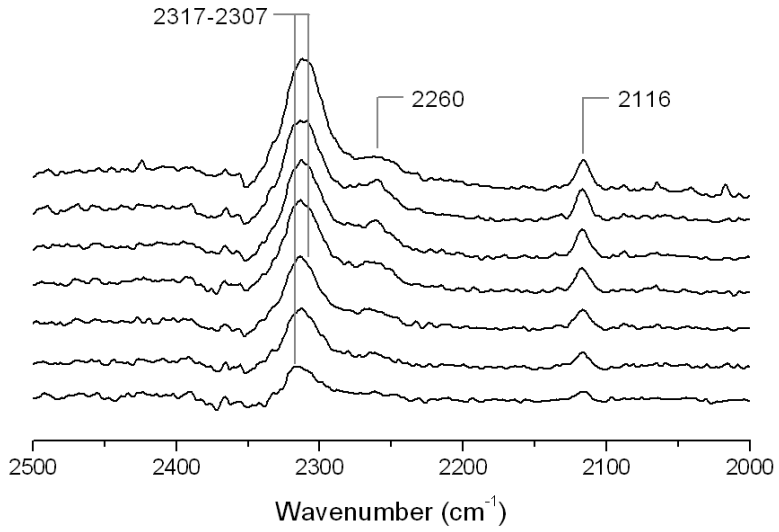

Fig. 5.17 Differential IR spectra of fm-2 saturated stepwise with CD_3CN.

CD_3CN was also employed as probe molecules to study the fm-*n* samples. In the differential spectra of fm-2 (Fig. 5.17), the trio bands at 2890, 2400, and 1700 cm^{-1} are still missing. Thus the fm-2 surface does exhibit strong Brønsted sites that can form H-complexes with CD_3CN. The band at 2116 cm^{-1} corresponds to the sym-

metric CD_3 stretching. The asymmetric modes of the CD_3 stretching vibration is too weak to be detected. The band at 2260 cm^{-1} results from physisorbed species. The 2314 cm^{-1} band is characteristic for coordinated CD_3CN species on medium strong and strong Lewis acid sites. Its frequency shifts slightly to the lower wavenumber range (4 cm^{-1}) as compared with that in the spectra of FeF_3 (Fig. 4.8) This implies that the Lewis acidity of FeF_3-MgF_2 is probably slightly weaker than that of FeF_3.

In conclusion, both Lewis and Brønsted acid sites co-exist on the surface of the ternary FeF_3-MgF_2 samples. The chemisorption-IR spectra of FeF_3 (Fig. 4.7 and Fig. 4.8) are similar to those of the FeF_3-MgF_2 samples, whereas the spectra of MgF_2 give only evidences of weak Lewis acid sites. Thus FeF_3 has a decisive influence on the surface acidic properties of the FeF_3-MgF_2 samples.

5.4 Summary

In this chapter, the synthesis route of ternary FeF_3-MgF_2 materials was established. The partially hydroxylated FeF_3 described in Chapter 4 was dispersed in a high-surface MgF_2 matrix through a simple one-step fluorination. Characterisation of the ternary FeF_3-MgF_2 material revealed its physicochemical properties. Structural studies indicated that in the ternary FeF_3-MgF_2 samples, the coordination environment around iron atoms is disturbed due to the incorporation into the MgF_2 matrix. N_2 adsorption-desorption isotherms suggested that FeF_3-MgF_2 exhibits extraordinarily high surface area (up to 500 $m^2 \cdot g^{-1}$) and micro-/mesoporosity. Since surface acidity has a direct impact on the material's catalytic activity, it was studied by employing complementary characterisation methods with different probe molecules. Weak and medium strong surface acid sites were detected on the FeF_3-MgF_2 samples. More importantly, strong Lewis and medium strong Brønsted acid sites were identified predominant on the FeF_3-MgF_2 surface. A novel ternary fluorides material with high surface and bi-acidity has been successfully produced via a convenient synthesis route.

6 Synthesis and characterisation of ternary FeF_3-MF_2 (M = Ca, Sr, or Zn)

Encouraged by the extraordinary surface properties of FeF_3-MgF_2 materials, other alkaline earth metal fluorides like calcium fluoride (CaF_2) and strontium fluoride (SrF_2) were used as matrices to prepare more ternary fluoride materials. Zinc fluoride (ZnF_2) was also employed due to its similarity to MgF_2 in many aspects including electron configuration, coordination number and ionic radius.[47] This chapter summarises the synthesis strategy and the characterisation results of these ternary FeF_3-MF_2 materials. It was found that not only surface area and pore size but also surface acidity can be tuned by changing the MF_2 matrix or the M-to-Fe ratio or both. This study therefore opens new possibilities in preparing materials with tunable surface properties.

6.1 Synthesis

The synthesis of ternary FeF_3-MF_2 (M = Ca, Sr, or Zn) follows the same route as that was applied to synthesise FeF_3-MgF_2. Pre-dehydrated iron nitrate was mixed with the respective metal acetate and then suspended in methanol. The precursor suspension was fluorinated with stoichiometric amounts of HF in a single step. Since the synthesis strategy allows easy adjustment of the molar M-to-Fe ratio, screening of the FeF_3-MF_2 catalysts has been achieved in two dimensions by changing the M metal or the M-to-Fe ratio. The obtained xerogels were named after their initials: fc-*n* for FeF_3-CaF_2, fs-*n* for FeF_3-SrF_2, and fz-*n* for FeF_3-ZnF_2; *n* refers to the molar M-to-Fe ratio.

Systematic changes were observed in the appearances of the obtained FeF_3-MF_2 sols. Images were recorded for the precursor suspensions and their corresponding sols after fluorination (Fig. 6.1 (B)). The FeF_3-CaF_2 sol is slightly turbid, while the FeF_3-SrF_2 "sol" is completely turbid and therefore should be identified as a suspension. In contrast to these two samples, the FeF_3-ZnF_2 sol is transparent. Its transparency is the same as that of the FeF_3-MgF_2 sol (see Fig. 5.1). The reason is probably the similarity between MgF_2 and ZnF_2. Since Zn has a fully occupied d-shell, it has the same electron configuration as Mg. The two elements have almost identical coordination number and ionic radius,[47] and their fluorides have the same rutile structure. Moreover, previous studies on the sol-gel prepared ZnF_2 suggested that its surface area and acidity are comparable to that of sol-gel prepared MgF_2.[42]

Since the turbidity of sols usually indicates larger sol particles or higher proportion of large sol particles, one can roughly estimate the average sol particle size of different samples as: FeF_3-SrF_2 > FeF_3-CaF_2 > FeF_3-ZnF_2. As the sol particle size is indicative for agglomeration or aggregation degree, which may influence the porous structure of the corresponding xerogel, the ternary FeF_3-MF_2 materials may exhibit systematic changes in porosity. On the other hand, changing the M-to-Fe ratio was found having little influence on the transparency of the sol. Thus it can be deduced that the MF_2 matrix has a crucial impact on the sol particle size of the ternary FeF_3-MF_2.

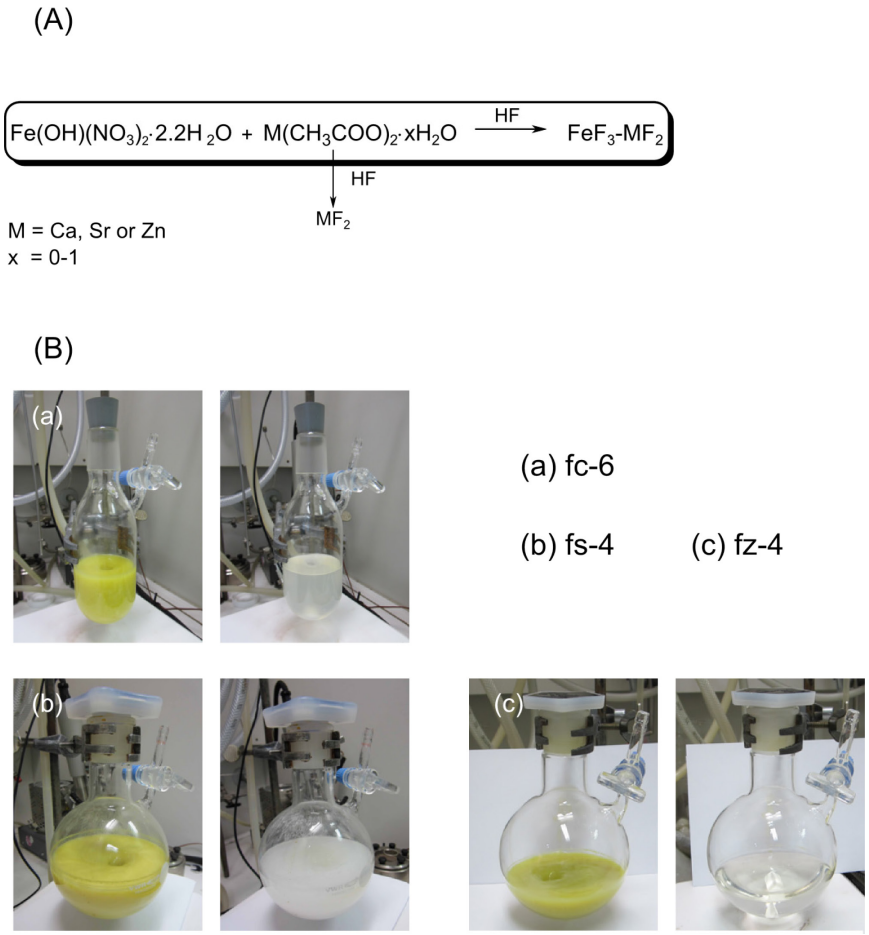

Fig. 6.1 (A) Schematic diagram of the one-step synthesis of ternary FeF_3-MF_2 (M = Ca, Sr, or Zn); (B) images of mixed Fe-M precursors suspensions (left) and the corresponding sols (right) of (a) fc-6, (b)fs-4, and (c) fz-4.

6.2 Bulk characterisation

6.2.1 Chemical composition

6.2.1.1 Thermal analysis

The dried FeF_3-MF_2 xerogels were first studied with thermal analysis. The TG curves and MS profiles of three representative samples are shown in Fig. 6.2. Weight loss of the FeF_3-CaF_2 is mainly caused by release of H_2O^+ (m/z = 18), which may come from coordinated water or hydroxyls. Decomposition products of residual nitrate and acetate (NO^+, CO_2^+, and CH_3^+; m/z = 30, 44, and 15) are also observed. The release of F^+ (m/z = 19) of FeF_3-CaF_2 happens after 250°C, which is similar to that of FeF_3-MgF_2; it implies that the two ternary fluorides show similar thermal stability. The TG curve of FeF_3-SrF_2 shows that it underwent a three-step decomposition: weight loss of the first step (100-290°C) corresponds to the release of water and hydroxyls, and of decomposition of some residual acetate; weight loss of the second step (300-460°C) mainly results from decomposition of residual nitrate and oxidation of organic residuals; weight loss of the last step is less significant, and is probably caused by release of some strongly bonded hydroxyls and decomposition of acetate. The TG curve of FeF_3-ZnF_2

also exhibits three decomposition steps. In the first step (120-300°C), the weight loss is due to the release of water and hydroxyls as well as the decomposition of nitrate. The second (300-420°C) and third (420-600°C) steps cannot be separated as clearly as in the TG curve of FeF_3-SrF_2; decomposition of acetate and release of strongly bonded hydroxyls contribute to the weight loss in both steps.

Comparing the MS profiles of FeF_3-CaF_2 and FeF_3-SrF_2, the largest difference lies on the decomposition temperature of nitrate, as indicated by the release of NO^+. The maximum of the ion current occurs at about 280°C in the profile of FeF_3-CaF_2, while it appears at 380°C in the profile of FeF_3-SrF_2 sample. More interestingly, by referring to the MS profile of FeF_3-MgF_2 (Fig. 5.2), it is clear that decomposition of the nitrate residuals becomes harder with the atom number of M metal. Different decomposition temperatures must be the consequence of different nitrate species. In other words, different nitrates remain as residuals in different FeF_3-MF_2 samples. It is straightforward to explain once the reaction path of the ternary fluorides is examined. In all the samples, iron nitrate salt was mixed with alkaline earth metal acetate in precursor suspensions. The metathesis between the two precursors is therefore unavoidable. Thus despite iron nitrate, alkaline earth metal nitrate may also exist in the precursor suspension. Since the thermal stability of $M(NO_3)_2$ increases with the atom number of M,[19] the release of the NO^+ occurs accordingly at different temperatures. The decomposition pathway of $M(NO_3)_2$ is shown in Eq. 6.1:

Eq. 6.1 $M(NO_3)_2 \rightarrow MO + 2NO_2 + 1/2O_2$,

$2NO_2 \rightarrow 2NO + O_2$.

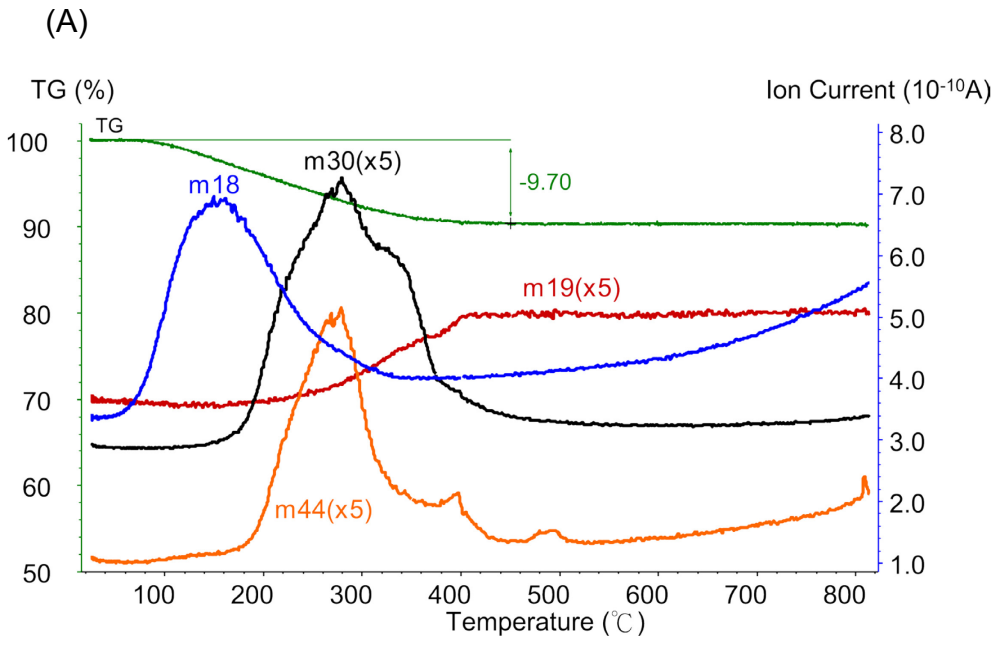

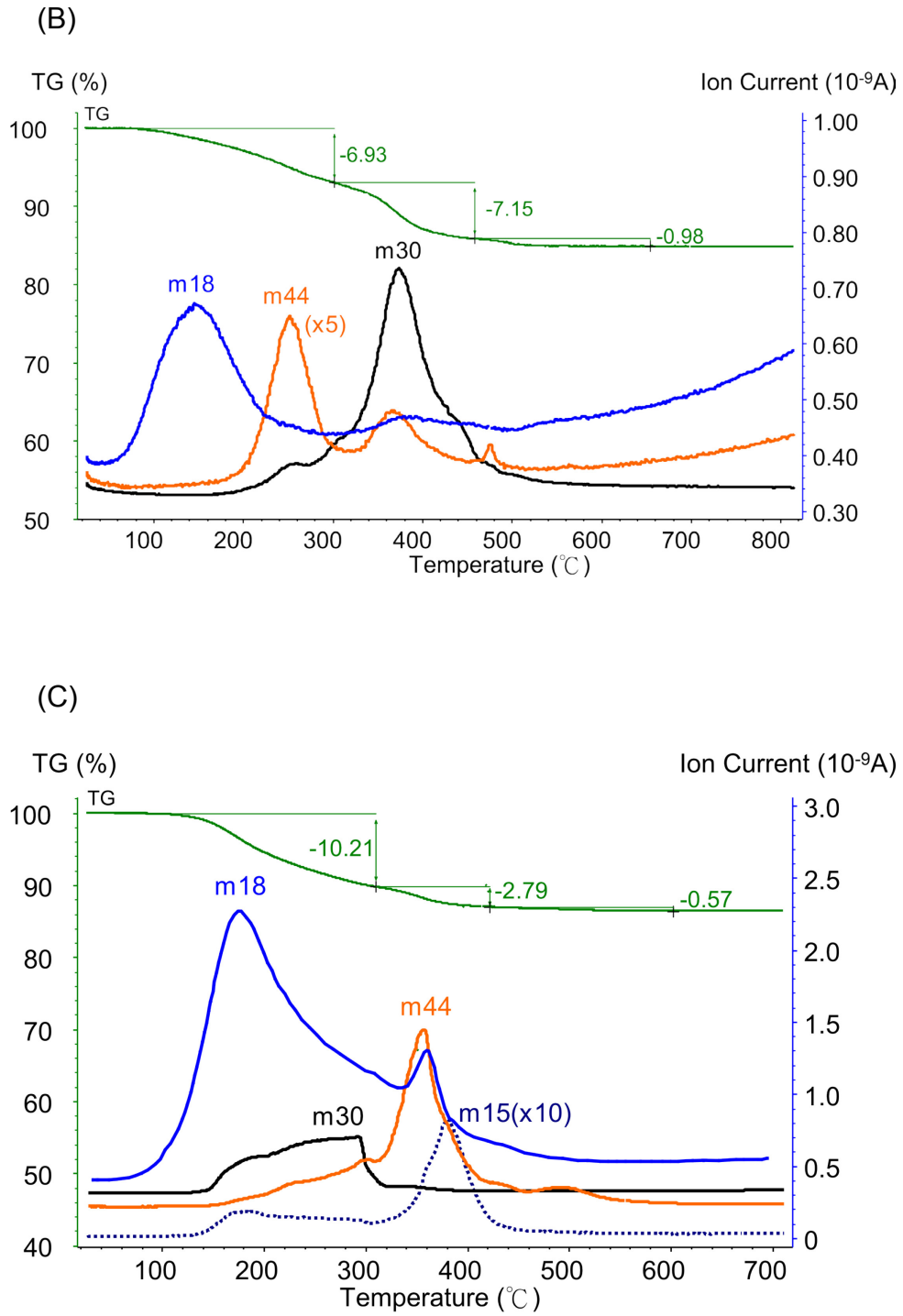

Fig. 6.2 TG curve and MS profiles of (A) fc-4, (B) fs-7, and (C) fz-7; assignments of the ionic fragments: m15 (CH_3^+), m18 (H_2O^+), m19 (F^+), m30 (NO^+), and m44 (CO_2^+).

6.2.1.2 Elemental analysis

Table 6.1 summarises the results of elemental analysis of the representative FeF_3-MF_2 samples. The results of the corresponding MF_2 are given as references. As elucidated by thermal analysis, the alkaline earth metal precursor

undergoes metathesis reaction with iron nitrate, hence leading to the formation of $M(NO_3)_2$. The Gibbs free energy of the fluorination of $Ca(NO_3)_2$ and $Sr(NO_3)_2$ with HF were calculated (Table 6.2).[47] Data of $Mg(NO_3)_2$ and $Ba(NO_3)_2$ were also provided for a better comparison. In the alkaline earth metal group, the tendency of forming metal fluoride over nitrate decreases with the atom number (Mg-to-Sr). This explains the significantly higher content of NO_3^- in FeF_3-SrF_2, because the formation of SrF_2 is less favoured. It also explains why Ba is excluded from this work: one experiment with Fe-Ba system shows that $Ba(NO_3)_2$, instead of BaF_2, was obtained as confirmed by the XRD pattern in Fig. 6.3. The fluorination degree of FeF_3-MF_2 samples is generally high and almost reaches the limit of the corresponding MF_2; this observation fits the result of FeF_3-MgF_2 samples. Similar to FeF_3-MgF_2, these ternary fluorides survived with most hydroxyl groups after fluorination; thus they can be applied as potential bi-acidic catalysts.

Table 6.1 Results of elemental analysis of FeF_3-MF_2 and MF_2 samples (M = Ca, Sr, or Zn).

Sample	Element (wt%)				Calculated composition	Fluorination degree [d]
	C [a]	H [a]	N [a]	F [b]		
fc-4	0.4	0.7	0.8	38.7	$FeCa_4F_{9.7}(OH)_{0.9}(NO_3)_{0.3}(Oac)_{0.1}\cdot 1.0H_2O$	0.88
CaF_2	4.1	1.2		34.7	$CaF_{1.8}(OAc)_{0.2}\cdot 0.8H_2O$	0.90
fs-7	0.1	1.0	1.7	22.5	$FeSr_7F_{14.7}(OH)_{0.8}(NO_3)_{1.4}(OAc)_{0.1}\cdot 5.3H_2O$	0.86
SrF_2	3.6	0.8		21.8	$SrF_{1.8}(OAc)_{0.2}\cdot 1.1H_2O$	0.90
fz-7	1.0	0.9	1.0	26.7	$FeZn_7F_{14.8}(OH)_{1.2}(NO_3)_{0.6}(OAc)_{0.4}\cdot 3.0H_2O$	0.87
ZnF_2	4.6	0.8		33.1	$ZnF_{1.8}(OAc)_{0.2}$	0.90

a: Error range: ± 0.3%; b: error range: ± 2.0%; c: below detection limit; d: fluorination degree: [F]/(3[Fe]+2[M]).

Table 6.2 Gibbs free energy: the reaction of metal nitrate with HF to metal fluoride and nitric acid.

	$\Delta_r G$ (kJ·mol^{-1})
$Mg(NO_3)_2$	-92.3
$Ca(NO_3)_2$	-43.4
$Sr(NO_3)_2$	4.6
$Ba(NO_3)_2$	25.2

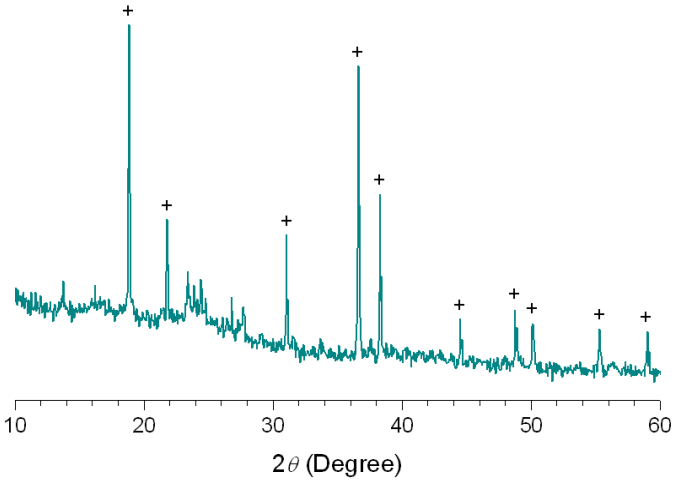

Fig. 6.3 The powder XRD pattern of an "FeF_3-BaF_2" sample; + refers to a $Ba(NO_3)_2$ phase in PDF 24-53.

6.2.2 Phase composition and morphology

The phase compositions of ternary FeF_3-MF_2 were studied by powder XRD. At low M-to-Fe ratios, FeF_3-CaF_2 and FeF_3-ZnF_2 are amorphous and their XRD patterns exhibit no reflexes (Fig. 6.4 (A) and (C)); the XRD pattern of FeF_3-SrF_2, however, exhibits very broad reflexes that refer to a nanocrystalline SrF_2 phase. The results suggest that FeF_3-SrF_2 has a higher crystallisation degree. With increasing content of MF_2, all the FeF_3-MF_2 samples begin to show structural characteristics of the corresponding MF_2 phases. Their XRD patterns share one common feature: the broadness of the reflexes, suggesting that these ternary fluorides consist of nanocrystallites.

FeF_3-CaF_2 and FeF_3-SrF_2 were further investigated by electron microscopy. The HRTEM images (Fig. 6.5 (A): (a) and (B): (a)) provide direct proofs for the materials' nanoscopic nature. Nanocrystallites with clear lattice planes are recognised in both samples, confirming the deduction from XRD patterns. Compared with FeF_3-MgF_2 (see Fig. 5.13), FeF_3-CaF_2 and FeF_3-SrF_2 contain larger nanocrystallites. With increasing atomic numbers of the M metals, the following tendency in the crystallite size was observed: FeF_3-MgF_2 (2-3 nm) < FeF_3-CaF_2 (5-10 nm) < FeF_3-SrF_2 (~ 20 nm). Moreover, in the HRTEM image of FeF_3-SrF_2, nanocrystallites of nonuniform sizes can be observed.

STEM images of FeF_3-CaF_2 and FeF_3-SrF_2 are provided in order to give a clear view of their morphology and porosity (Fig. 6.5 (A): (b) and (B): (b)). The bright regions refer to aggregates or agglomerates while the dark regions indicate the voids in-between, *i.e.* the pores. The FeF_3-CaF_2 particles are smaller and more uniform in size as compared with FeF_3-SrF_2. Macropores (Ø > 50 nm) are visualised in the STEM image of FeF_3-SrF_2. In contrast, no macropores are observed in the images of FeF_3-CaF_2 or FeF_3-MgF_2 samples.

Based on EDX, the elemental distribution of FeF_3-CaF_2 and FeF_3-SrF_2 was determined in selected regions (corresponding to the STEM images). Similar to FeF_3-MgF_2 (Fig. 5.13), FeF_3-CaF_2 and FeF_3-SrF_2 also show a homogeneous distribution of Fe and M (here M = Ca or Sr). Thus in spite of different M metals and the M-to-Fe ratios, FeF_3 dispersed homogeneously in the MF_2 matrix.

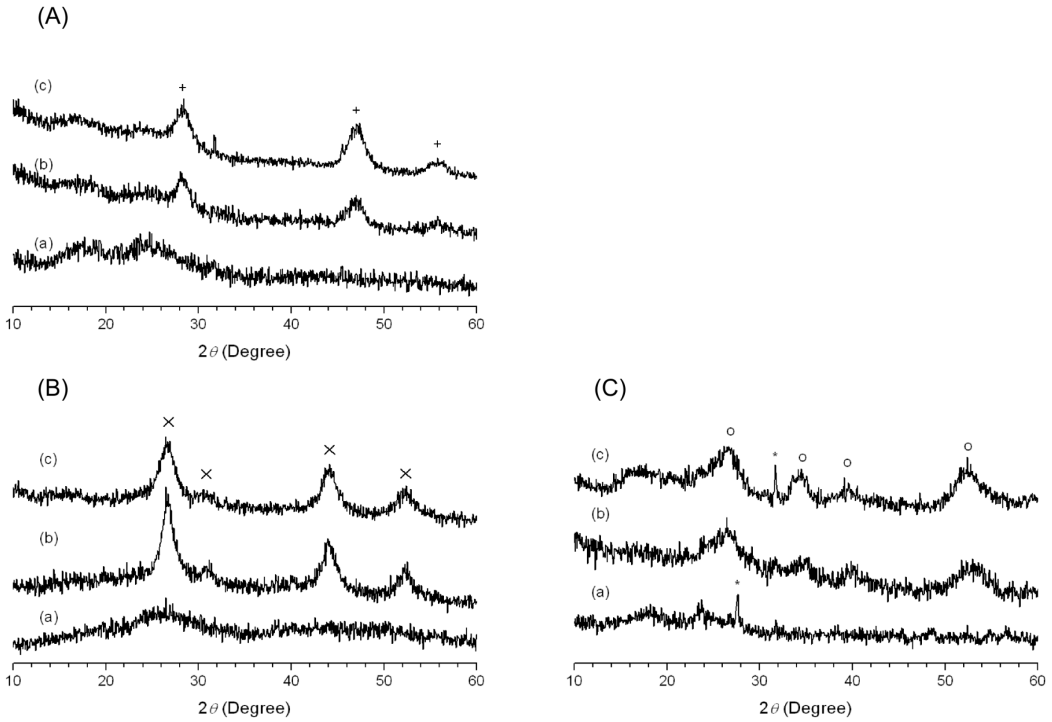

Fig. 6.4 Powder XRD patterns of (A) FeF_3-CaF_2: (a) fc-1, (b) fc-4, and (c) CaF_2; (B) FeF_3-SrF_2: (a) fs-1, (b) fs-7, and (c) SrF_2; (C) FeF_3-ZnF_2: (a) fz-1, (b) fz-7, and (c) ZnF_2;* refers to reflexes from sample holder, + refers to an CaF_2 phase in PDF 35-816, × refers to a SrF_2 phase in PDF 88-2294, and ° indicates a ZnF_2 phase in PDF 7-214.

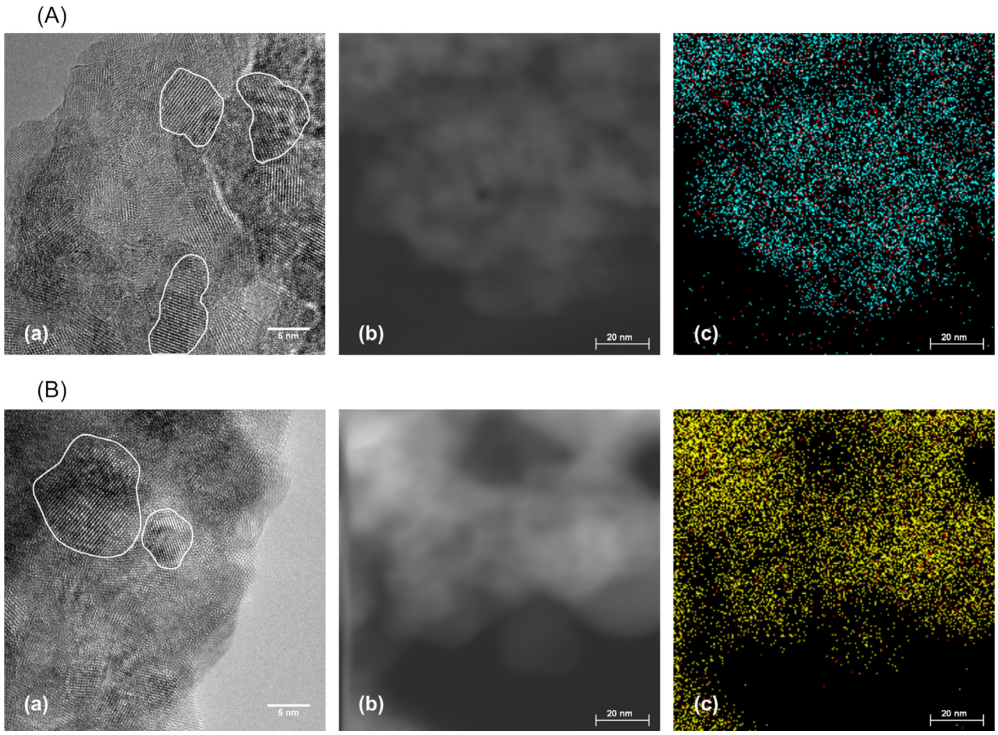

Fig. 6.5 (A) (a) HRTEM image (scale: 5 nm), (b) STEM image (scale: 20 nm), and (c) the corresponding hypermap of Fe and Ca elements of fc-4; (B) (a) HRTEM image (scale: 5 nm), (b) STEM image (scale: 20 nm), and (c) the corresponding hypermap of Fe and Sr elements of fs-7 (red: Fe; blue: Ca; yellow: Sr).

6.3 Surface characterisation

6.3.1 Surface area and porosity

Surface area and porosity of FeF_3-MF_2 samples were characterised by N_2 adsorption-desorption measurements. Due to the low Ca-to-Fe ratio of fc-1, this sample maintains the macroporous features of FeF_3 and shows type II isotherms. Other FeF_3-CaF_2 samples, however, present type IV isotherms that are typical for mesoporous material (Fig. 6.6 (A)). With increasing CaF_2 content, a type H1 hysteresis loop appears in the isotherms of FeF_3-CaF_2 samples. This type of hysteresis loops indicates cylindrical pores that are of uniform size. In comparison to FeF_3-CaF_2, all the FeF_3-SrF_2 samples, regardless of the Sr-to-Fe ratio, possess type II isotherms with a type H3 hysteresis loop. This type refers to macroporous pores of nonuniform size. As expected, the isotherms of FeF_3-ZnF_2 samples assemble similar features as that of FeF_3-MgF_2. They also show a type H2 hysteresis loop that refers to nonuniform pores. The isotherm of FeF_3-ZnF_2 switches to a "ZnF_2" type with increasing Zn-to-Fe ratio. However, neither FeF_3-CaF_2 nor FeF_3-SrF_2 samples present any porous characteristics of the corresponding MF_2 even at high M-to-Fe ratios. Therefore, introducing FeF_3 into CaF_2 or SrF_2 probably largely changed the porosity of the matrix, while it has little influence on ZnF_2.

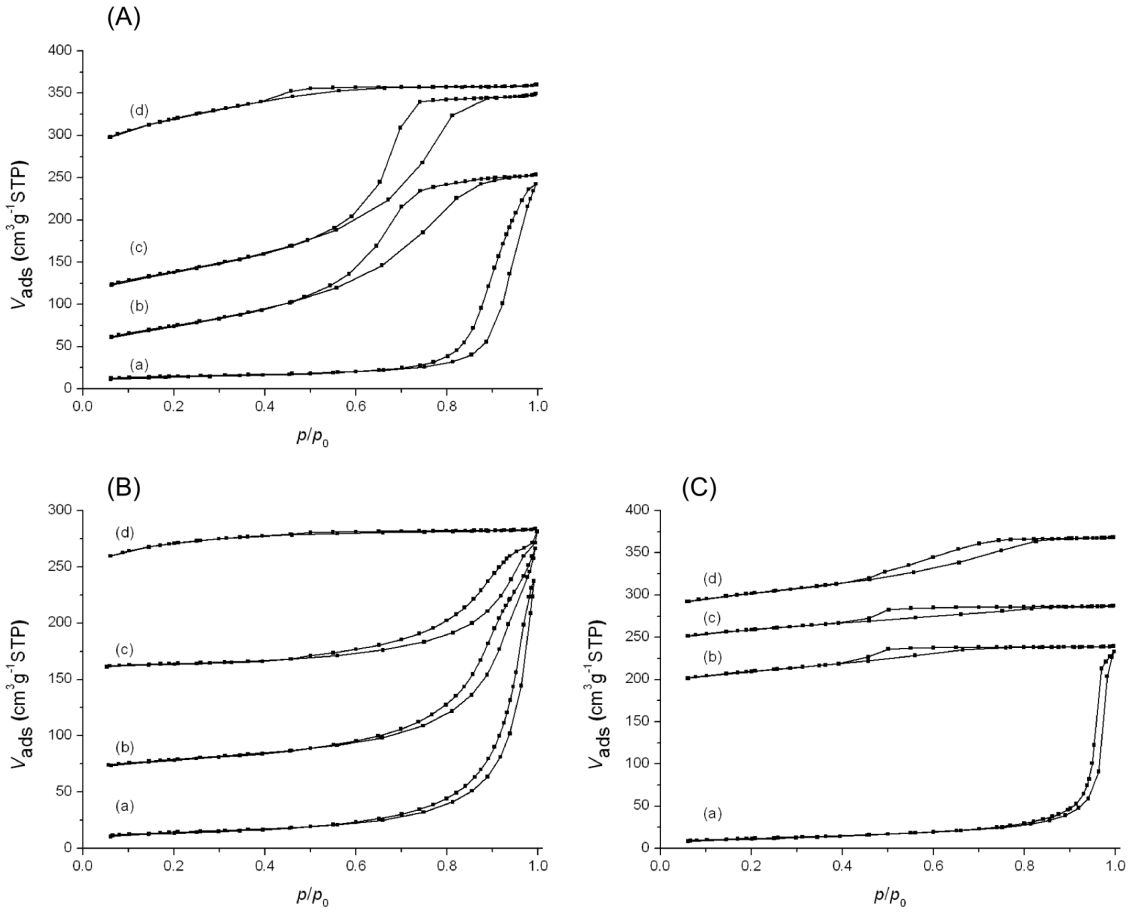

Fig. 6.6 (A) N_2 adsorption-desorption isotherms of (a) fc-1, (b) fc-4, (c) fc-7, and (d) CaF_2; (B) N_2 adsorption-desorption isotherms of (a) fs-3, (b) fs-5, (c) fs-7, and (d) SrF_2; (C) N_2 adsorption-desorption isotherms of (a) fz-1, (b) fz-5, (c) fz-9, and (d) ZnF_2.

Furthermore, surface area and pore size of FeF_3-MF_2 were calculated and plotted versus the M-to-Fe ratio. Fig. 6.7 summarises the porous characteristics of these samples. Generally, the surface area of the ternary FeF_3-MF_2 is much larger than that of FeF_3. The surface area of FeF_3-CaF_2 samples increases drastically with the Ca-to-Fe ratio. The flattening of the curve at high ratios reflects that as the Ca content increases, surface area becomes less responsive to Ca. Similar results were discovered in the study on FeF_3-MgF_2 samples (Fig. 5.14). In comparison, the surface area of FeF_3-SrF_2 and FeF_3-ZnF_2 increases less significantly with M, and is smaller than that of FeF_3-CaF_2 or FeF_3-MgF_2.

Using different MF_2 as matrix has changed not only the surface area but also the pore size. Generally, ternary FeF_3-MF_2 samples show a smaller average pore diameter as compared with FeF_3. The average pore diameter of FeF_3-CaF_2 and FeF_3-ZnF_2 first decreases rapidly with increasing MF_2 content, and then remains at the minimum and forms a plateau in the curve. The average pore diameter of FeF_3-CaF_2 is about 6 nm in the plateau region, while that of FeF_3-ZnF_2 is about 3 nm, similar to the pore diameter of FeF_3-MgF_2 (2 nm). The average pore diameter of FeF_3-SrF_2 decreases much slower compared with the other two samples. Moreover, though the average pore diameter of FeF_3-SrF_2 lies in mesoporous region, the adsorption-desorption isotherms and STEM images show the existence of macropores in these samples.

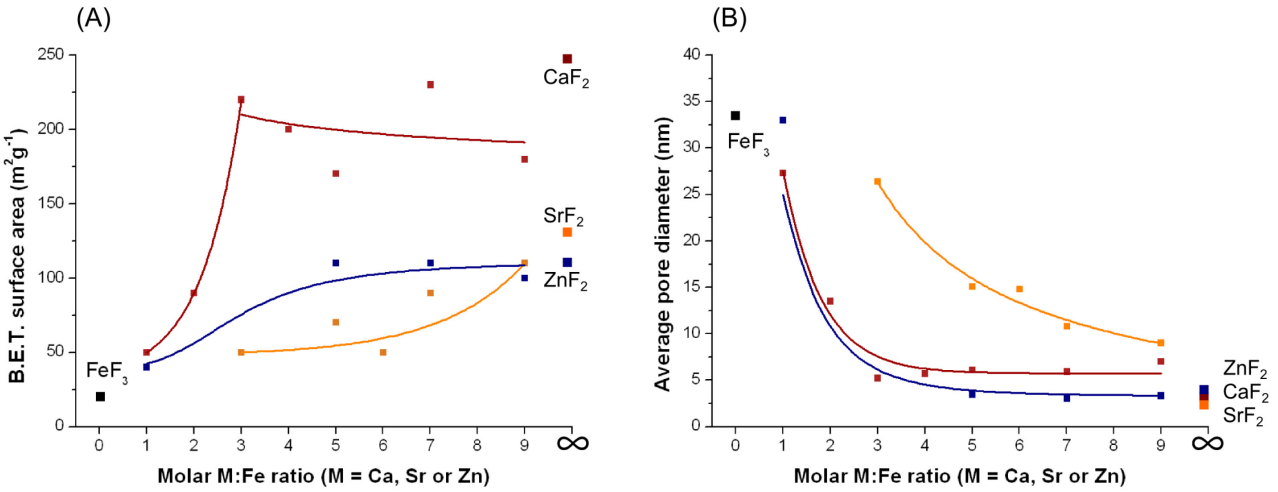

Fig. 6.7 (A) Surface area of FeF_3-MF_2 samples versus the molar M-to-Fe ratio (M = Ca, Sr, or Zn); (B) average pore diameter of FeF_3-MF_2 samples versus the molar M-to-Fe ratio. Results of FeF_3 and corresponding MF_2 are provided as references.

6.3.2 Surface acidity

Surface acidity of the FeF_3-MF_2 samples was studied by IR spectroscopy equipped with chemisorption devices. Different probe molecules (NH_3, pyridine, and CD_3CN) were employed to determine the type of surface acid sites (Lewis or Brønsted sites) and their strengths.

Fig. 6.8 shows the differential spectra of one FeF_3-CaF_2 sample, fc-4, after saturated with NH_3. The 1410 cm^{-1} band can be assigned to protonated NH_4^+ species, indicating Brønsted acidity. This band shifts to lower wavenumber range ($\Delta\delta$ = 26 cm^{-1}) compared with that in the spectra of fm-2 (see Fig. 5.16); this suggests that the Brønsted acidity of FeF_3-CaF_2 is probably weaker than that of FeF_3-MgF_2. The vibration band at 1222 cm^{-1} and the shoulder at 1183 cm^{-1} can be assigned to the coordinated NH_3 species that refers to the surface Lewis sites. The broad peak at a lower wavenumber range (1134-1124 cm^{-1}) corresponds to H-bonding species that is typical for weak Brønsted acidity. The negative peak at 1258 cm^{-1} is probably due to the disturbance of NH_3 on some residual acetate groups.

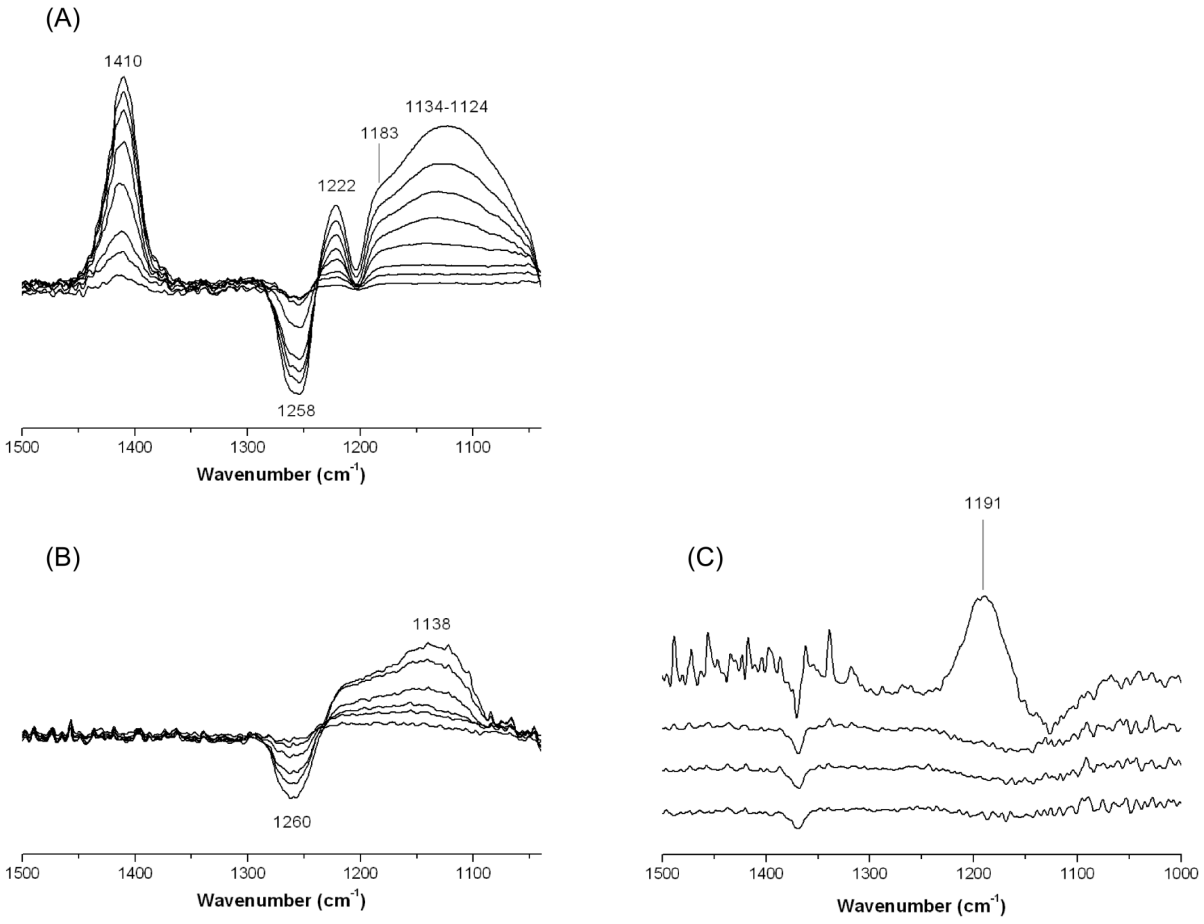

Fig. 6.8 Differential IR spectra of (A) fc-4, (B) fs-7, and (C) fz-7 saturated stepwise with NH_3.

With NH_3 as probe molecule, both Lewis and Brønsted acid sites were determined on the surface of FeF_3-CaF_2. However, the differential spectra of FeF_3-SrF_2 (fs-7) show one single band at 1138 cm^{-1} that indicates H-bonding

species, corresponding to weak Brønsted sites. Similarly, only a single band at 1191 cm^{-1} can be observed in the spectra of FeF_3-ZnF_2 (fz-7), and this band refers to coordinated NH_3 at Lewis acid sites. No vibration bands corresponding to protonated NH_4^+ were recorded in the spectra of both samples. One possible reason is that the Brønsted sites of these two samples are not strong enough to protonate NH_3. Another possible explanation is there is only a low coverage of hydroxyls (potential Brønsted sites) on the surface, but the protonated NH_4^+ requires adjacent -OH for stabilisation.[55] In both fs-7 and fz-7 samples, the high M-to-Fe ratio results in a low concentration of FeF_3 that should carry the Brønsted sites. To solve this problem, pyridine was used as probe molecule to investigate FeF_3-SrF_2 and FeF_3-ZnF_2, because it is a stronger base than NH_3 in gas phase (proton affinity in gas phase: pyridine 922.2 $kJ \cdot mol^{-1}$; NH_3 857.7 $kJ \cdot mol^{-1}$).[56]

In the differential spectra of fs-7 after pyridine adsorption (Fig. 6.9), the two bands at 1641 and 1614 cm^{-1} can be assigned to protonated (PyH^+) and coordinated (PyrL) species, respectively. These bands arise from the vibration mode 8a of pyridine.[57] The band at 1598 cm^{-1} refers to H-bonding species on both Lewis and Brønsted sites.[5] Thus both Brønsted and Lewis acid sites are determined on the surface of FeF_3-SrF_2. The differential spectra of fz-7 after, however, show no vibration bands that can be analysed. This is probably due to the sample's weak Brønsted acidity that even cannot protonate pyridine. Nevertheless, the catalytic results in Chapter 7 confirmed that FeF_3-ZnF_2 samples should also exhibit some Brønsted acid sites.

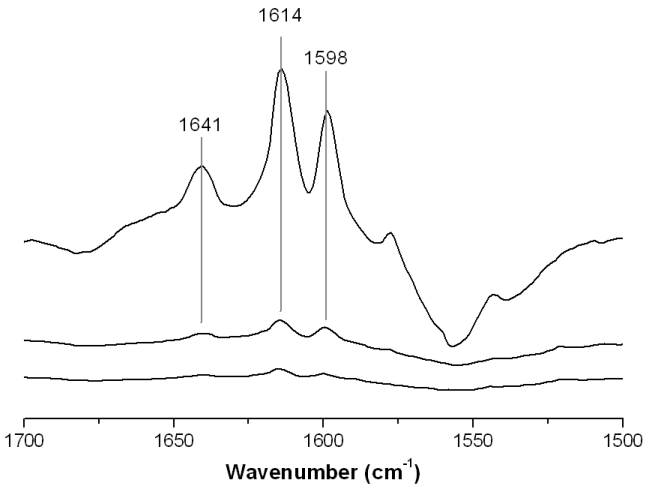

Fig. 6.9 Differential IR spectra of fs-7 saturated stepwise with pyridine.

CD_3CN was used as probe molecules to distinguish the strengths of Lewis acid sites on the surface of FeF_3-MF_2. As discussed in 5.3.2, the vibration band at 2313-2318 cm^{-1} refers to strong Lewis acid sites, while the band in lower wavenumber range (about 2260-2290 cm^{-1}) indicates weak Lewis sites. Interestingly, a decreasing tendency in Lewis acidity can be concluded in the order of Zn, Ca, and Sr. Strong Lewis acid sites are predominant on the surface of FeF_3-ZnF_2, which is similar to the situation on FeF_3-MgF_2 surface. This result was not surprising considering the similarity between ZnF_2 and MgF_2. In comparison, weak Lewis acid sites are the main species of

the surface of FeF_3-SrF_2. On the surface of FeF_3-CaF_2, strong and weak Lewis sites coexist and the intensity of the corresponding bands are comparable. The band at 2114-2118 cm^{-1} in these spectra corresponds to the symmetric CD_3 stretching. Physisorbed species resulting in bands at about 2220-2260 cm^{-1} were recorded in the spectra of FeF_3-CaF_2 and FeF_3-SrF_2 samples. The so-called trio bands (see 4.3.2 and 5.3.2) corresponding to very strong Brønsted sites are not observed in the spectra of FeF_3-MF_2. The Brønsted sites on the surface of these samples are not strong enough to protonate CD_3CN.

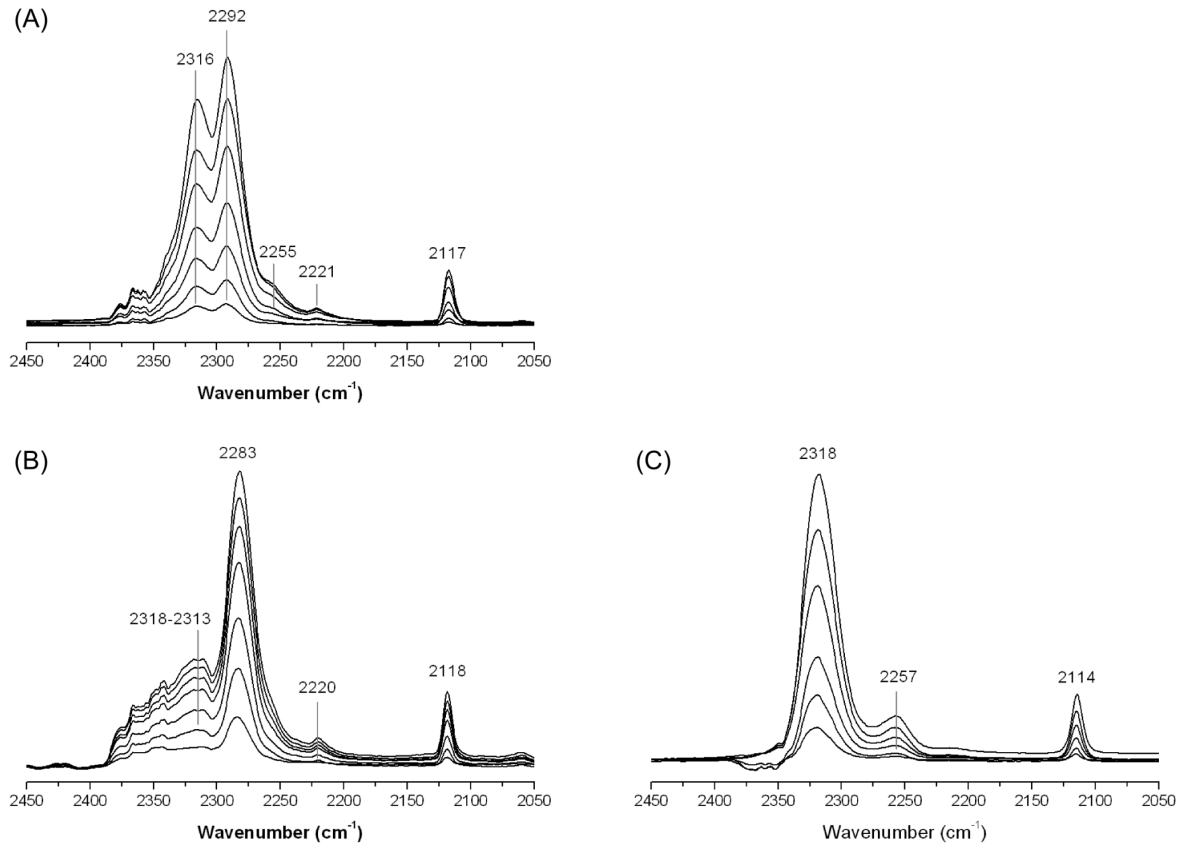

Fig. 6.10 Differential IR spectra of (A) fc-4, (B) fs-7, and (C) fz-7 saturated stepwise with CD_3CN.

In conclusion, Table 6.3 summarises the surface acidity of all ternary FeF_3-MF_2 materials (including FeF_3-MgF_2). With the help of chemisorption-IR, medium strong Brønsted acid sites were determined on the surface of FeF_3-MgF_2, FeF_3-CaF_2, and FeF_3-SrF_2. Only Lewis sites were detected on the surface of FeF_3-ZnF_2; its Brønsted acid sites are probably too weak to be detected by IR. Moreover, strong Lewis acid sites are predominant on the FeF_3-MgF_2 surface, while weak Lewis sites are the main species on the surface of FeF_3-SrF_2. The surface acidity of FeF_3-CaF_2 lies in-between with both strong and weak Lewis acidity. This trend indicates that the strengths of Lewis/Brønsted sites can be easily tuned by using different MF_2 as matrix, allowing the syntheses of catalysts with desirable surface acidity.

Table 6.3 Summary of surface acidity of FeF_3-MF_2.

Sample	Molar M-to-Fe ratio	Lewis acidity	Brønsted acidity
FeF_3-MgF_2	2	Strong	Medium strong
FeF_3-CaF_2	4	Strong sites ≈ weak sites	Weak/medium strong
FeF_3-SrF_2	7	Strong sites <<weak sites	Weak/medium strong
FeF_3-ZnF_2	7	Strong	Too weak to be detected

6.4 Summary

In this chapter, three new FeF_3-MF_2 materials (M = Ca, Sr, or Zn) were prepared and characterised. The one-step sol-gel route reported in Chapter 5 has been successfully applied on other ternary fluorides. Bulk and surface characterisation of FeF_3-MF_2 samples revealed their physicochemical properties. Ternary FeF_3-MF_2 materials exhibited the nanoscopic features as found for other sol-gel prepared materials. The partially hydroxylated FeF_3 distributed homogeneously in the MF_2 matrix. Using MF_2 as matrix significantly increased the surface area and reshaped the porous structure. More importantly, in all the three FeF_3-MF_2 systems, the hydroxyl groups that were introduced by pre-dehydration treatment of the iron nitrate precursor were preserved after fluorination. As elucidated by chemisorption-IR, these hydroxyl groups, or at least some of them, exist on the surface and act as Brønsted acid sites; thus the FeF_3-MF_2 samples can be used as bi-acidic catalysts. Finally, systematic changes were observed in the strengths of surface acid sites and porosity of the FeF_3-MF_2 samples, providing new possibilities to synthesise nanoscopic metal fluorides with tunable surface properties.

7 Catalytic activity of FeF_3-based materials in isomerisation of citronellal to isopulegols

The developments of the FeF_3-based materials are described in Chapter 4, 5, and 6. In this chapter, their catalytic activities are evaluated by the isomerisation of citronellal to isopulegols. The results will not only offer evidences to prove these materials' potential in heterogeneous catalyses, but also help us to understand how their surface properties (*i.e.* surface area, porosity, and surface acidity) influence their catalytic performance.

7.1 Isomerisation of citronellal to isopulegols

Citronellal, isopulegol, and menthol are three frequently used chemicals in the fragrance industry.[58] The isomerisation reaction of citronellal to isopulegols is one of the key steps in synthesising menthol,[44] which is widely used in medicaments, cosmetics, and food additives.[59] It represents an intramolecular carbonyl-ene reaction. This type of reaction involves unsaturated carbonyl compounds, in which an allylic hydrogen (an "ene") reacts with a carbonyl (an "enophile") to form a new bond with the migration of the ene double bond and 1,5-hydrogen shift (Fig. 7.1).[60, 61] The product of the citronellal isomerisation reaction, isopulegol, has three asymmetric carbon atoms, and thus gives rises to eight stereoisomers (Fig. 7.2). Thermodynamic stability of these stereoisomers influences their molar distribution in the products. A typical distribution of the stereoisomers in molar ratio was reported by W. Oppolzer and V. Snieckus:[61] isopulegol (60%), neo-isopulegol (20%), iso-isopulegol (15%), and neoiso-isopulegol (5%). This distribution was obtained from pyrolytic process, as the isomerisation of citronellal can proceed at 150-300°C; using acid catalysts will change the product-distribution as well as lower the reaction temperature.[61, 62] Therefore various catalysts have been developed for the isomerisation of citronellal.

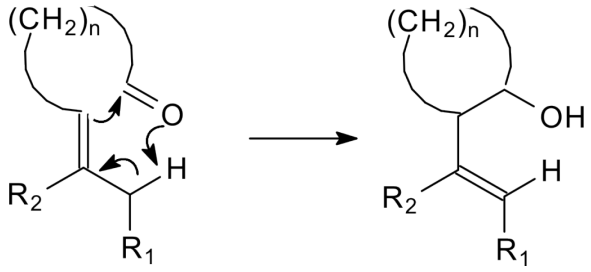

Fig. 7.1 Intramolecular carbonyl-ene reaction.

Both homogeneous and heterogeneous acid catalysts have been developed for the isomerisation of citronellal. Initially, Lewis acids like zinc halides ($ZnCl_2$, $ZnBr_2$, and ZnI_2), $FeCl_3$, $AlCl_3$, and $SbCl_3$ were investigated.[27] Especially, $ZnBr_2$ has shown high diastereoselectivity towards (-)-isopulegol and hence has been used in the industrial synthesis process (Takasago process) of (-)-menthol. For industrial applications (-)-menthol is the most important isomer because it possesses a unique cooling effect out of all the other stereoisomers.[59, 63] High dia-

stereoselectivity towards (-)-isopulegol is therefore appreciated as this isomer is a convenient precursor to synthesise (-)-menthol. The drawbacks of these commonly used Lewis acid catalysts, however, are as noteworthy as their advantages. In most reports, stoichiometric amounts of catalysts are needed, and pollution caused by the acid waste is difficult to avoid. In addition, the recovery of these catalysts is also problematic, restricting the sustainability of these processes. Other substances like molybdenum (II) and tungsten (II) complexes like $PhCH_2(Et)_3N^+[M(CO)_4ClBr_2]^-$ and $M(CO)_5(OTf)_2$ (M = Mo or W) were reported as active catalysts.[64] They show, however, preference towards the formation of neo-isopulegol, a fragrance ingredient that has less industrial value than the desired (-)-isopulegol. Scandium trifluoromethanesulfonate[65] was developed as an efficient catalyst with high diastereoselectivity (> 80%) towards the (-)-isopulegol; but the reaction required subambient temperature to achieve high yields. These homogeneous catalysts are usually difficult to separate and thus are inconvenient for recycled usage; therefore, heterogeneous catalysts are more attractive for this reaction. A number of heterogeneous catalysts have been reported. The most studied examples include zeolites (*e.g.* H-MCM-41, H-MCM-22, and Sn- or Zr-zeolite beta),[66, 67] mixed oxides (SiO_2-TiO_2, -ZrO_2, or –Al_2O_3) with and without Cu,[68] silica-supported heteropoly acid ($H_3PW_{12}O_{40}$),[69] and ZrO_2-based catalysts.[28] Moreover, partially hydroxylated aluminium fluoride also showed great potential in this reaction with high conversion of citronellal and high selectivity to isopulegols (including all diastereoisomers).[13]

Meanwhile, the reaction mechanism in the heterogeneous process has been investigated. Although the reaction was initially considered to be catalysed by Lewis acids, later studies show that it actually requires the participation of both Lewis and Brønsted acid sites to achieve high yields towards isopulegols.[28, 67] Thus the isomerisation reaction of citronellal can be used as an excellent touchstone to prove the surface bi-acidity. It was therefore chosen as the model reaction to evaluate the catalytic potential of FeF_3-based materials.

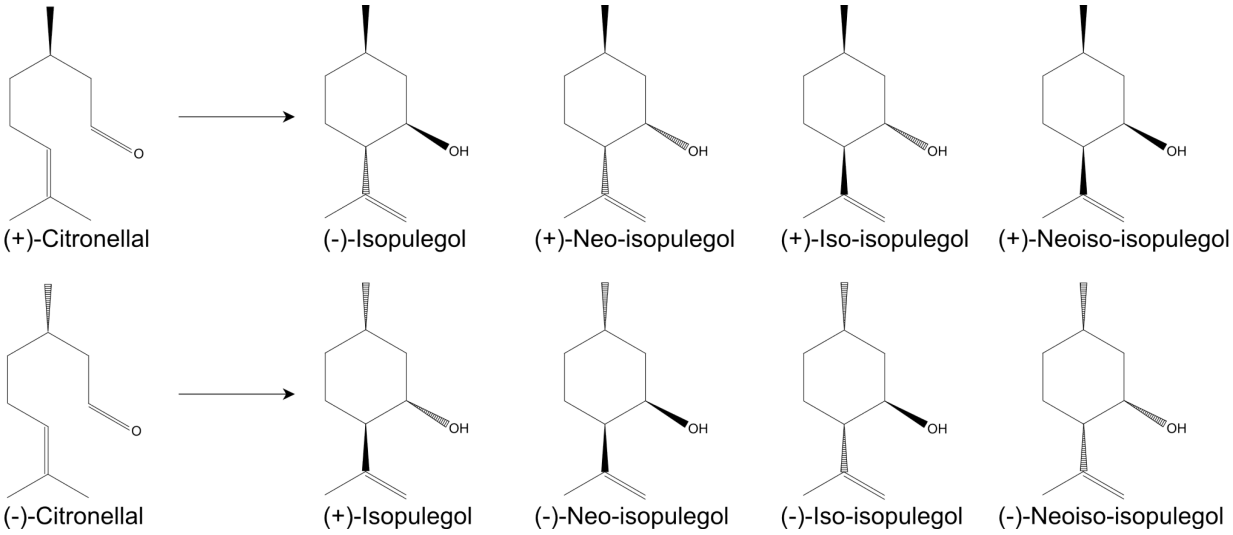

Fig. 7.2 Isomerisation of (±)-citronellal to isopulegol isomers: (±)-isopulegol, (±)-neo-isopulegol, (±)-iso-isopulegol, and (±)-neoiso-isopulegol.

7.2 Results and discussion

7.2.1 Partially hydroxylated FeF_3

Since the isomerisation of citronellal requires the participation of both Lewis and Brønsted acid sites, it can offer a most convincing proof for the bi-acidity of the FeF_3-based materials. As discussed in Chapter 4, hydroxyl groups (potential Brønsted acid sites) were introduced to iron fluoride by the pre-dehydration treatment; chemisorption-IR found that the hydroxyls existed on the surface and acted as Brønsted acid sites. Whether these Brønsted sites are active in catalytic reactions, however, still needs to be examined; and thus the catalytic results here will provide a final proof.

In this work, because a (±)-citronellal was used as reactant, the eight isopulegol stereoisomers can be divided into four groups each containing a pair of enantiomers. For brevity the "(±)-" symbol is omitted in the following text unless otherwise denoted. A blank test without catalysts was taken under the reaction temperature (80°C). The conversion of citronellal in the blank test was 35%, but no isopulegols were formed (Table 7.1). Thermal decomposition of citronellal and formation of some nonvolatile by-products may contribute to the conversion. Similar by-products have been also observed in the isomerisation reaction of citronellal.[70] A crystalline FeF_3 (commercially available) was tested in this reaction as well. It showed no activity towards this reaction as the conversion was equal to that of the blank test and the selectivity towards isopulegols was negligible (Table 7.1).

Table 7.1 Summarised results of the blank test and the test with crystalline FeF_3.

	Conversion of citronellal (%)	Selectivity to isopulegols (%)
Blank test	35	–
c-FeF_3 [a]	35	1

a: Crystalline FeF_3; catalysts amount: 20 mg/1 mmol citronellal.

In comparison, the nanoscopic FeF_3 materials showed considerable potential in catalysing this reaction. Without the pre-dehydration treatment, the sol-gel prepared FeF_3 was able to catalyse the isomerisation reaction and showed about 11% selectivity towards isopulegols. Using this catalyst, the conversion of citronellal (29%) is lower than that of the blank test (35%), suggesting that the decomposition of citronellal and other side-reactions are probably hindered. The catalytic performance of FeF_3 can be significantly enhanced by the pre-dehydration treatment of iron nitrate precursor: under the same reaction conditions, the pre-dehydrated samples all showed much higher conversion and selectivity than the untreated one. Fig. 7.3 compares the catalytic results of partially hydroxylated FeF_3 that was pre-dehydrated at different temperatures. Notably, the pre-dehydration temperature seems to have a strong impact on the catalytic performance of FeF_3. The FeF_3 sample that was pre-dehydrated at 50°C showed a conversion of 47% with a selectivity of 46% to isopulegols. FeF_3 pre-dehydrated at 65°C exhibited the highest activity with 74% conversion and 72% selectivity. The conversion of citronellal remained high

(72%) when the sample was pre-dehydrated at a higher temperature (80°C); the selectivity to isopulegols, however, decreased significantly to about 48%. Thus an optimised pre-dehydration temperature was found at 65°C.

Interestingly, using these FeF_3 materials as catalysts leads to similar diastereoselectivity towards (±)-isopulegol. Despite the different conversion and selectivity, the diastereoselectivity of all these samples lies between 60-75%. Previous studies showed that generally, in a heterogeneous process, all the diastereoisomers were formed, and they followed the typical molar distribution as suggested by W. Oppolzer and V. Snieckus;[61] usually the diastereoselectivity towards (±)-isopulegol varies between 52-75%. In this work, the FeF_3 catalysts have not changed the thermodynamic stability of isopulegol stereoisomers; and hence the four pairs of diastereoisomers follow the same distribution even with different FeF_3 samples. This ratio was also found in the catalytic results of all the ternary FeF_3-MF_2 materials (here M = Mg, Ca, Sr, or Zn). Therefore, the discussion and comparison in this chapter concentrate on the conversion of citronellal and the chemical selectivity to isopulegols (including all the diastereoisomers).

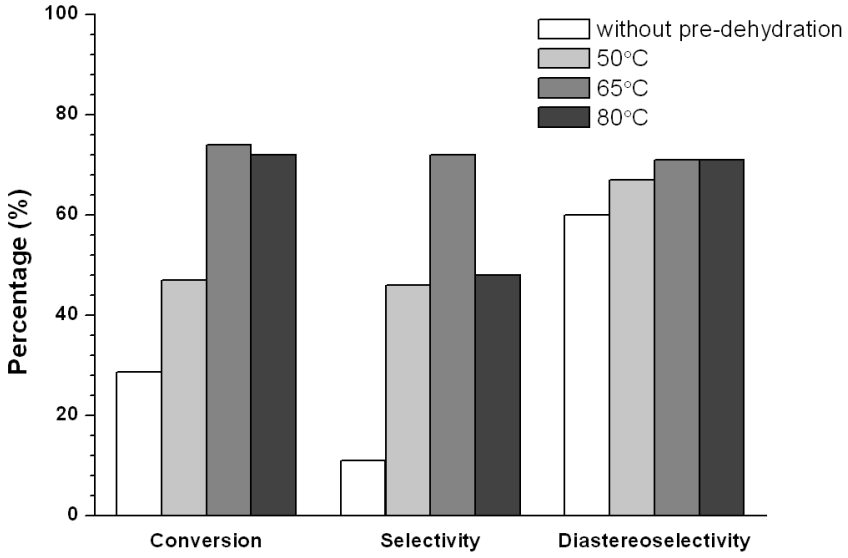

Fig. 7.3 Conversion of citronellal, selectivity to isopulegols, and diastereoselectivity to (±)-isopulegols with FeF_3 (without pre-dehydration, pre-dehydrated at 50°C, 65°C, and 80°C) as catalysts; 20 mg catalysts/1 mmol citronellal was used in each test.

The partially hydroxylated FeF_3 has been proved to be active in the model reaction. Subsequently, the robustness of this type of catalysts needs examination. A leaching test was therefore performed, in which the catalysts were filtered to see if the reaction continued. The corresponding results are summarised in Table 7.2. The conversion of citronellal increased slightly after removing solid-state catalysts, because decomposition of citronellal can proceed without catalyst, as indicated by the blank test (Table 7.1). The formation of isopulegol stopped after the filtration of the catalysts, resulting in a decrease of selectivity. Moreover, since the most probable leaching species are the residual soluble Fe compounds, another test was taken with $Fe(NO_3)_3 \cdot 9H_2O$ as the catalyst. The

amount of $Fe(NO_3)_3 \cdot 9H_2O$ was determined by calculating the maximum nitrogen content: the partially hydroxylated FeF_3 (pre-dehydrated at 65°C) exhibited no N according to elemental analysis results (Table 4.2). It is known that the error range of elemental analysis is ±3 wt%; therefore the maximum content of N is 6% in partially hydroxylated FeF_3. Accordingly, the amount of $Fe(NO_3)_3 \cdot 9H_2O$ was calculated from the maximum N content. To ensure that the results of $Fe(NO_3)_3 \cdot 9H_2O$ were comparable with that of the partially hydroxylated FeF_3, this sample was also pre-dehydrated under the same conditions (65°C, under vacuum) before use. An $Fe(NO_3)_x(OH)_{3-x}$ compound was obtained through this treatment. The results showed that although pre-dehydrated $Fe(NO_3)_3 \cdot 9H_2O$ led to the formation of isopulegols, its activity cannot compete with FeF_3. Thus it is unlikely that the reaction undergoes a homogeneous process. In short, the results suggest that no leaching happens in this reaction and the partially hydroxylated FeF_3 acts as a real heterogeneous catalyst.

Table 7.2 Summarised results of leaching tests.

Leaching test		Conversion of citronellal (%)	Selectivity to isopulegols (%)
1. With partially hydroxylated FeF_3 [a]	After 6 h reaction	77	78
	After removing catalysts	83	67
2. With $Fe(NO_3)_3 \cdot 9H_2O$ [b]	After 6 h reaction	16	17

a: Catalysts amount: 20 mg/1 mmol citronellal; b: pre-dehydrated at 65°C under vacuum for 2 h.

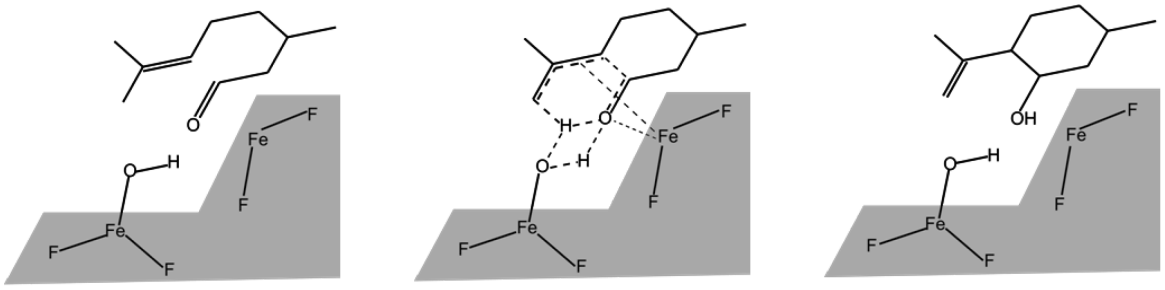

Fig. 7.4 Proposed isomerisation mechanism of citronellal to isopulegol at the active sites of FeF_3-based catalysts.

The catalytic results supported the idea of using partially hydroxylated FeF_3 in heterogeneous catalysis. The surface Lewis and Brønsted acid sites acted synergistically as active centres in the isomerisation reaction of citronellal to isopulegols. The mechanism of this reaction remains under debate, because it may undergo a converted route or a stepwise route with a zwitterion as intermediate. The study on ZrO_2-catalysts as reported by G. K. Chuah *et al.*[28] shed some light on this issue by using a six-ring transition state to explain the roles of Lewis and Brønsted acid sites. The C=C bond was probably activated by the undercoordinated metal centre (the Lewis acid site), and the adjacent hydroxyl group (the Brønsted acid site) assisted the proton transfer. Accordingly, a

possible reaction mechanism at the active sites on the partially hydroxylated FeF_3 surface was proposed in Fig. 7.4.

7.2.2 FeF_3-MgF_2

First of all, since MgF_2 is completely inactive in this reaction (0% selectivity to isopulegols), FeF_3 must be the real active component. The first series of tests used equal amounts of catalysts with varying Fe-contents. The maximum conversion (as well as selectivity) was observed at the molar Mg-to-Fe ratio of about 1.5 (Fig. 7.5 (A)). Since the FeF_3 content varies in samples, the results were normalised to the same amount (10 mg) of FeF_3 in all cases (Fig. 7.5 (B)). Both conversion and selectivity increased drastically for Mg-to-Fe ratios between 0 and 2. At higher Mg-to-Fe ratios, both measures remained constant. Since the amount of FeF_3, the active species, is unchanged, higher conversion and selectivity are probably caused by changes in other characteristics, *e.g.* the surface area and porosity.

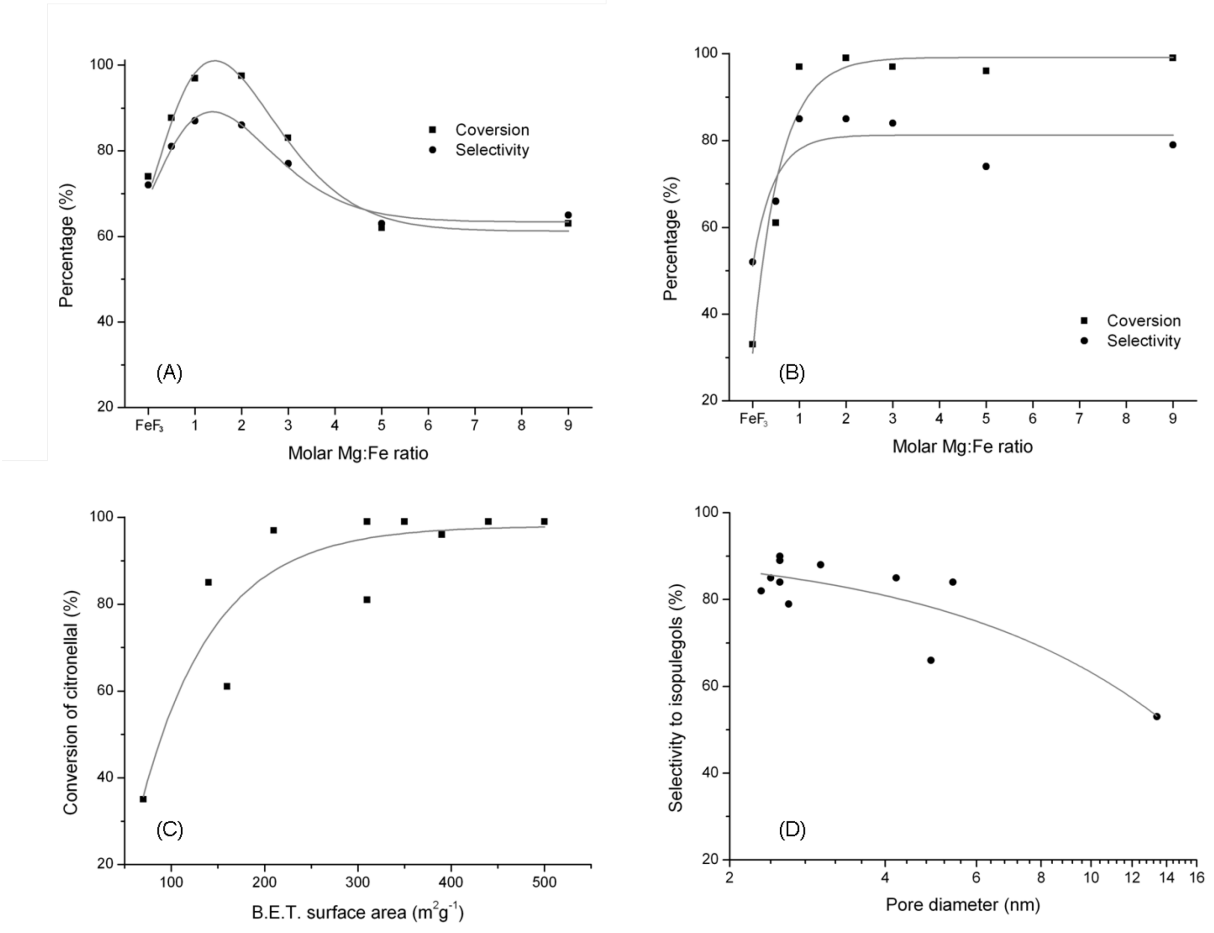

Fig. 7.5 Catalytic results of FeF_3-MgF_2 samples: (A) conversion and selectivity versus the molar Mg-to-Fe ratio (20 mg catalysts/1 mmol citronellal); (B) conversion and selectivity versus the molar Mg-to-Fe ratio (catalysts amounts normalised to 10 mg FeF_3/1 mmol citronellal); (C) conversion of citronellal versus surface area of catalysts; (D) selectivity to isopulegol versus the average pore diameter of catalysts.

The conversion of citronellal was plotted versus the surface area of the fm-*n* samples in Fig. 7.5 (C). Generally, high surface materials are preferred in heterogeneous catalysis. Indeed, the conversion rises rapidly in the surface area region below 300 $m^2 \cdot g^{-1}$. In the high surface area region, however, the conversion approached nearly 100% and hence no further changes were observed.

In previous studies, G. K. Chuah *et al.*[28] discussed the influence of the catalyst's pore size on the selectivity towards isopulegols. It was concluded that small pores preferentially led to isopulegol formation because they suppressed large by-products such as dimerisation product of isopulegols. Similar results were also found for the fm-*n* samples. In Fig. 7.5 (D), the plot proves that high selectivity for isopulegols is only achieved in the low nanometer range of pores below 5 nm. Thus small mesopores or large micropores are favourable for this reaction.

The change of conversion and selectivity with reaction time is presented in Fig. 7.6. The catalyst amount was normalised to 10 mg FeF_3. The isomerisation reaction of citronellal proceeded rapidly in the initial state: the conversion reached about 85% within one hour; it then increased gradually to over 97% at the end of the test. The selectivity to isopulegols decreased slightly from ca. 85% to 80%; it was probably caused by the oligomerisation of isopulegols, which was one of the side-reactions accompanied the isomerisation reaction of citronellal.[28]

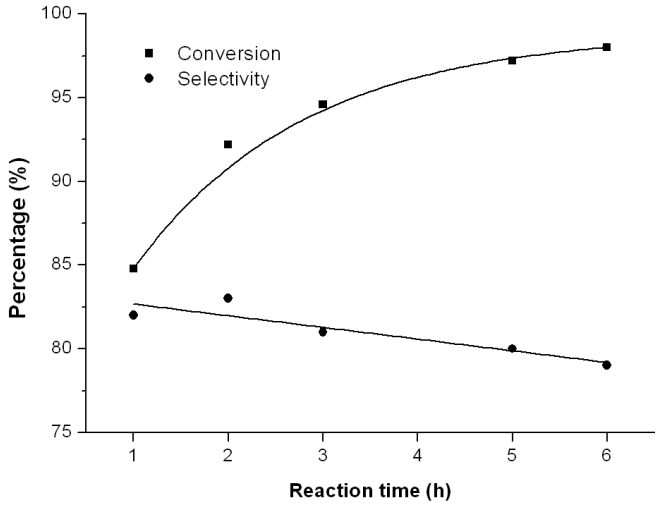

Fig. 7.6 Conversion of citronellal and selectivity to isopulegols versus reaction time with fm-2 as catalysts.

Moreover, the FeF_3-MgF_2 material was also investigated regarding its recycling ability since this is of importance for any realistic application. To examine the robustness of the catalysts, one FeF_3-MgF_2 sample (fm-2) was selected and applied in the recycling tests. Regeneration of catalysts was performed by the following process: the used catalysts were filtered and washed with acetone, and then dried at 80°C under Ar flow for 12 h, or under vacuum for 6 h. The results are summarised in Table 7.3. The recovery rate was calculated by comparing the yields to isopulegols. In the first test, three recycling runs were performed, and the reaction proceeded for 3 h in

each turn. The recovery rate remained almost constant between 77-79%. The decline in catalytic activity is probably due to the coordination of some organic species (*e.g.* reactant, product or by-products) to the surface active sites, since elemental analysis showed significant increase in the carbon content after each run of reaction. Only one recycling run was performed in the second test. The reaction time, however, was not only 3 h but 6 h as in the usual catalytic tests. The recovery rate was *ca.* 95% after the first run. Taking into account the results from the first recycling test, it can be deduced that about 85% of the original yield to isopulegols is to be expected after three recycling runs.

Table 7.3 Summarised results of recycling tests.

	Cycles	Conversion of citronellal (%)	Selectivity to isopulegols (%)	Recovery rate [a] (%)	Carbon content [b] (wt %)	Regeneration method
Test 1 (3 h reaction)	0	75	76	–	0.6	Wash with acetone for 4 times (10 min each); dry at 80°C under Ar flow for 12 h
	1	63	71	79	2.5	
	2	50	69	77	3.6	
	3	44	61	77	4.0	
Test 2 (6 h reaction)	0	98	73	–	0.6	Wash with acetone for 3 times (5 min, 10 min, and 12 h); dry at 80°C under vacuum for 6 h
	1	86	79	95	2.7	

a: Recovery rate = 100%×yield ($cycle_n$)/yield ($cycle_{n-1}$); yield to isopulegols = conversion×selectivity;

b: determined by elemental analysis and the error range is ±3%.

7.2.3 FeF_3-MF_2 (M = Ca, Sr, or Zn)

The ternary FeF_3-MgF_2 materials have been found highly active in the model reaction, the isomerisation of citronellal to isopulegols. Subsequently, the catalytic activity of other FeF_3-MF_2 materials needs to be examined. Since surface characterisations of FeF_3-MF_2 revealed systematic changes in surface area, porosity, and surface acidity, discussions in this section will focus on the consequences of these systematic changes on the catalytic activity of these materials.

The catalytic results of FeF_3-CaF_2 samples are presented in Fig. 7.7. The conversion and selectivity varied simultaneously with the Ca-to-Fe ratio. The curves of conversion and selectivity in Fig. 7.7 (A) exhibit two peaks, corresponding to the Ca-to-Fe ratios of 3 and 7. Using 20 mg FeF_3-CaF_2 as catalyst, the maximum conversion of citronellal was 74%, and the corresponding selectivity to isopulegols was 65%. Compared with FeF_3-MgF_2 materials (see Fig. 7.5 (A)), FeF_3-CaF_2 materials lead to lower conversion as well as lower selectivity in the model reaction. One possible reason is that in the FeF_3-CaF_2 materials, the weight proportion of the active component,

FeF_3, is lower than that in the FeF_3-MgF_2 materials with the same M-to-Fe ratio, because Ca is heavier than Mg. Moreover, considering that the FeF_3 content also varies in different FeF_3-CaF_2 samples, it is necessary to normalise the catalytic results to the same amount of FeF_3 in all cases for a better comparison. As shown in Fig. 7.7 (B), both conversion and selectivity increased drastically for Ca-to-Fe ratio between 1 and 4. At higher ratios, the conversion reached nearly 100% and hence no increase can be expected. The fc-3 sample shows the highest yield to isopulegols with a conversion of 97% and a selectivity of 84%, comparable to that of FeF_3-MgF_2 samples. Hence, evidently the catalytic performance of FeF_3-CaF_2 is similar to FeF_3-MgF_2. Correspondingly, the correlations between surface area and conversion (or between pore size and selectivity) of these two series of materials show the same tendency. This finding leads to the conclusion that high surface area and small pores are preferred. Referring to the surface characteristics of FeF_3-CaF_2 materials in Chapter 6 (see Fig. 6.7), it is clear the fc-3 sample combines the best conditions and is therefore the most active sample in this series.

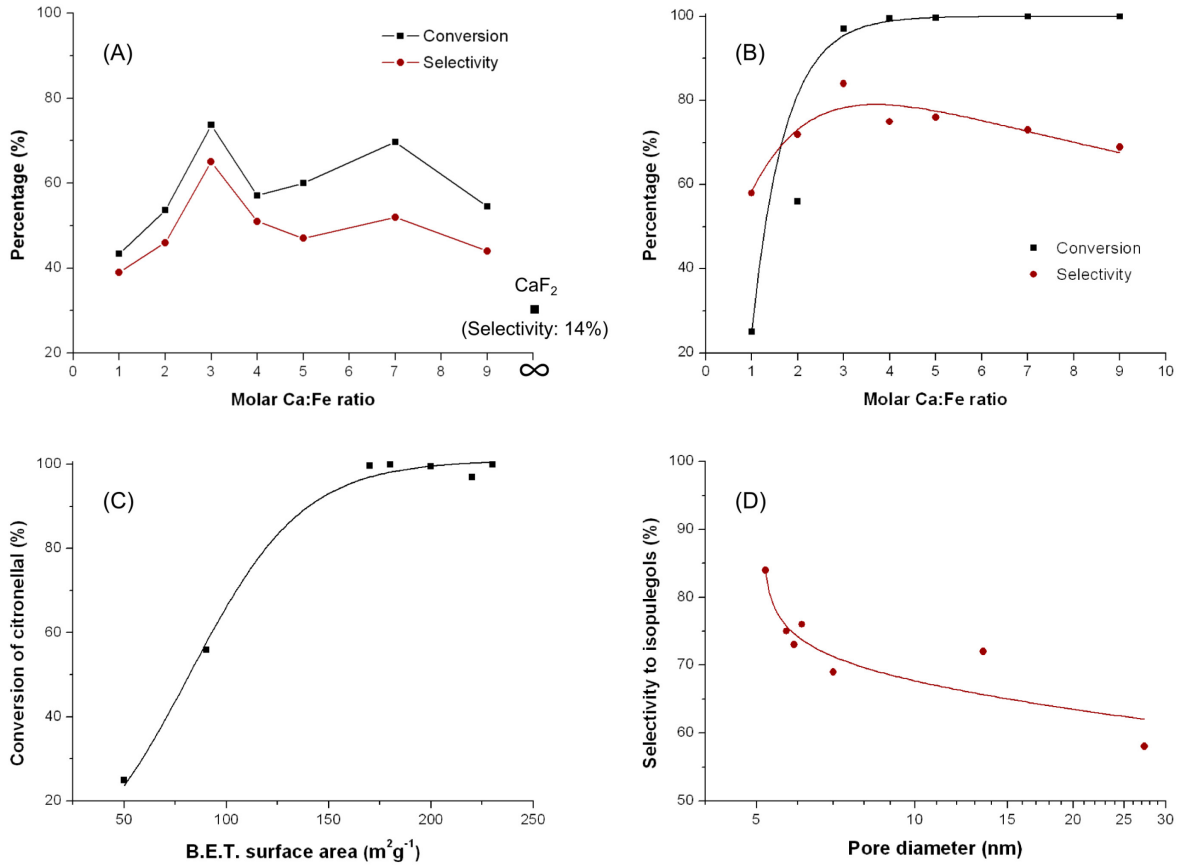

Fig. 7.7 Catalytic results of FeF_3-CaF_2 samples: (A) conversion and selectivity versus the molar Ca-to-Fe ratio (20 mg catalysts/1 mmol citronellal); (B) conversion and selectivity versus the molar Ca-to-Fe ratio (catalysts amounts normalised to 10 mg FeF_3/1 mmol citronellal); (C) conversion of citronellal versus surface area of catalysts; (D) selectivity to isopulegol versus the average pore diameter of catalysts.

Comparing with FeF_3-MgF_2 or FeF_3-CaF_2, FeF_3-SrF_2 samples are probably less competitive in this reaction. Normalising the catalysts amount to 10 mg FeF_3, the conversion curve reached its maximum of nearly 100% at the Sr-to Fe ratio of 7 (Fig. 7.8). The selectivity to isopulegols, however, was noticeably lower than that that of the FeF_3-MgF_2 or FeF_3-CaF_2 catalysts. As discussed above, micropores or small mesopores are favourable in this reaction; thus the much larger average pore diameter of FeF_3-SrF_2 (over 10 nm) may be less competitive for the formation of isopulegols.

The catalytic results of FeF_3-ZnF_2 provide an interesting comparison with FeF_3-MgF_2. These two materials showed similar characteristics in both surface area and porosity, as they showed the same type of N_2 adsorption-desorption isotherms and both consisted of micro-/mesopores of 2-3 nm. Despite their similarity in porous structure, these two types of ternary fluorides showed different activity in the model reaction. The FeF_3-MgF_2 materials, as discussed in 7.2.2, were highly active in this reaction with nearly 100% conversion and over 80% selectivity. In comparison, the FeF_3-ZnF_2 materials showed a maximum conversion of 85% with 65% selectivity. The porous structure is unlikely to be the reason since FeF_3-ZnF_2 materials possess optimum pore size. One possible explanation may be that the selectivity to isopulegols is additionally influenced by other properties such as the surface acidity.

The FeF_3-ZnF_2 and FeF_3-MgF_2 materials both exhibited strong Lewis acidity (see Table 6.3); however, they differed in their surface Brønsted acidity. The predominant species on the FeF_3-MgF_2 surface are medium strong Brønsted acid sites; the predominant species on the FeF_3-ZnF_2 surface, however, are very weak Brønsted acid sites, which were too weak to protonate probe molecules like NH_3 or pyridine. It can be therefore deduced that medium strong Brønsted acid sites are probably required to achieve high selectivity to isopulegols.

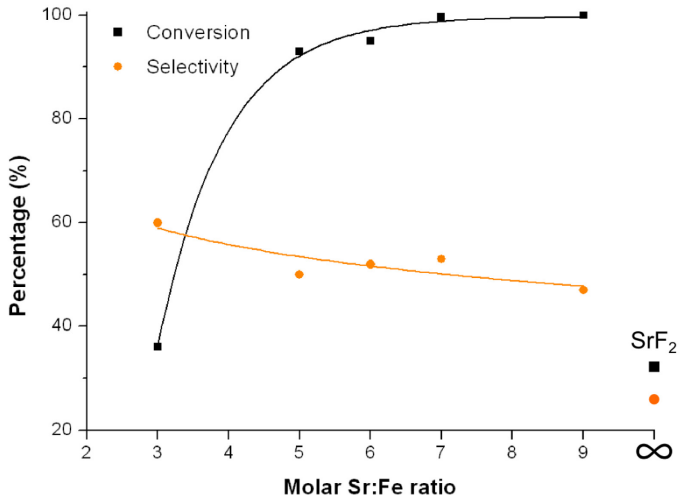

Fig. 7.8 Catalytic results of FeF_3-SrF_2 samples: conversion of citronellal and selectivity to isopulegols versus the molar Sr-to-Fe ratio (catalysts amounts normalised to 10 mg FeF_3/1 mmol citronellal).

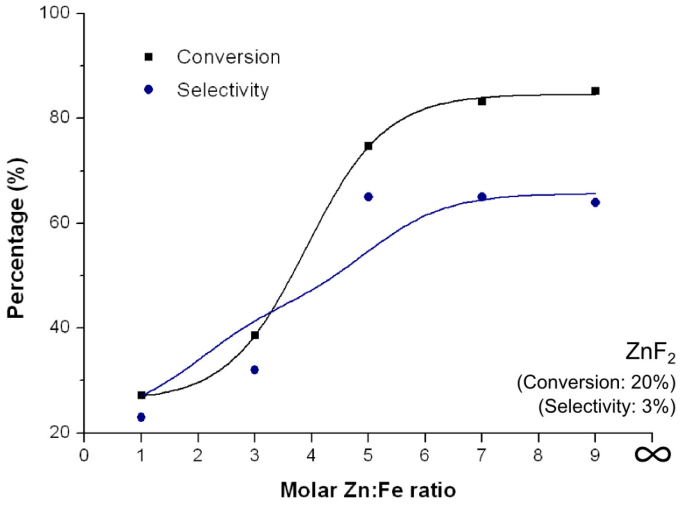

Fig. 7.9 Catalytic results of FeF3-ZnF2 samples: conversion of citronellal and selectivity to isopulegols versus the molar Zn-to-Fe ratio (catalysts amounts normalised to 10 mg FeF_3/1 mmol citronellal).

The changes of conversion and selectivity with reaction time were studied by using FeF_3-CaF_2 and FeF_3-SrF_2 as catalysts. The catalyst amount was normalised to 10 mg FeF_3 in both cases. When FeF_3-CaF_2 was used, the conversion of citronellal increased with reaction time, and reached its maximum after 5 h of reaction; the selectivity to isopulegols, however, increased within the initial 2 h and then remained almost constant. One possible explanation is that in the first 2 h, the side-reactions are overwhelmed by the isomerisation reaction to isopulegols. When the reaction proceeds, side-reactions like the oligomerisation of isopulegols tends to happen.[28] The results with FeF_3-SrF_2 offered another example: within the first 2 h, the conversion of citronellal increased drastically, accompanied by the decrease in selectivity to isopulegols, afterwards the isomerisation and the side-reactions seemed to reach equilibrium and thus the concentration of citronellal and isopulegols remained constant; consequently, the conversion and selectivity curves remain flat.

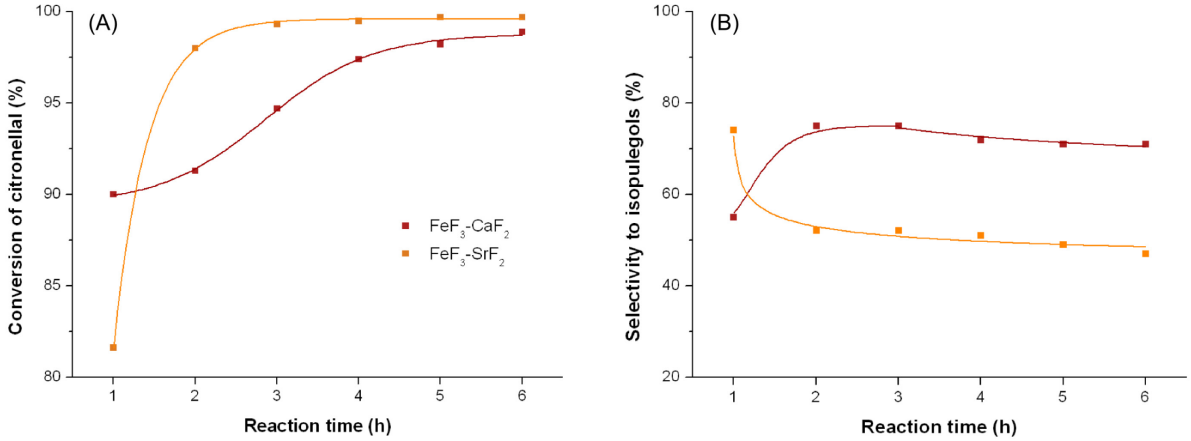

Fig. 7.10 Conversion of citronellal and selectivity to isopulegols versus reaction time with FeF_3-CaF_2 (fc-4) and FeF_3-SrF_2 (fs-7) samples as catalysts.

7.3 Summary

In this chapter, the FeF_3-based materials were evaluated by the isomerisation reaction of citronellal to isopulegols. Their potentials as heterogeneous catalysts were estimated. With both Lewis and Brønsted acid sites on the surface, partially hydroxylated FeF_3 was found to be active in this reaction. The ternary FeF_3-MF_2 catalysts (M = Mg, Ca, Sr, or Zn) showed even higher activities towards the formation of isopulegols, probably because of the high surface area. The correlation between pore size and selectivity to isopulegols was discussed as well. Generally, small pores (micropores or small mesopores of < 5 nm) were favourable in catalysing the isomerisation reaction to isopulegols. Another impact factor was the strengths of dominant acid sites. The comparison between FeF_3-MgF_2 and FeF_3-ZnF_2 demonstrated that medium strong Brønsted acidity is necessary to obtain high yields of isopulegols.

Moreover, leaching and recycling tests were performed to examine the robustness of the FeF_3-based materials. It has shown that leaching does not represent a serious problem for the partially hydroxylated FeF_3 catalyst; a recovery of about 77% of the yield to isopulegols was obtained after three recycling runs using a representative FeF_3-MgF_2 sample. The results supported the expectations of FeF_3-MF_2 materials: as robust bi-acidic solids that are active in the model reaction as heterogeneous catalysts. Consequently, these ternary fluoride materials should be tested in the future with different types of reactions in order to investigate their potentials.

8 Conclusion and prospects

This work presents a substantial development of the sol-gel process that once gave rises to a large variety of oxides. By using hydrogen fluoride instead of water, this fluorolytic sol-gel route leads to the syntheses of nanoscopic metal fluorides. Metal fluoride derivatives with diverse properties can be prepared by varying parameters of this synthesis route. Especially, this work establishes the sol-gel synthesis route of novel nanoscopic FeF_3-based materials with bi-acidity, *i.e.* with both Lewis and Brønsted acid sites on the surface.

Fig. 8.1 describes the synthesis strategy of FeF_3-based materials. An essential step to achieve the bi-acidity is the dehydration treatment of iron(III) nitrate precursor before fluorination (pre-dehydration), which introduces hydroxyl groups as potential Brønsted acid sites into the precursor. These hydroxyl groups are preserved after fluorination. Thus the obtained FeF_3, which itself is a solid Lewis acid, is complemented with Brønsted acid sites. Subsequently, through a one-step fluorination, the partially hydroxylated FeF_3 is dispersed in a high-surface MF_2 matrix (M = Mg, Ca, Sr, or Zn); thus novel ternary FeF_3-MF_2 materials are obtained. They are marked by bi-acidic sites (Lewis and Brønsted) as well as prominently high surface area. This simple synthesis route creates opportunities to tune the properties of FeF_3-MF_2 materials by changing the M species or the M-to-Fe ratio, or both.

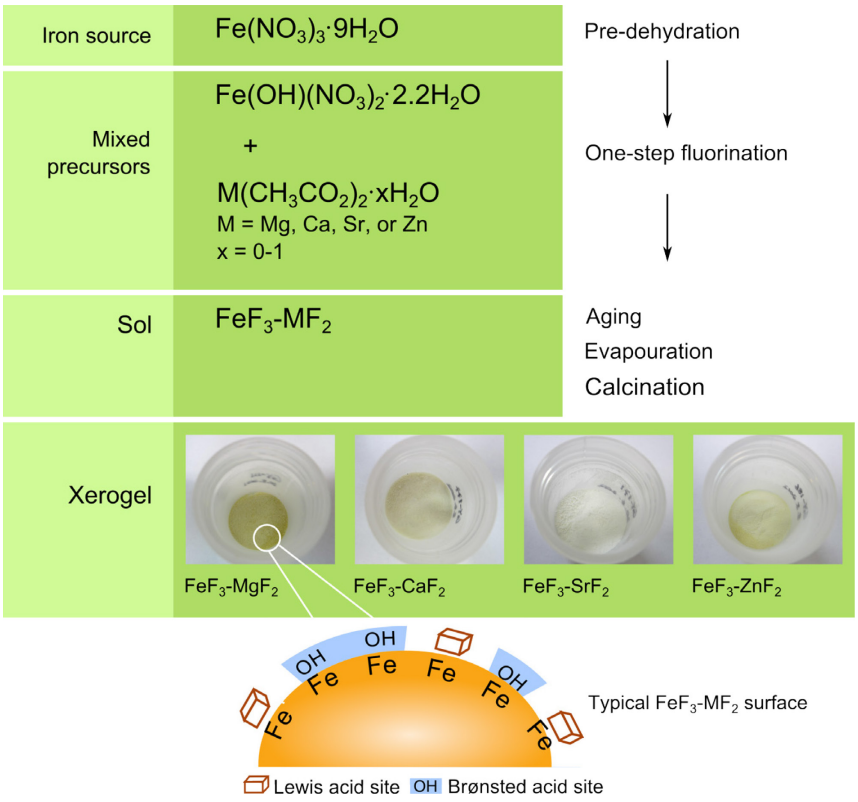

Fig. 8.1 Schematic illustration of the synthesis strategy of FeF_3-based materials with bi-acidity.

In this work, an extensive characterisation of the FeF_3-MF_2 materials was equally important as the efforts in developing the synthesis route. A series of analytical methods were employed in order to comprehensively study

the bulk properties of FeF_3-MF_2 materials: a combination of elemental and thermal analysis elucidated the chemical compositions; XRD patterns and TEM images confirmed the nanoscopic nature of these materials; STEM-EDX hypermaps suggested a homogeneous distribution of FeF_3 in the MF_2 matrix; and last but not least, Mössbauer spectra and XPS results revealed the atomic interactions between FeF_3 and the MF_2 matrix.

Moreover, the surface characteristics of FeF_3-MF_2 materials are of substantial interest since these materials are to be applied in heterogeneous catalysis, which is a surface phenomenon. They were investigated by N_2 adsorption-desorption measurements, NH_3-TPD, and chemisorption-IR with different probe molecules (NH_3, pyridine, and CD_3CN). Systematic changes in surface area, porosity, and surface acidity were revealed by varying the MF_2 species,. Using MF_2 as matrix generally increased the surface area of FeF_3-based materials and changed the porous structure: the FeF_3-MgF_2 and FeF_3-ZnF_2 mainly exhibited micropores (average pore diameter smaller than 3 nm), while the FeF_3-CaF_2 and FeF_3-SrF_2 samples exhibited mesopores (average pore diameter between 5 and 30 nm). Both Lewis and Brønsted acid sites were detected on the surface of FeF_3-MF_2 samples, confirming their bi-acidity. Notably, strong Lewis acid sites and medium strong Brønsted acid sites are predominant on the FeF_3-MgF_2 surface. All the FeF_3-MF_2 samples demonstrated activity in the model reaction of the isomerisation of citronellal to isopulegols, in which both Lewis and Brønsted acid sites are required. The catalytic results provided a final piece of evidence of the surface bi-acidity of these FeF_3-based materials.

The MF_2 matrices were proved to be inactive in the model reaction. Among all samples, FeF_3-MgF_2 showed the highest activity and selectivity towards isopulegols. The correlations of surface properties (*i.e.* surface area, porosity, and surface acidity) and the catalytic activity were discussed. Especially, microporosity and a combination of strong Lewis and medium strong Brønsted acidity were found favourable for high yield of isopulegols.

In brief, this study demonstrates the great potential of ternary FeF_3-MF_2 materials with tunable properties in heterogeneous catalysis. It opens new possibilities for targeted design and synthesis of nanoscopic fluoride materials with desirable surface properties.

Future work on FeF_3-based materials should address two important issues. On one hand, although this work identified FeF_3-MF_2 materials as highly active catalysts in a carbonyl-ene reaction, their potential in other types of reactions was not investigated. Further studies are therefore necessary to fully evaluate the values of FeF_3-MF_2. These materials can be tested in other acid-catalysed reactions like the Friedel-Craft reaction, the Diels-Alder reaction, and in organofluorine chemistry including dismutation of freons and dehalogenation of fluoroalkanes. On the other hand, synthesis routes of further FeF_3-based materials are worth investigating. Inspired by the ternary fluorides, other materials can be also used as matrix. For example, FeF_3 can be dispersed in iron oxides to prepare a magnetic catalyst, which can be separated easily after reaction. Other oxides like SiO_2, TiO_2, and Al_2O_3 can be also used to synthesise a variety of novel fluoride-oxide materials with different morphology and functions. Furthermore, carbon materials (carbon fibers, nanotubes, and graphene) and organic polymers can be added to the waiting list, too. These future FeF_3-based materials can bring new insights in developing the nanoscopic fluoride materials with high performance and low cost.

9 Experimental part

9.1 Source and purity of applied chemicals

9.1.1 Solid

Barium acetate	$Ba(CH_3COO)_2$	Sigma-Aldrich, 99%
Calcium acetate monohydrate	$Ca(CH_3COO)_2 \cdot H_2O$	Sigma-Aldrich, ≥ 99.0%
Iron acetylacetonate	$Fe(C_5H_7O_2)_3$	Aldrich, 97%
Iron chloride	$FeCl_3$	Riedel-deHaën, anhydrous, ≥ 98%
Iron fluoride	FeF_3	Merk, 98%
Iron nitrate nonahydrate	$Fe(NO_3)_3 \cdot 9H_2O$	Sigma-Aldrich, ≥ 98%
Iron oxide	Fe_2O_3	Riedel-deHaën, anhydrous, ≥ 97%
Magnesium acetate tetrahydrate	$Mg(CH_3COO)_2 \cdot 4H_2O$	Sigma-Aldrich, > 99%
Strontium acetate	$Sr(CH_3COO)_2 \cdot 0.5H_2O$	Sigma-Aldrich, ~ 97%
Zinc acetate	$Zn(CH_3COO)_2$	Sigma-Aldrich, 99.99%

9.1.2 Liquid

(±)-Citronellal	$C_{10}H_{18}O$	Acros, 93%, pract.
Deuterated acetonitrile	C_2D_3N	Sigma-Aldrich, 99.8 atom%
Ethanol	C_2H_6O	HU
Hydrogen fluoride solution	71% HF/H_2O	Sigma-Aldrich
	40% HF/H_2O	Fluka
Methanol	CH_4O	Sigma-Aldrich, 99.6%
Pyridine	C_5H_5N	Acros, anhydrous, 99.5%
Tetrahydrofuran (THF)	C_4H_8O	ABCR, 99%
Toluene	C_7H_8	Acros, for HPLC, 99.99%
Undecane	$C_{11}H_{24}$	Sigma-Aldrich, ≥ 99%

9.1.3 Gas

Ammonia	NH_3	Messer, anhydrous, 3.8
Argon	Ar	Air Liquide, 5.0
Hydrogen	H_2	Air Liquide, 5.0
Hydrogen fluoride	HF	Solvay Fluor
Nitrogen	N_2	Air Liquide, 5.0

9.2 Synthesis

9.2.1 Preparation of partially hydroxylated FeF_3

Pre-dehydration treatment of $Fe(NO_3)_3 \cdot 9H_2O$ (20 mmol, 8.08 g) was performed *in vacuo* at 65°C for 2 h. The obtained substance was dissolved in 100 mL methanol and fluorinated with stoichiometric amounts of HF (in methanolic solution). The obtained FeF_3 sol was aged for 14-16 h before dried *in vacuo*. The product xerogel was further calcined at 100°C for 2 h and hand-grinded to fine powders.

$Fe(NO_3)_3 \cdot 9H_2O$ was also used directly as precursor to prepare normal nanoscopic FeF_3 (without hydroxyls). This synthesis route followed the same procedure as described above.

9.2.2 Preparation of FeF_3-MgF_2

9.2.2.1 Sol-gel route

$Mg(CH_3COO)_2 \cdot 4H_2O$ was dehydrated at 210°C overnight in oven. It was then added to the pre-dehydrated iron nitrate precursor (see 9.2.1) at different molar Mg-to-Fe ratios. The mixed precursors were suspended in methanol and fluorinated in one-step with stoichiometric amounts of HF (in methanolic solution). The total metal concentration was 0.2 $mol \cdot L^{-1}$. The obtained FeF_3-MgF_2 sol was aged, dried and calcined under the same conditions as described in 9.2.1. The xerogel product was labeled as fm-*n*; f and m refer to FeF_3 and MgF_2 respectively, while *n* indicates the molar Mg-to-Fe ratio.

MgF_2 was also prepared as reference. The dehydrated $Mg(CH_3COO)_2$ (20 mmol, 2.85 g) was suspended in 100 mL methanol. Methanolic HF solution was added in stoichiometric amounts to the suspension. The drying procedure followed the same steps as in the synthesis of FeF_3 and FeF_3-MgF_2.

9.2.2.2 Mechano-milling

The mechano-milled sample was prepared with a planetary micro mill PULVERISETTE 7 *premium line* (Fritsch). The FeF_3 (2 mmol, 0.23 g) and MgF_2 (4 mmol, 0.25 g) xerogels were mixed and milled for 2×60 min at 600 rpm with 15 min break in between.

9.2.3 Preparation of FeF_3-MF_2 (M = Ca, Sr, or Zn)

In each synthesis, the metal acetate was used as received. It was added to the pre-dehydrated iron nitrate precursor (described in 9.2.1) at different M-to-Fe ratios. The mixed precursors were suspended in methanol (total concentration of metals: 0.2 $mol \cdot L^{-1}$) and fluorinated in one step with stoichiometric amounts of HF in methanolic solution. The obtained FeF_3-MF_2 sol was aged, dried and calcined following the same procedure as described in 9.2.1.

9.3 Analytical methods

9.3.1 Thermal analysis

Thermal analysis experiments were performed by using the hyphenation of Netzsch-STA-409C/CD and Balzers-QMG-422-Quadrupol-Mass spectrometry. Both TG curves and the *m*/*z* ratio of the fragments were recorded during measurements.

9.3.2 Elemental analysis (C, H, N, and F)

The C and H contents were determined with a Leco CHNS-932 analyser. The F contents were determined with a fluoride-sensitive electrode. Before the analysis, the samples were digested by fusion with soda-potash.

9.3.3 Dynamic light scattering

Dynamic light scattering (DLS) measurements were taken with a Malvern Zetasizer Nano ZS in NIBS mode at 173°. The methanolic fm-2 sol (concentration of metal = 0.2 $mol \cdot L^{-1}$) was filtered with a Nylon filter (ø = 450 nm).

9.3.4 Powder X-ray diffraction (XRD)

The XRD patterns were obtained from a XRD-7 Seifert-FPM diffractometer using Cu$K\alpha$ beam.

9.3.5 Mössbauer spectroscopy

The Mössbauer spectra of FeF_3, fm-2 and fm-9 at room temperature were taken with a standard transmission Mössbauer spectrometer (Halder) in the sinusoidal drive mode. The velocity scale was calibrated with an α-Fe absorber and the isomer shift (IS) is given relative to α-Fe.

9.3.6 Transmission electron microscopy (TEM)

The partially hydroxylated FeF_3 and three ternary FeF_3-MF_2 samples (fm-2, fc-4, and fs-7) were resuspended in methanol (2-3 mg/1 mL). A Lacey carbon film (Cu-networks, 300 mesh) was dipped in the sample suspension and dried in air. The TEM images were recorded with a Joel JEM-2200FS Transmission Electron Microscope, using a 200 kV field emission gun (FEG). A high angle annular dark field detector (HAADF) was applied to obtain STEM images.

9.3.7 X-ray photoelectron spectroscopy (XPS)

The XPS measurements were carried out with an ESCALab 200X photoelectron spectrometer (VG Scientific, U.K.) for all samples. XP survey spectra were recorded at an angle of emission of 0° using non-monochromatized Al Kα excitation with a constant retard ratio of 10. The samples were analysed under high-vacuum (< 10^{-8} mbar). Quantification was performed by using a routine implemented in the Advantage 4.43 software. The routine uses Scofield's photoionisation cross section data for determination of relative sensitivity factors. This quantification routine uses the model of homogeneous distribution of all constituents in the analyzed volume. The estimated IMFP was calculated with Gries (G-1) equation using the NIST Electron IMFP Database Version 1.2 (National Institute of Standards and Technology, Caithersburg, MD., U.S.A.).

9.3.8 N_2 adsorption-desorption

N_2 adsorption-desorption at 77 K was measured with a Micromeritics ASAP 2020 instrument. Samples were degassed at 80°C under high vacuum for 12 h. Specific surface area was calculated by using the B.E.T equation.

9.3.9 Temperature programmed desorption

The temperature programmed desorption of ammonia (NH_3-TPD) profiles were recorded with a Perkin Elmer FTIR-System 2000 at 930 cm^{-1}. The pre-heated (100°C) samples were loaded with NH_3 at 60°C. After purging with N_2, the temperature was raised by 10°C min^{-1} until reaching 450°C while the desorbed NH_3 was recorded.

9.3.10 Infrared spectroscopy (IR spectroscopy)

For the IR spectroscopy coupled with chemisorption of probe molecules (chemiorption-IR), about 25-30 mg sample was pressed at 1 ton into self-supporting disc (2 cm^2 area) for IR analysis. Fig. 9.1 gives an overview of the IR spectrometer equipped with chemisorption devices.

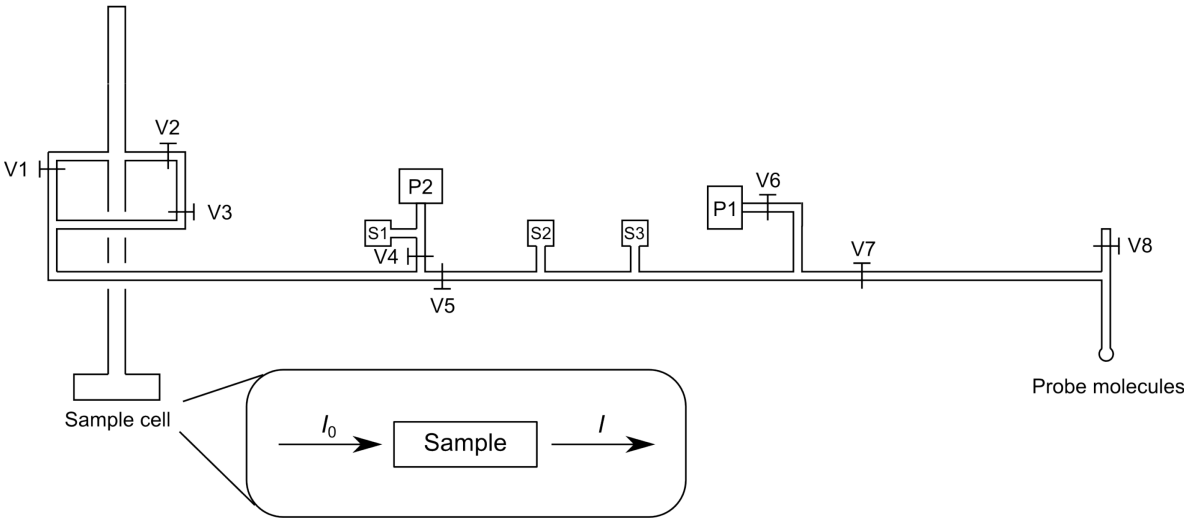

Fig. 9.1 Schematic illustration of IR spectrometer coupled with chemisorption devices. V1-V8: valves; P1: vacuum pump; P2: high-vacuum turbo pump; S1-S3: sensors.

The sample disc was placed in a quartz cell equipped with KBr windows. The cell was connected to a vacuum line and a glass injection loop. A movable quartz sample holder permits adjusting of the sample disc in the infrared beam for spectra acquisition, and to displace it into a furnace at the top of the cell for thermal activation of the samples. The cell was connected to a vacuum line and a glass injection loop. After we activated the sample at 80°C under vacuum, different probe molecules were added in small doses. The amount of injected probe molecules was regulated by the volume between V2 and V3. IR spectra were recorded on a Thermo Scientific Nicolet iS10 spectrometer. The IR spectrum of FeF_3 after degassing at 200°C under vacuum was taken with the same equipment without probe molecules.

9.4 Catalysis

Citronellal isomerisation reaction was performed in a Thermomixer comfort (Eppendorf) equipped with glass tubes. The samples were heated at 80°C *in vacuo* for 2 h before use to remove the surface impurities. Different amounts of fluoride samples were added to the reactants mixture (0.2 mL (*ca.* 1 mmol) citronellal, 0.1 mL undecane as internal standard for GC evaluation, and 2 mL toluene as solvent). The glass tubes were maintained at 80°C for 6 h. After the reaction, the catalysts were separated by filtration and the products were analysed by GC (Shimadzu GC-2010 with a HP-1 column of 100 m×0.25 mm×0.5 μm, temperature programming: starting temperature 120°C, hold time 50 min, rate 15°C·min^{-1}, end temperature 270°C, hold time 5 min).

Leaching test was executed by removing the catalyst from the reaction mixture after 3 h from the reaction beginning. The rest solution was kept under the reaction conditions for another 3 h. In the end, the reaction mixtures before and after the break were both analysed by GC.

Two recycling tests were taken under the same reaction conditions with the fm-2 catalyst. In the first test, the used catalyst was filtered out from a catalysis mixture and washed four times with acetone (10 min each), and then dried at 80°C under Ar flow (20 mL·min^{-1}). The first test included three recycling runs and each run lasted 3 h. In the second test, the catalyst was separated and washed with acetone for three times (5 min, 10 min and 12 h), and then dried at 80°C *in vacuo* for 6 h. One recycling run of 6 h reaction was performed in the second test.

References

[1] A. S. Hornby, *Oxford Advanced Learner's Dictionary of Current English*, 8th ed., Oxford University Press, Oxford, **2010**.

[2] G. Lövestam, H. Rauscher, G. Roebben, B. S. Klüttgen, N. Gibson, J.-P. Putaud, H. Stamm, *Considerations on a Definition of Nanomaterial for Regulatory purposes*, *Joint Research Centre (JRC) Reference Reports* **2010**, 80004-80001.

[3] J. Njuguna, K. Pielichowski, *Polymer Nanocomposites for Aerospace Applications: Properties*, *Advanced Engineering Materials* **2003**, *5*, 769-778.

[4] Y. Malam, M. Loizidou, A. M. Seifalian, *Liposomes and Nanoparticles: Nanosized Vehicles for Drug Delivery in Cancer*, *Trends in Pharmacological Sciences* **2009**, *30*, 592-599.

[5] G. Ertl, H. Knözinger, J. Weitkamp, *Handbook of Heterogeneous Catalysis, Vol. 1 and 2*, Wiley-VCH, Weinheim, **2008**.

[6] E. Kemnitz, U. Groß, S. Rüdiger, C. S. Shekar, *Amorphous Metal Fluorides with Extraordinary High Surface Areas*, *Angewandte Chemie International Edition* **2003**, *42*, 4251-4254.

[7] E. Kemnitz, S. Wuttke, S. M. Coman, *Tailor-Made MgF_2-Based Catalysts by Sol–Gel Synthesis*, *European Journal of Inorganic Chemistry* **2011**, 4773-4794.

[8] K. Teinz, S. Wuttke, F. Börno, J. Eicher, E. Kemnitz, *Highly Selective Metal Fluoride Catalysts for the Dehydrohalogenation of 3-Chloro-1,1,1,3-tetrafluorobutane*, *Journal of Catalysis* **2011**, *282*, 175-182.

[9] S. Wuttke, G. Scholz, S. Rüdiger, E. Kemnitz, *Variation of Sol-Gel Synthesis Parameters and Their Consequence for the Surface Area and Structure of Magnesium Fluoride*, *Journal of Materials Chemistry* **2007**, *17*, 4980-4988.

[10] S. Wuttke, S. M. Coman, J. Kröhnert, F. C. Jentoft, E. Kemnitz, *Sol-Gel Prepared Nanoscopic Metal Fluorides as a New Class of Tunable Acid-Base Catalysts*, *Catalysis Today* **2010**, *152*, 2-10.

[11] H. A. Prescott, Z.-J. Li, E. Kemnitz, J. Deutsch, H. Lieske, *New Magnesium Oxide Fluorides with Hydroxy Groups as Catalysts for Michael Additions*, *Journal of Materials Chemistry* **2005**, *15*, 4616-4628.

[12] S. M. Coman, S. Wuttke, A. Vimont, M. Daturi, E. Kemnitz, *Catalytic Performance of Nanoscopic, Aluminium Trifluoride-Based Catalysts in the Synthesis of (all-rac)-α-Tocopherol*, *Advanced Synthesis & Catalysis* **2008**, *350*, 2517-2524.

[13] K. Teinz, Dissertation thesis, Humboldt-Universität zu Berlin (Berlin), **2012**.

[14] A. Negoi, K. Teinz, E. Kemnitz, S. Wuttke, V. Parvulescu, S. Coman, *Bifunctional Nanoscopic Catalysts for the One-Pot Synthesis of (+/-)-Menthol from Citral*, *Topics in Catalysis* **2012**, *55*, 680-687.

[15] N. Candu, S. Wuttke, E. Kemnitz, S. M. Coman, V. I. Parvulescu, *Friedel-Crafts Alkylations on Nanoscopic Inorganic Fluorides*, *Applied Catalysis A: General* **2011**, *391*, 169-174.

[16] S. M. Coman, P. Patil, S. Wuttke, E. Kemnitz, *Cyclisation of Citronellal over Heterogeneous Inorganic Fluorides--Highly Chemo- and Diastereoselective Catalysts for (+/-)-Isopulegol*, *Chemical Communications* **2009**, 460-462.

[17] A. Negoi, S. Wuttke, E. Kemnitz, D. Macovei, V. I. Parvulescu, C. M. Teodorescu, S. M. Coman, *One-Pot Synthesis of Menthol Catalyzed by a Highly Diastereoselective Au/MgF_2 Catalyst*, *Angewandte Chemie International Edition* **2010**, *49*, 8134-8138.

[18] S. Wuttke, A. Negoi, N. Gheorghe, V. Kuncser, E. Kemnitz, V. Parvulescu, S. M. Coman, *Sn-Doped Hydroxylated MgF_2 Catalysts for the Fast and Selective Saccharification of Cellulose to Glucose*, *ChemSusChem* **2012**, *5*, 1708-1711.

[19] Holleman, Wiberg, *Lehrbuch der Anorganischen Chemie*, Walter de Gruyter, Berlin, New York, **2007**.

[20] G. Brauer, *Handbuch der Präparativen Anorganischen Chemie, Vol. 1*, Ferdinand Enke Verlag, Stuttgart, **1960**.

[21] P. Laszlo, *Catalysis of Organic Reactions by Inorganic Solids*, *Accounts of Chemical Research* **1986**, *19*, 121-127.

[22] B. P. Bandgar, V. T. Kamble, *Organic Reactions in Aqueous Medium: FeF_3 Catalyzed Chemoselective Addition of Cyanotrimethylsilane to Aldehydes*, *Green Chemistry* **2001**, *3*, 265-266.

[23] T. Hatakeyama, M. Nakamura, *Iron-Catalyzed Selective Biaryl Coupling: Remarkable Suppression of Homocoupling by the Fluoride Anion*, *Journal of the American Chemical Society* **2007**, *129*, 9844-9845.

[24] J. Krishna Murthy, U. Gross, S. Rüdiger, E. Kemnitz, *FeF_3/MgF_2: Novel Lewis Acidic Catalyst Systems*, *Applied Catalysis A: General* **2004**, *278*, 133-138.

[25] I. K. Murwani, K. Scheurell, E. Kemnitz, *Liquid Phase Oxidation of Ethylbenzene on Pure and Metal Doped HS-AlF_3*, *Catalysis Communications* **2008**, *10*, 227-231.

[26] J. C. Leffingwell, R. E. Shackelford, *Laevo-Menthol, Syntheses and Organoleptic Properties*, *Cosmetics and Perfumery* **1974**, *89*, 69-89.

[27] Y. Nakatani, K. Kawashima, *A Highly Stereoselective Preparation of l-Isopulegol*, *Synthesis* **1978**, *1978*, 147-148.

[28] G. K. Chuah, S. H. Liu, S. Jaenicke, L. J. Harrison, *Cyclisation of Citronellal to Isopulegol Catalysed by Hydrous Zirconia and Other Solid Acids*, *Journal of Catalysis* **2001**, *200*, 352-359.

[29] C. J. Brinker, G. W. Scherer, *Sol-Gel Science: The Physics and Chemistry of Sol-Gel Processing*, Academic Press, San Diego, **1990**.

[30] J. Alemán, A. V. Chadwick, J. He, M. Hess, K. Horie, R. G. Jones, P. Kratochvíl, I. Meisel, I. Mita, G. Moad, S. Penczek, R. F. T. Stepto, *Definitions of Terms Relating to the Structure and Processing of Sols, Gels, Networks, and Inorganic-Organic Hybrid Materials*, *Pure and Applied Chemistry* **2007**, *79*, 1801-1829.

[31] J. Livage, M. Henry, C. Sanchez, *Sol-Gel Chemistry of Transition Metal Oxides*, *Progress in Solid State Chemistry* **1988**, *18*, 259-341.

[32] J. Livage, C. Sanchez, M. Henry, S. Doeuff, *The Chemistry of the Sol-Gel Process*, *Solid State Ionics* **1989**, *32-33, Part 2*, 633-638.

[33] K. Nakamoto, *Infrared Spectra of Inorganic and Coordination Compounds*, John Wiley & Sons Inc, **1970**.

[34] H. Hertz, *Über einen Einfluss des ultravioletten Lichtes auf die electrische Entladung*, *Annalen der Physik* **1887**, *267*, 983-1000.

[35] A. Einstein, *Über einen die Erzeugung und Verwandlung des Lichtes betreffenden heuristischen Gesichtspunkt*, *Annalen der Physik* **1905**, *322*, 132-148.

[36] K. Siegbahn, K. Edvarson, *Beta-Ray Spectroscopy in the Precision Range of 1 : 105*, *Nuclear Physics* **1956**, *1*, 137-159.

[37] P. Gütlich, *Fifty Years of Mössbauer Spectroscopy in Solid State Research – Remarkable Achievements, Future Perspectives*, *Zeitschrift für anorganische und allgemeine Chemie* **2012**, *638*, 15-43.

[38] J. M. Thomas, R. M. Lambert, *Characterisation of catalysts, Chapter II: the Use of Physisorption for the Determination of Surface Area and Pore Size Distribution*, John Wiley, Chichester, **1980**.

[39] G. Leofanti, M. Padovan, G. Tozzola, B. Venturelli, *Surface Area and Pore Texture of Catalysts*, *Catalysis Today* **1998**, *41*, 207-219.

[40] S. G. Bratsch, *A Group Electronegativity Method with Pauling Units*, *Journal of Chemical Education* **1985**, *62*, 101.

[41] K. Wieczorek-Ciurowa, A. J. Kozak, *The Thermal Decomposition of $Fe(NO_3)_3 \cdot 9H_2O$*, *Journal of Thermal Analysis and Calorimetry* **1999**, *58*, 647-651.

[42] Y. Guo, S. Wuttke, A. Vimont, M. Daturi, J.-C. Lavalley, K. Teinz, E. Kemnitz, *Novel Sol-Gel Prepared Zinc Fluoride: Synthesis, Characterisation and Acid-Base Sites Analysis*, *Journal of Materials Chemistry* **2012**, *22*, 14587-14593.

[43] D. B. Williams, C. B. Carter, *Transmission Electron Microscopy: A Textbook for Materials Science*, Springer, **2009**.

[44] A. A. Tsyganenko, D. V. Pozdnyakov, V. N. Filimonov, *Infrared Study of Surface Species Arising from Ammonia Adsorption on Oxide Surfaces*, *Journal of Molecular Structure* **1975**, *29*, 299-318.

[45] K. Góra-Marek , M. Derewiński, P. Sarv, J. Datka, *IR and NMR Studies of Mesoporous Alumina and Related Aluminosilicates*, *Catalysis Today* **2005**, *101*, 131-138.

[46] A. G. Pelmenschikov, R. A. van Santen, J. Janchen, E. Meijer, *Acetonitrile-d3 as A Probe of Lewis and Broensted Acidity of Zeolites*, *The Journal of Physical Chemistry* **1993**, *97*, 11071-11074.

[47] D. R. Lide, *Handbook of Chemistry and Physics*, 84 ed., CRC Press, **2003-2004**.

[48] X. Liu, Y. Guo, Y. Wang, J. Ren, Y. Wang, Y. Guo, Y. Guo, G. Lu, Y. Wang, Z. Zhang, *Direct Synthesis of Mesoporous Fe_3O_4 through Citric Acid-Assisted Solid Thermal Decomposition*, *Journal of Materials Science* **2010**, *45*, 906-910.

[49] G. K. Wertheim, H. J. Guggenheim, D. N. E. Buchanan, *Sublattice Magnetization in FeF_3 near the Critical Point*, *Physical Review* **1968**, *169*, 465-470.

[50] J. M. Grenèche, *Magnetic Frustration in Ferric Fluorides Investigated by Mössbauer Spectrometry*, *Hyperfine Interactions* **1999**, *122*, 9-19; M. Eibschütz, M. E. Lines, L. G. Van Ultert, H. J. Guggenheim, G. J. Zydzik, *Mössbauer Study of Amorphous FeF_3*, *Physical Review B* **1984**, *29*, 3843-3851; M. Eibschütz, M. E. Lines, L. G. Van Uitert, H. J. Guggenheim, G. J. Zydzik, *Study of Local Environment in a Series of Amorphous Ferric Fluorides*, *Physical Review B* **1981**, *24*, 2343-2348; G. Ferey, F. Varret, J. M. D. Coey, *Amorphous FeF_3 : A Non-Crystalline Magnet with Antiferromagnetic Interactions*, *Journal of Physics C: Solid State Physics* **1979**, *12*, L531.

[51] S. Wuttke, S. M. Coman, G. Scholz, H. Kirmse, A. Vimont, M. Daturi, S. L. M. Schroeder, E. Kemnitz, *Novel Sol–Gel Synthesis of Acidic $MgF_{2-x}(OH)_x$ Materials*, *Chemistry – A European Journal* **2008**, *14*, 11488-11499.

[52] F. Menil, *Systematic Trends of the ^{57}Fe Mössbauer Isomer Shifts in (FeO_n) and (FeF_n) Polyhedra. Evidence of A New Correlation between the Isomer Shift and the Inductive Effect of the Competing Bond T-X (→Fe) (Where X is O or F and T Any Element with a Formal Positive Charge)*, *Journal of Physics and Chemistry of Solids* **1985**, *46*, 763-789.

[53] C. J. Powell, A. Jablonski, *NIST Electron Inelastic-Mean-Free-Path Database*, Version 1.2, SRD71, National Institute of Standards and Technology, Caithersburg, MD, **2010**.

[54] R. Paul, R. Narula, S. Vasisht, *Iron(III) Acetates*, *Transition Metal Chemistry* **1978**, *3*, 35-38.

[55] E. H. Teunissen, R. A. Van Santen, A. P. J. Jansen, F. B. Van Duijneveldt, *Ammonium in Zeolites: Coordination and Solvation Effects*, *The Journal of Physical Chemistry* **1993**, *97*, 203-210.

[56] A. Auroux, *Acidity and Basicity*, Springer-Verlag Heidelberg **2008**.

[57] D. Cook, *Vibrational Spectra of Pyridinium Salts*, *Canadian Journal of Chemistry* **1961**, *39*, 2009-2024.

[58] K. Bauer, D. Garbe, H. Surburg, *Ullmann's Encyclopedia of Industrial Chemistry, Vol. A11*, Wiley-VCH Weinheim, **1988**.

[59] D. H. Pybus, C. S. Sell, *The Chemistry of Fragrances*, RSC Paperbacks, Cambridge **1999**.

[60] B. B. Snider, M. Karras, R. T. Price, D. J. Rodini, *Alkylaluminum Halide Induced Cyclization of Unsaturated Carbonyl Compounds*, *The Journal of Organic Chemistry* **1982**, *47*, 4538-4545; H. M. R. Hoffmann, *The Ene Reaction*, *Angewandte Chemie International Edition in English* **1969**, *8*, 556-577.

[61] W. Oppolzer, V. Snieckus, *Intramolecular Ene Reactions in Organic Synthesis*, *Angewandte Chemie International Edition in English* **1978**, *17*, 476-486.

[62] B. B. Snider, *Lewis-Acid Catalyzed Ene Reactions*, *Accounts of Chemical Research* **1980**, *13*, 426-432.

[63] S. Akutagawa, *Enantioselective Isomerization of Allylamine to Enamine: Practical Asymmetric Synthesis of (-)-Menthol by Rh-BINAP Catalysts*, *Topics in Catalysis* **1997**, *4*, 271-274.

[64] P. Kočovský, G. Ahmed, J. Šrogl, A. V. Malkov, J. Steele, *New Lewis-Acidic Molybdenum(II) and Tungsten(II) Catalysts for Intramolecular Carbonyl Ene and Prins Reactions. Reversal of the Stereoselectivity of Cyclization of Citronellal*, *The Journal of Organic Chemistry* **1999**, *64*, 2765-2775.

[65] V. K. Aggarwal, G. P. Vennall, P. N. Davey, C. Newman, *Scandium Trifluoromethaneslfonate, An Efficient Catalyst for the Intermolecular Carbonyl-Ene Reaction and the Intramolecular Cyclisation of Citronellal*, *Tetrahedron Letters* **1998**, *39*, 1997-2000.

[66] P. Mäki-Arvela, N. Kumar, V. Nieminen, R. Sjöholm, T. Salmi, D. Y. Murzin, *Cyclization of Citronellal Over Zeolites and Mesoporous Materials for Production of Isopulegol*, *Journal of Catalysis* **2004**, *225*, 155-169; A. Corma, M. Renz, *Sn-Beta Zeolite as Diastereoselective Water-Resistant Heterogeneous Lewis-Acid Catalyst for Carbon-Carbon Bond Formation in the Intramolecular Carbonyl-Ene Reaction*, *Chemical Communications* **2004**, *0*, 550-551.

[67] Z. Yongzhong, N. Yuntong, S. Jaenicke, G.-K. Chuah, *Cyclisation of Citronellal Over Zirconium Zeolite Beta—a Highly Diastereoselective Catalyst to (+/-)-Isopulegol*, *Journal of Catalysis* **2005**, *229*, 404-413.

[68] N. Ravasio, M. Antenori, F. Babudri, M. Gargano, in *Studies in Surface Science and Catalysis, Vol. 108*, Elsevier, **1997**, pp. 625-632.

[69] K. A. da Silva, P. A. Robles-Dutenhefner, E. M. B. Sousa, E. F. Kozhevnikova, I. V. Kozhevnikov, E. V. Gusevskaya, *Cyclization of (+)-Citronellal to (-)-Isopulegol Catalyzed by $H_3PW_{12}O_{40}/SiO_2$*, *Catalysis Communications* **2004**, *5*, 425-429.

[70] K. A. da Silva Rocha, P. A. Robles-Dutenhefner, E. M. B. Sousa, E. F. Kozhevnikova, I. V. Kozhevnikov, E. V. Gusevskaya, *Pd-Heteropoly Acid as a Bifunctional Heterogeneous Catalyst for One-Pot Conversion of Citronellal to Menthol*, *Applied Catalysis A: General* **2007**, *317*, 171-174.

Acknowledgements

In the end, it is the author's privilege to express thanks to those who have contributed to this work. First of all, I would like to thank my supervisor, Prof. Erhard Kemnitz, whose rich scientific experiences and kind attendance perfectly explained the German word "Doktorvater". I would also like to thank Prof. Zhu Yuexiang, my supervisor in my Bachelor time. Without her recommendation and encouragement, I might not have chosen to come to Germany and study here. It is my great luck to meet the two excellent supervisors in my twenties; what I have learned from them will have a life-long effect.

Many have supported this work in practical ways. For help in reviewing the manuscript I am grateful to Katharina Teinz, Kaichin Chang, Matthias Karg, Thoralf Krahl, Larisa Schmidt (who also helped with DLS measurement), and Felix Hemmann. For help in material characterisation I am grateful for the assistance provided by Sigrid Bäßler (who performed fluorine analysis and TPD), Michael Feist (who offered help in thermal analysis and discussion of the results), Gudrun Scholz (who helped organising the collaboration in Mössbauer spectroscopy), Holm Kirmse (who took the TEM images), Andreas Lippitz (who helped with the XPS measurement), and Piotr Gaczyński and Klaus-Dieter Becker (who performed the Mössbauer measurement). Maik Dreger helped synthesising the mechano-milled sample, and Paul Saftien helped preparing the samples in 5.2.2.2 which was part of his internship under my supervision. I acknowledge their vital assistance greatly. A scholarship from the Chinese Scholarship Council allowed me to work as a doctoral student in the Kemnitz group. I express my thanks to them sincerely.

Special thanks to the girls from the Kemnitz group: Kathi, Kaichin, Larisa, and Aga, who are the air of the working place and have offered wonderful tea breaks, which I enjoyed and appreciated heartily.

Finally I owe a special debt to Jitao David Zhang, for all his support and care in our domestic life and for the efforts he made over a long period to help me concentrate on writing, and to my mother and father, who always encouraged me to work in this demanding career. It is to them, my family, that this work is dedicated.

Selbstständigkeitserklärung

Hiermit erkläre ich die vorliegende Dissertation am Institut für Chemie der Humboldt-Universität zu Berlin unter der Betreuung von Prof. Dr. Erhard Kemnitz selbstständig und nur unter Verwendung zulässiger und angegebener Hilfsmittel angefertigt zu haben.

Berlin, den

Die Arbeit ist für den Leihverkehr freigegeben.

Berlin, den

Scientific CV

Education

10/2009-06/2013

Doctoral student, supervised by Prof. Erhard Kemnitz, Institut für Chemie, Humboldt-Universität zu Berlin, Berlin, Germany.

Topic: Novel nanoscopic FeF_3–based materials: synthesis, characterisation, and catalytic applications

09/2005-07/2009

B. Sc. in chemistry, supervised by Prof. Yuexiang Zhu, College of Chemistry and Molecular Engineering, Peking University, Beijing, China. Grade: 3.25 out of 4.

Topic: Effect of carbon on the structure and photo-catalytic activity of TiO_2

Scientific experience

05/2013-

Research project in pigment chemistry, internship at BASF Schweiz AG, Basel, Switzerland.

10/2009-08/2010

Research project, in the group of Prof. Erhard Kemnitz, Institut für Chemie, Humboldt-Universität zu Berlin, Berlin, Germany.

Topic: Sol-gel synthesis and characterisation of nanoscopic ZnF_2 and NiF_2

04/2007-10/2008

Research project, in the group of Prof. Yuexiang Zhu, College of Chemistry and Molecular Engineering, Peking University, Beijing, China.

Topic: Phosphorus-doped TiO_2 and its photo-catalytic activity

Awards and scholarships

04/2013

EFCATS PhD student awards, for the XIth European Congress on Catalysis, Lyon, France.

09/2009-06/2013

Scholarship by Chinese Scholarship Council, for the doctoral study, Beijing, China.

04/2007-10/2008

Mini-grant from the National Fund for Foresting Talents of Basic Science (JO630421), for the undergraduate student research project, Beijing, China.

Publication list

Publications

2013

Sol-gel synthesis and surface characterisation of novel ternary FeF_3-MF_2 catalysts (M = Mg, Ca, Sr, or Zn), **Y. Guo**, A. Lippitz, P. Saftien, W. Unger and E. Kemnitz, *in preparation*.

Dehydration of xylose and glucose to furan derivatives using innovative bifunctional partially hydroxylated MgF_2 catalysts, *Green Chemistry*, I. Agirrezabal-Telleria, **Y. Guo**, C. Jäger, M.B. Güemez, P.L. Arias and E. Kemnitz, *in revision*.

Sol-gel synthesis and characterisation of nanoscopic FeF_3-MgF_2 heterogeneous catalysts with bi-acidic properties, *ChemCatChem*, **Y. Guo**, P. Gaczyński, K.-D. Becker and E. Kemnitz, *in print*, DOI: 10.1002/cctc.201300115.

2012

Novel sol-gel prepared zinc fluoride: synthesis, characterisation and acid-base sites analysis, *Journal of Materials Chemistry*, 22, 14587-14593, **Y. Guo**, S. Wuttke, A. Vimont, M. Daturi, J.C. Lavalley, K. Teinz and E. Kemnitz.

2010

Influence of carbon on phase transformation of oxides in carbon/oxide composites, *Acta Physico-Chimica Sinica*, 26, 1887-1892, **Y. Guo**, P. Wang, Y. Wang, Y.X. Zhu and Y.C. Xie.

Novel thermally stable phosphorus-doped TiO_2 photocatalyst synthesized by hydrolysis of $TiCl_4$, *Journal of Molecular Catalysis A: Chemistry*, 319, 46-51, R.Y. Zheng, **Y. Guo**, C. Jin, J.L. Xie, Y.X. Zhu and Y.C. Xie.

2009

Hydrothermal synthesis and characterization of phosphorous-doped TiO_2 with high photocatalytic activity for methylene blue degradation, *Journal of Molecular Catalysis A: Chemistry*, 313, 44-48, C. Jin, R.Y. Zheng, **Y. Guo**, J.L. Xie, Y.X. Zhu and Y.C. Xie.

Presentations

2013

Sol-gel synthesis and surface characterisation of novel ternary FeF_3-MF_2 catalysts (M = Mg, Ca, or Sr), ***poster and oral presentation*** at *the symposium "The importance of nanostructuring in catalyst design and preparation" at the XIth European Congress on Catalysis*, Lyon, France, **Y. Guo** and E. Kemnitz.

2012

Sol-gel synthesis of novel high-surface FeF_3-MgF_2 catalysts, ***oral presentation*** at *the 15. Deutscher Fluortag*, Schmitten, Germany, **Y. Guo** and E. Kemnitz.

2011

Sol-gel synthesis and characterization of nanoscopic transition fluorides, ***oral presentation*** at *the Xth European Congress on Catalysis*, Glasgow, Scotland, **Y. Guo** and E. Kemnitz.